Open and Hidden Charm Mesons at Finite Temperature from Anisotropic Lattice QCD

Aoife Kelly
B.Sc.

Thesis presented for the degree of

Doctor of Philosophy

to the

National University of Ireland Maynooth
Department of Mathematical Physics

February 2017

Department Head

Dr. Jon-Ivar Skullerud

Research advisor

Dr. Jon-Ivar Skullerud

Contents

Abstract

The quark-gluon plasma (QGP) is conjectured to have existed in the early stages of the Big Bang and it has been discovered in heavy ion collisions. The internal properties of the medium are not well understood. Due to its large mass and long thermalisation time, the charm quark is an excellent tool with which to probe the plasma. In this thesis I study the dissociation of open and hidden charm mesons.

Lattice QCD provides a non-perturbative means of studying the spectral quantities of charmed mesons. The suppression of J/ψ in medium is widely considered to be a signal for deconfinement. I will use J/ψ to study the heavy quark diffusion through the QGP. Jet-quenching observed in heavy ion collision experiments may be studied through the D mesons, increasing experimental interest in open charm. I will present the first study of the spectral functions of these mesons.

The finite resolution in the time direction is one of the main limiting factors in obtaining reliable spectral functions from lattice QCD. In order to reduce the ensuing uncertainties we are currently producing a set of highly anisotropic lattices which will greatly improve the accuracy of our results. I will outline the method employed in the generation of these ensembles and present preliminary results.

Acknowledgements

I first wish to extend my thanks and appreciation to my supervisor, Dr. Jon-Ivar Skullerud without whom I could not have reached this point. Your guidance and support have been immense and you always had time for my questions.

For the lunch and office banter, I'd like to particulary thank Úna, John, Darragh, Aonghus, Mikael, Rob, Sepanda and Glen. Over the last few years you guys have never failed to put a smile on my face — even while beating me at Mario Kart! To every other member of the Maths Physics department, thanks for making it such an enjoyable place to come and work. To the members of the Maths Support Centre, it's been a privilege getting to teach alongside you all. A special thanks goes to Dr. Ciarán Mac an Bhaird for his support, advice and kindness.

Tuesdays in Trinity were always something to look forward to, and for that I thank Graham, Pol, Tim and Darran. To my collaborators near and far, it's been a geniune pleasure working with everyone, in particular Chris, Gert and Alex.

To the friends I've had since primary school and the friends I've gained since, thank you all for your support and motivation. It's been a tough road but I always knew I could count on you, particularly Ally, Ramsey, Megan, and all the old fencing crowd — there are too many to name. Needless to say Maynooth has not been the same since we left 37 and 55 behind.

To the Leinster rugby team, for providing much-needed excitement and distraction. It's always a thrill going to the RDS for a game, and having that to look forward to has kept my spirits up.

Lastly, I'd like thank my parents James and Gráinne, and my sisters Cassandra and Jenny. You guys have been a rock I could lean on and your unwavering love and support have seen me through some impossible days. I could never express how truly grateful I am.

I also acknowledge the finanicial support of the Irish Research Council, and the Student Assistance Fund in NUIM.

Chapter 1

Introduction

1.1 Motivation

1.1.1 The Big Bang

The leading theory on the formation of the universe is that it began approximately 13.8 billion years ago as a singularity in space filled with a medium with a very high energy density and enormous temperatures. A phase transition kick-started cosmic inflation and the universe began to rapidly expand and cool. At 10^{-11} s and at a temperature $T \sim 10^{15}$ K (~ 100 GeV) the electroweak phase transition occured and gave the fundamental particles their mass through the Higgs mechanism [1, 2]. What remained after the inflation period (at $\sim 10^{-6}$s) was a jumble of hot, dense matter known as the quark gluon plasma (QGP), and other elementary particles known as leptons. At these temperatures the particles were incredibly energetic and were thus continuously colliding causing the creation and annihilation of particle-antiparticle pairs. Baryogenesis resulted in an excess of quarks and leptons over antiquarks and antileptons. Little is yet understood about this reaction. It is conjectured to be the main reason for the predominance of matter over antimatter in the universe.

At 10^{-5} s and at $T \sim 10^{12}$ K (~ 200 MeV), the strong phase transition took place and combined the free quarks into hadrons [3]. At these temperatures, fewer collisions occured which could result in the creation of new particle pairs and so pair annihilation vastly reduced the number of antiparticles. This all occured within the first few minutes, after which the temperature and density were low enough to allow for nucleosynthesis — the formation of nuclei (mostly hydrogen and helium). These atoms further combined into molecules and eventually formed the stars, planets and every other tangible component of this universe. Modern particle physics experiments can reproduce the temperatures at which this nucleosynthesis occurs and so from this point the theories surrounding expansion of the universe and subsequent particle

formation are robust.

Only in the last few decades have the collider experiments managed to obtain the temperatures at which a quark-gluon plasma may be formed. As such its internal properties are yet uncertain. As it is thought to be the earliest stage of matter to exist in the universe, it has been a hot topic for research for many decades.

1.1.2 Phase Diagram of Quantum Chromodynamics

Quantum Chromodynamics (QCD) is the study of the strong nuclear force. It assigns a colour charge (of red, green or blue) to quarks and gluons. When combining to form a hadron, only quarks and gluons of the correct colour combination may be united. In nature, quarks are bound in colour-neutral hadronic states and are never found alone. However, if enough energy is applied to a hadron, the binding force becomes weaker and they can break apart into a QGP state. This phenomenon is known as deconfinement and it occurs at a temperature of $T_c \sim 155\text{MeV}$ [4].

Quarks carry an inherently quantum mechanical property known as chirality in which a quark may be considered to be right-handed or left-handed. When rotating a right- or left-handed fermion, chirality imposes a particular way in which the quantum wavefunction is shifted. For massless particles, rotating the right- and left-handed components independently has no overall effect on the theory. This is known as chiral symmetry. In the chiral limit of massless quarks ($m_q \to 0$), the QCD Lagrangian is chirally symmetric. However, at low temperatures the massless quarks obtain an effective mass by dressing with gluons. Thus in the hadronic phase this symmetry is spontaneously broken. The quarks ψ and antiquarks $\bar{\psi}$ combine to form chiral condensates $\langle\bar{\psi}\psi\rangle$ in the QCD vacuum. The presence of these condensates spontaneously breaks chiral symmetry and they act as the order parameter for the transition. The left and right $SU(2)$ rotations are locked into an isospin symmetry and this results in the creation of three Goldstone bosons — the pions.

It is the spontaneous breaking of chiral symmetry that accounts for the majority of the mass of bound hadronic states. At high temperatures thermal motion removes the quark dressing and chiral symmetry is restored. For massless quarks there is a first order chiral phase transition between the plasma of free quarks and gluons and the tightly bound hadronic phase. However, in nature it is simply a crossover and is parallelled by a deconfinement crossover. [5, 6]. A sketch of the QCD phase diagram is presented in Figure 1.1. The quark condensates do not survive in the QGP and chiral symmetry is restored. The temperature at which chiral symmetry restoration occurs happens to coincide with the deconfinement crossover. Therefore, chiral symmetry restoration is

also a signal for deconfinement.

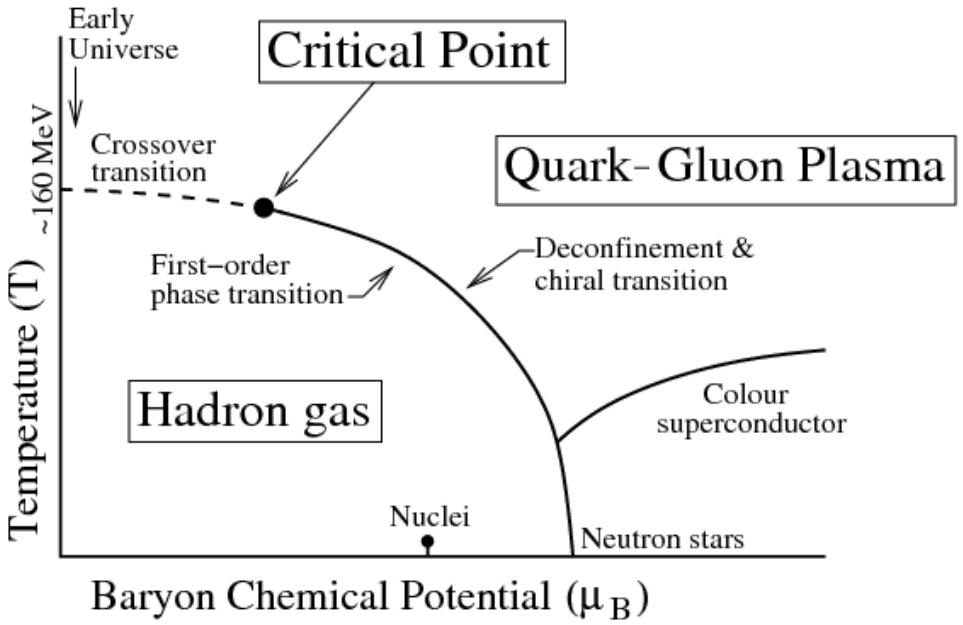

Figure 1.1: QCD phase diagram as a function of temperature T and baryon chemical potential μ. Taken from [arXiv:nucl-th/1404.3294]

1.1.3 Probing the Quark Gluon Plasma

The high energy heavy ion collision experiments undertaken at the Large Hadron Collider (LHC) in the European Organisation for Nuclear Research (CERN) and at the Relativistic Heavy Ion Collider (RHIC) in Brookhaven National Laboratory (BNL) have achieved a QGP state. In these experiments the nuclei of heavy atoms (e.g. lead and gold) are accelerated to speeds close to the speed of light and made to collide with one another. The nuclei are blasted apart into partons. A significant amount of the kinetic energy of the incoming nuclei collects in the central region, culminating in a high energy-density fireball. The partons in this fireball subsequently collide with one another and lead to a thermalised state, the QGP. The plasma then cools and expands, leading to hadronisation. Eventually, the hadrons stop colliding and travel towards the detector. Measurements of the final particles in the detector are taken and in this way one may establish whether the QGP phase was achieved. Ultra relativistic heavy ion collision (URHIC) experiments can give great insight into phases of matter, particle decays and even the discovery of new particles.

The STAR collaboration at RHIC has defined the QGP as a (locally) thermally equilibrated state of matter in which quarks and gluons are deconfined from hadrons so that the colour degrees of freedom become manifest over nuclear, rather than merely nucleonic, volumes [7]. Very little is yet known about its internal structure. Experimental results so far characterise the QGP as a strongly coupled, colour-opaque liquid with temperatures far exceeding the

critical temperature for deconfinement. As the QGP cools it experiences a collective expansion known as flow. Flow is an experimental observable which can provide information on the equation of state and transport properties of the medium [8, 9]. In heavy ion collisions the azimuthal anisotropy in particle production is the clearest indicator of the flow. Non-central collisions cause asymmetries in the geometry of the system characterised by the anisotropic flow. At high energies the longitudinal and transverse components of the flow can be treated independently and as such the plane transverse to the beam can be used to study the flow pattern. The distribution of the final state particles is generally written as a Fourier expansion as follows

$$E\frac{\mathrm{d}^3N}{\mathrm{d}^3p} = \frac{1}{2\pi}\frac{\mathrm{d}^2N}{p_T\mathrm{d}p_T\mathrm{d}y}\left[1+\sum_{n=1}^{\infty}2v_n\cos(n(\phi-\Phi_R))\right], \tag{1.1}$$

where E is the energy of the particle, p_T is the transverse momentum, y is the rapidity, ϕ is the azimuthal angle of the outgoing particle's momentum, and Φ_R is the angle of the reaction plane. The leading term is the radial transverse flow and the second term represents the anisotropic transverse flow. The anisotropic flow corresponding to the first two coefficients v_1, v_2 plays an important role in collision experiments. v_1 is known as the directed flow, which provides information about the direction of the flow itself, and v_2 is the elliptic flow. Elliptic flow is named from the fact that when two particles collide indirectly the cross-sectional area is shaped like an ellipse. The coefficients are computed as follows

$$v_n = \langle\cos(n(\phi-\Phi_R))\rangle. \tag{1.2}$$

Since Φ_R is not directly observable, the elliptic flow cannot be measured in experiment. It is estimated using azimuthal correlations between the particles. Elliptic flow has been studied extensively at RHIC [10, 7, 11] and the LHC [12, 13]. The QGP was found to display properties similar to ideal hydrodynamic predictions and this led to the idea that it is an almost ideal liquid. Its ratio of shear viscosity to entropy density is very close to the conjectured lower bound on any quantum mechanical system $\eta/s \geq 1/4\pi$ [14] and its observed elliptic flow is almost as large as that of an ideal fluid [15].

Collision experiments at RHIC and the LHC can directly measure thermodynamic and transport properties of the QGP by comparing results from heavy ion collisions which include the QCD medium to those of proton-proton collisions which represent the QCD vacuum. The first major discovery at RHIC was that energetic hadrons are strongly suppressed in central Au + Au collisions [16, 17]. They discovered that energetic partons could influence production of new particles in hot nuclear matter [18, 19]. Partons with a high transverse momentum p_T can radiate gluons and split into quark-antiquark

pairs. After this parton branching, the resulting particles fragment into the final state hadrons. The directed spray of hadrons from one of these parton fragmentations is known as a jet. Alongside elliptic flow, jet quenching is one of the most important observables in URHICs.

There is a measurable energy loss in partons scattering in a QGP state due to jet quenching [20]. In order to conserve momentum, jets should be observed travelling in opposite directions. However, only one spray of hadrons from a highly energetic parton is detected [21, 22, 23, 24]. The energy loss is composed of collisional and radiative terms. Loss of collisional energy occurs through elastic scatterings and dominates when the particles have a low momentum. At high momentum, the energy losses are radiative and derive from inelastic scatterings. Radiative energy losses can be determined by the photon or gluon Bremsstrahlung spectra. However, jet quenching is not sufficient to explain the large suppression of non-photonic electrons which was also observed at RHIC. These electrons are predominately produced in the semi-leptonic decays of D and B mesons, which are usually considered to be formed from heavy quark fragmentation outside the medium. It is possible that these mesons may be produced and subsequently dissociate in the QGP [25]. The existence of the heavy D and B mesons above the deconfinement temperature may explain the energy loss and flow of heavy quarks observed in heavy ion collisions [26]. It is therefore essential to have a theoretical understanding of the dissolution of the heavy mesons in medium.

1.1.4 Heavy Quarks in the Quark Gluon Plasma

The heavy quarks, charm (c) and bottom (b), make excellent probes into the QGP. Their masses (1.3GeV and 4.5GeV respectively) are significantly larger than the temperatures reached in the collider experiments. This indicates that they are produced only in the primordial nucleon-nucleon collisions [27] as the production threshold is much higher than the temperature of the medium. Their thermal relaxation times are comparable to the the lifetime of the QGP phase in URHICs [28], although charm quarks may thermalise more quickly. As such, heavy quarks are not expected to reach thermal equilibrium in the QGP and their in-medium interactions will have a noticeable effect on the momentum spectrum. An analysis of heavy quark spectra can therefore produce a timeline of the evolution of the QGP and it can be probed over the full range of its transverse momentum, leading to a complete picture of the medium at all scales [29]. Heavy quarks are used as a standard hard probe of the QGP at high transverse momentum and their interactions with the medium at low transverse momentum are approximated by Brownian motion. Heavy quarks are arguably the most direct probes of the entire QCD medium.

In a vacuum, the free energy of a heavy quark-antiquark pair $Q\bar{Q}$ is assumed to have the string form [30], given in the usual units ($\hbar = c = 1$) as

$$F(r) \sim \sigma r, \tag{1.3}$$

where $\sigma \simeq 0.16$ GeV^2 is the string tension and r is the separation between the constituent quarks. The free energy increases as the quarks are pulled away from one another. When it reaches the value of a pair of dressed light quarks, a $q\bar{q}$ pair is produced from the vacuum, the string breaks and two new hadrons $Q\bar{q}, q\bar{Q}$ are formed.

At finite temperature, where $T < T_c$, chiral symmetry is broken and there are dynamical light quarks in the medium. An effective screening of the colour force occurs. The light hadrons can interact with the $Q\bar{Q}$ pair and recouple their contituents at a lower energy value [31]. Beyond the deconfinement threshold, chiral symmetry is restored and there is a significant increase in the density of constituents. Light quarks and gluons become deconfined resulting in a genuine colour screening. The screening radius r_D is inversely proportional to the density of colour charges. It follows that as the temperature is increased, the screening radius decreases and counteracts the binding force in hadrons causing them to dissociate.

Colour screening induces the suppression of heavy quarkonia in nucleus-nucleus collisions in comparison with proton-proton yields and this suppression is predicted to be a signal for deconfinement [32]. A sequential pattern is anticipated, with the excited states dissociating before the more tightly-bound ground states. The strongly bound J/ψ meson is the ideal candidate for studying this prediction. Identifying a suppression pattern in collider experiments is not an easy task. The overall charmonium yield also contains J/ψ mesons appearing as decay products of higher mass resonances and b-hadrons.

Experimentally, J/ψ production has been studied at the Super Proton Synchrotron (SPS), RHIC and the LHC at a large range of energies. The J/ψ yield was found to be suppressed in nucleus-nucleus collisions with respect to proton-proton collisons. Cold nuclear matter (CNM) effects such as shadowing and nuclear absorption can cause J/ψ to dissociate. However the overall suppression far exceeded that expected from CNMs at both SPS [33, 34] and RHIC [35]. SPS ran at a lower centre of mass energy per nucleon pair $\sqrt{s_{NN}} = 158$ GeV. They observed that that J/ψ suppression was consistent with the melting of excited states. RHIC employed a higher energy $\sqrt{s_{NN}} = 200$ GeV and concluded there is an element of suppression for the direct J/ψ [36, 37]. In recent years the LHC has reached energies of $\sqrt{s_{NN}} = 2.76$ TeV and the CMS experiment has also observed a sequential suppression pattern for $\Upsilon = b\bar{b}$ [38].

At this high energy, the ALICE experiment measured a greater J/ψ yield than the $\sqrt{s_{NN}} = 200$ GeV experiment at RHIC [39]. This large centre of mass energy allows for a much higher charm quark density in the QGP [40]. Charm and anticharm pairs can coalesce, leading to the regeneration of J/ψ mesons in the medium [41, 42]. If J/ψ can survive in the medium, production due to the recombination of $c\bar{c}$ pairs may occur during the lifespan of the QGP [43, 44]. However, if they are fully suppressed, recombination will occur at the phase boundary [45, 46]. Charm quarks are mostly produced at low momentum, so the regeneration of J/ψ at low transverse momentum is anticipated, and has been confirmed experimentally [47]. J/ψ suppression, on the other hand, is a high-p_T process. It is therefore essential that the transverse momentum and rapidity behaviour of J/ψ is understood to establish the balance between suppression and recombination.

The in-medium modification of heavy quarkonium production in nucleus-nucleus collisions is quantified by the nuclear modification factor

$$R_{AA} = \frac{N_{AA}^{Q\bar{Q}}}{\langle T_{AA} \rangle \times \sigma_{pp}^{Q\bar{Q}}}, \tag{1.4}$$

where $N_{AA}^{Q\bar{Q}}$ is the quarkonium yield in nucleus-nucleus collisions, $\sigma_{pp}^{Q\bar{Q}}$ is the cross section in proton-proton collisions and the ratio is scaled by the average nuclear overlap $\langle T_{AA} \rangle$. A non-unity value for R_{AA} implies that $Q\bar{Q}$ production in heavy ion collisions is modified with respect to a binary nucleon-nucleon scaling. Further insight into the medium effects on the $Q\bar{Q}$ yield is gained by studying the transverse momentum and rapidity dependence of R_{AA}. At forward-rapidity, the J/ψ R_{AA} shows a clear suppression of the J/ψ yield at an energy $\sqrt{s_{NN}} = 2.76$ TeV and it was found to have a strong dependence on its transverse momentum [48, 49]. The results differ radically from the RHIC results at $\sqrt{s_{NN}} = 200$ GeV, suggesting that a portion of the yield is due to charmonium recombination in medium. At $\sqrt{s_{NN}} = 5.02$ TeV, the ALICE experiment also measured J/ψ suppression at high p_T and considerable regeneration at low p_T [50]. The overall yield was much larger than observed at $\sqrt{s_{NN}} = 2.76$ TeV suggesting a far greater recombination in the hotter medium.

Theoretically, the suppression of the J/ψ particle can be studied at finite temperature by considering the spectral functions of the vector meson current. A description of spectral functions can be found in Section (2.2). A mass peak is evident in the spectrum if the particle survives the medium. Spectral functions can be calculated at a number of temperatures and a qualitative estimate for the temperature at which the meson melts can be evaluated. The low frequency region of these spectra is related to the quantitative properties of the QGP, for example the heavy quark diffusion and electrical conductivity.

1.2 The Path Integral Formulation of QCD

The fundamental equation governing the mechanics of the strong nuclear force is the QCD Lagrangian. Quarks interact through the exchange of gluons, the gauge bosons for the theory. Due to the non-abelian nature of QCD the gluons are also subject to self-interactions. The Lagrangian describes these interactions and is given by

$$\mathcal{L} = \bar{\psi}\left(i\gamma^{\mu}D_{\mu} - m\right)\psi - \frac{1}{4}G^{a}_{\mu\nu}G^{\mu\nu}_{a}, \tag{1.5}$$

where ψ is the quark field, D_{μ} is the covariant derivative

$$D_{\mu} = \partial_{\mu} + igA^{a}_{\mu}(x), \tag{1.6}$$

and $G^{a}_{\mu\nu}$ is the gauge invariant gluon field strength tensor with colour index a given by

$$G^{a}_{\mu\nu} = \partial_{\mu}A^{a}_{\nu} - \partial_{\nu}A^{a}_{\mu} + gf_{abc}A^{b}_{\mu}A^{c}_{\nu}. \tag{1.7}$$

Here, A^{a}_{μ} is the gluon field, g is the strong running coupling and f_{abc} is the structure constant. In practice, one calculates the action which is related to the Lagrangian via

$$\mathcal{S} = \int_{C} \mathcal{L}\, \mathrm{d}^{4}x. \tag{1.8}$$

For quantum physical systems, the action may have an infinite number of configurations over which to integrate. The behaviour of the system is dependent on all possible trajectories and their relative probability amplitudes. In order to calculate this, Feynman introduced the path integral formalism, which is closely linked with statistical field theory. The basic tool required to quantise quark and gluon fields is the partition function

$$Z = \int \mathcal{D}[\Phi]\, \mathrm{e}^{i\mathcal{S}[\Phi]}. \tag{1.9}$$

Here, $\mathcal{S}[\Phi]$ is the action which is dependent on the fields $\Phi = \psi, \bar{\psi}, A_{\mu}$ and we neglect a possible chemical potential dependence. In order to solve this integral for our system, we employ the use of the Wick rotation $t \to -it \equiv \tau$ and work in imaginary time. This yields a Euclidean action $\mathcal{S}_{E} = i\mathcal{S}$ and allows us to work in Euclidean spacetime. Our partition function then becomes

$$Z_{E} = \int \mathcal{D}[\Phi]\, \mathrm{e}^{-\mathcal{S}_{E}[\Phi]}. \tag{1.10}$$

The expectation value of an operator $\mathcal{O}$ in the Euclidean representation is

$$\langle\mathcal{O}\rangle = \frac{1}{Z_{E}}\int \mathcal{D}[\Phi]\, \mathcal{O}[\Phi]\, \mathrm{e}^{-\mathcal{S}_{E}[\Phi]}. \tag{1.11}$$

Finite temperature field theory is formulated using the Matsubara formalism for statistical systems. At zero baryon chemical potential, the quantum mechanical partition function is given by

$$Z(T) = \mathrm{tr}\left[\mathrm{e}^{-\hat{H}/(k_B T)}\right], \tag{1.12}$$

where $\hat{H}$ is the Hamiltonian operator and k_B is the Boltzmann constant. The path integral formulation of this partition function gives the temperature as the reciprocal of the imaginary time period, yielding the action

$$\mathcal{S}(\phi, \psi) = \int_0^\beta \mathrm{d}\tau \int \mathrm{d}^3x \; \mathcal{L}(\phi, \psi), \tag{1.13}$$

where ϕ is a boson field with periodic boundary conditions, ψ is a fermion field with antiperiodic boundary conditions and $\beta = 1/k_B T$ is the inverse temperature. As is usual, we set $k_B = 1$ so $\beta = 1/T$ and the temperature is given in units of energy.

1.3 QCD on the Lattice

1.3.1 Discretising Spacetime

The path integral formalism which is described in equation (1.10) is not well-defined. A regularisation scheme must be implemented to solve it. In order to regularise the theory non-perturbatively, we introduce a four dimensional hypercubic lattice of finite size $N_s^3 \times N_\tau$ with a finite lattice spacing a and periodic boundary conditions. The continuum may be recovered by taking $a \to 0$ while keeping the volume constant.

The fermion fields are found on the lattice sites and the gluons on the links connecting them. Infinite integrals may now be calculated as finite sums and continuous derivatives are replaced by their discrete counterparts. In order to ensure the action remains invariant under a local rotation of the colour indices of the quark fields, a link variable $U_\mu \in SU(3)$ in the direction $\hat{\mu}$ is introduced, where

$$U_\mu(x) = \exp\left[ig \int_x^{x+\hat{\mu}a} \mathrm{d}y^\mu A_\mu(y)\right] \tag{1.14}$$

connects the neighbouring lattice sites x and $x + \hat{\mu}$. Thus we can define

$$\psi'(x) = \Omega(x)\psi(x); \tag{1.15}$$

$$U'_\mu(x) = \Omega(x) U_\mu(x) \Omega^\dagger(x + \hat{\mu}). \tag{1.16}$$

such that

$$\bar{\psi}(x)U_\mu(x)\psi(x+\hat{\mu}) \to \bar{\psi}'(x)U'_\mu(x)\psi'(x+\hat{\mu})$$

is a gauge transformation where $\Omega(x)$ is an element of $SU(3)$ at each lattice site x. The link variables are oriented and thus we can define a link variable connecting the site x to $x-\hat{\mu}$ as

$$U_{-\mu}(x) \equiv U^\dagger_\mu(x-\hat{\mu}) \tag{1.17}$$

As the gluons live on the links between the fermion sites, these link variables represent the gluon fields in QCD. In the absence of quark fields, the link variables must form closed loops in order to retain their gauge invariance. They are known as Wilson loops. The simplest of these is a plaquette $U_{\mu\nu}$, which is a square comprised of four link variables as follows.

$$U_{\mu\nu}(x) = U_\mu(x)U_\nu(x+\hat{\mu})U^\dagger_\mu(x+\hat{\nu})U^\dagger_\nu(x). \tag{1.18}$$

1.3.2 Lattice Actions

In the continuum, the Yang-Mills action represents the gluons and the Dirac action represents the fermions. On the lattice, discretised versions of these actions must be implemented. The plaquette is the simplest object on the lattice. The gluon action can be built as a sum over all plaquettes. This is the Wilson gauge action, as formulated in [51]

$$\mathcal{S}_G[U] = \frac{2}{g^2}\sum_{x\in\Lambda}\sum_{\mu<\nu}\text{Re tr}[\mathbb{1} - U_{\mu\nu}(x)], \tag{1.19}$$

where g is the strong coupling. In the limit $a \to 0$ the Yang-Mills action should be reproduced. However, the lattice only reproduces the continuum action correct to $\mathcal{O}(a^2)$. Symanzik proposed a solution to these large discretisation errors by introducing improved lattice actions. To implement Symanzik Improvement, one adds terms with the appropriate symmetries to the action. Their coefficients may then be tuned to become functions of the bare couplings. The simplest example of Symanzik Improvement is the action containing the plaquette $U_{\mu\nu}$ and the rectangular 1×2 Wilson loop $R_{\mu\nu}$ as follows

$$\mathcal{S}^I_G[U] = \frac{2}{g^2}\sum_{x\in\Lambda}\sum_{\mu<\nu}\left\{\frac{5}{3}\text{Re tr}\left[\mathbb{1} - U_{\mu\nu}(x)\right] - \frac{1}{6}\text{Re tr}\left[\mathbb{1} - \frac{1}{2}R_{\mu\nu}(x)\right]\right\}. \tag{1.20}$$

Naïvely, one expects to discretise the Dirac action in order to obtain a

lattice action for fermions as follows

$$\mathcal{S}_F^N[\psi,\bar{\psi},U] = \sum_{f=1}^{N_f} a^4 \sum_{x,y\in\Lambda} \bar{\psi}^{(f)}(x) M^{(f)}(x|y)\psi^{(f)}(y), \tag{1.21}$$

where a is the lattice spacing and M is the fermion matrix given by

$$M^{(f)}(x|y)_{\alpha\beta,ab} = m^{(f)} a\delta_{\alpha\beta}\delta_{ab}\delta_{x,y} - \frac{1}{2}\sum_{\mu=\pm1}^{\pm4} (\gamma_\mu)_{\alpha\beta} U_\mu(x)_{ab}\delta_{x+\hat{\mu},y}. \tag{1.22}$$

However, this introduces a complication. This naïve discretisation of the fermion action leads to 2^d flavours for each fermion field in the continuum limit. This doubling problem is easily demonstrated by considering the free quark propagator in momentum space. The Fourier transform of the action (with $U_\mu = 1$) is

$$\mathcal{S}_F^{-1}(p) = m + \frac{i}{a}\sum_\mu \gamma_\mu \sin(p_\mu a), \tag{1.23}$$

leading to a free quark propagator

$$\langle\bar{\psi}(p)\psi(q)\rangle = \left(m + \frac{i}{a}\sum_\mu \gamma_\mu \sin(p_\mu a)\right)^{-1} \delta(p-q). \tag{1.24}$$

In the continuum limit $a \to 0$ this propagator has poles not only at zero but at the corners of the first Brillouin zone, usually defined to be at $[-\pi/a, \pi/a]$. If any component of the momentum is equal to $\pm\pi/a$, then the same continuum is formed. In four dimensions this yields an additional 15 unwanted fermions. Nielsen and Ninomiya proved in their No-Go Theorem that these doublers cannot be removed if the theory is to be kept chirally symmetric, local and hermitian [52].

A number of options have been formulated for the fermion action which break one of these conditions. However, it is essential that they are restored in the continuum limit. The most commonly used methods by lattice theorists are the staggered fermion approach pioneered by Kogut and Susskind [53] which violates locality, the Wilson fermion formulation [54] which breaks chiral symmetry, and the Ginsparg-Wilson approach [55] in which chiral symmetry survives if the Dirac operator obeys the equation $M\gamma_5 + \gamma_5 M = aM\gamma_5 M$, where a is the lattice spacing. We will focus on Wilson's approach. Wilson proposed that a second derivative term (now known as the Wilson term) may be added to the action in order to cancel out the fermion doublers. The Wilson fermion

action is then

$$\mathcal{S}_F^W[\psi,\bar{\psi},U] = \sum_{f=1}^{N_f} a^4 \sum_{x,y\in\Lambda} \bar{\psi}^{(f)}(x)\Big[\left(m^{(f)}+\frac{4}{a}\right)\delta_{\alpha\beta}\delta_{ab}\delta_{x,y} - \frac{1}{2a}\sum_{\mu=\pm1}^{\pm4}(\mathbb{1}-\gamma_\mu)_{\alpha\beta}U_\mu(x)_{ab}\delta_{x+\hat{\mu},y}\Big]\psi^{(f)}(y). \tag{1.25}$$

The addition of the Wilson term in the action introduces $\mathcal{O}(a)$ errors. Further terms may be added in order to cancel these $\mathcal{O}(a)$ errors. The simplest improved fermion action is the Sheikholeslami-Wohlert action [56] which is an $\mathcal{O}(a^2)$ improvement of the Wilson action.

1.3.3 Anisotropic Lattices

In utilising discrete lattices to calculate continuum results there will always be some errors involved. There are many methods in use which balance computational cost with reducing these errors. One such method removes any dynamical quark flavours from the system. This is known as the quenched approximation of QCD. From equation (1.11) we can compute the quark propagator

$$\begin{aligned}\langle\bar{\psi}(x)\psi(y)\rangle &= \frac{1}{Z}\int \mathcal{D}A_\mu\mathcal{D}\bar{\psi}\mathcal{D}\psi\ \bar{\psi}(x)\psi(y)\ \mathrm{e}^{-(\mathcal{S}_F+\mathcal{S}_G)}\\ &= \frac{1}{Z}\int \mathcal{D}A_\mu\ \mathrm{Tr}\left(M^{-1}(x,y)\right)\ \det M\ \mathrm{e}^{-\mathcal{S}_G}.\end{aligned} \tag{1.26}$$

The effects of the sea quarks are contained in the determinant of the fermion matrix. In the quenched approximation this is set to $\det M = 1$. This yields a medium which is made purely from gluons. The assumption that there are no dynamical quarks in the QGP allows for a larger temporal extent on the lattice, and as such more viable data points.

However, the inclusion of dynamical sea quarks is desirable. With each flavour of quark, there is a new mass to take into account and the level of computational difficulty rises as each new flavour is introduced. The masses of the up and down quarks are usually taken to be degenerate. Our results have been calculated on two sets of ensembles – one with 2 flavours of dynamical sea quarks (up, down) and one with $2+1$ flavours (up, down, and strange) corresponding to the FASTSUM Collaboration's first and second generations.

We will use anisotropic lattices with a spatial lattice spacing a_s different than the temporal lattice spacing a_τ. The anisotropy is given by $\xi = a_s/a_\tau$. There are many benefits to using anisotropic lattices. They make it possible to do relativistic simulations with heavy quarks [57] which would otherwise have been too computationally expensive. Employing a smaller temporal lattice

spacing ensures there are more timeslices in the Monte Carlo data with an accurate signal. This is because the signal-to-noise ratio of the correlators decays exponentially with time. Thus, P-wave states [58] and glueballs [59] have become accessible despite their bad signal-to-noise ratio. Another big advantage is that thermodynamic quantities become much easier to calculate. It is a much simpler task to take derivatives with respect to volume and temperature if a_s and a_τ can be varied independently.

There are, however, added complications in the use of anisotropic lattices which are not present in the quenched or isotropic cases. Two new parameters appear in the anisotropic actions — the bare gauge and bare fermion anisotropies, γ_g and γ_f respectively. These parameters must be tuned so that the physical anisotropies of the quarks and gluons are the same.

A two-plaquette anisotropic Symanzik-Improved gauge action was developed for the the study of the glueball spectrum [60]. It includes a term composed of two parallel plaquettes on adjacent timeslices and was found to have reduced the finite cut-off effects in glueball studies. This gauge action was employed in the first generation. It is given by

$$\mathcal{S}'_G[U] = \frac{\beta}{\gamma_g}\left[\frac{20}{3u_s^4}\mathcal{P}_{ss} - \frac{15}{3u_s^8}\mathcal{P}'_{ss} - \frac{1}{12u_s^6}\mathcal{R}_{ss}\right] + \beta\gamma_g\left[\frac{4}{3u_s^2u_t^2}\mathcal{P}_{st} - \frac{1}{12u_s^4u_t^2}\mathcal{R}_{st}\right], \tag{1.27}$$

where $\mathcal{P}$ and $\mathcal{R}$ are the usual 1×1 plaquette and 2×1 rectangular Wilson loops, $\mathcal{P}'_{ss}$ is constructed from two spatial plaquettes separated by a temporal link, u_s and u_t are the spatial and temporal tadpole factors of the bare links, γ_g is the bare gauge anisotropy, $\beta = 2N_c/g^2$ is the lattice coupling and $N_c = 3$ is the number of colours.

The fermion action for this generation is a fine-Wilson, coarse Hamber-Wu action [61] with stout-link smearing [62]. The temporal component is a fine-Wilson action given by

$$\begin{aligned}\mathcal{S}_F^W[\psi,\bar\psi,U] = a^4\sum_{x,y\in\Lambda}\bar\psi(x)\Big[&\left(m+\frac{4}{a}\right)\delta_{\alpha\beta}\delta_{ab}\delta_{x,y}\\ &-\frac{1}{2a}(\mathbb{1}-\gamma_4)_{\alpha\beta}U_{\pm4}(x)_{ab}\delta_{x+\hat\mu,y}\Big]\psi(y).\end{aligned} \tag{1.28}$$

The spatial component uses the coarse Hamber-Wu action given by

$$\begin{aligned}\mathcal{S}_F^{HW}[U,\bar{\psi},\psi] = \frac{1}{a_s}\Bigg\{ &\sum_x \bar{\psi}(x)\psi(x) \\ &- \frac{4\kappa}{3}\sum_{x,i}\Big[\bar{\psi}(x)(r-\gamma_i)U_i(x)\psi(x+\hat{\imath}) \\ &\qquad - \bar{\psi}(x)(r+\gamma_i)U_i^\dagger(x-\hat{\imath})\psi(x-\hat{\imath})\Big] \\ &+ \frac{\kappa}{6u_s}\sum_{x,i}\Big[\bar{\psi}(x)(2r-\gamma_i)U_i(x)U_i(x+\hat{\imath})\psi(x+2\hat{\imath}) \\ &\qquad - \bar{\psi}(x)(2r+\gamma_i)U_i^\dagger(x-\hat{\imath})U_i^\dagger(x-2\hat{\imath})\psi(x-2\hat{\imath})\Big]\Bigg\},\end{aligned} \tag{1.29}$$

where u_s is the mean spatial link, r is the Wilson parameter, and κ is the hopping parameter. Putting these two components together yields the complete fermion action

$$\mathcal{S}_F = \mathcal{S}_F^{HW} + \mathcal{S}_F^{W} \tag{1.30}$$

Our second generation of lattices utilised an anisotropic Symanzik-Improved gauge action with tree-level tadpole coefficients as follows

$$\mathcal{S}_G[U] = \frac{\beta}{\gamma_g}\left\{\sum_{x,s>s'}\left[\frac{5}{3u_s^4}\mathcal{P}_{ss'} - \frac{1}{12u_s^6}\mathcal{R}_{ss'}\right] + \sum_{x,s}\left[\frac{4}{3u_s^2u_t^2}\mathcal{P}_{st} - \frac{1}{12u_s^4u_t^2}\mathcal{R}_{st}\right]\right\}, \tag{1.31}$$

where all parameters are the same as in the two-plaquette case in equation (1.27).

The fermion action for the second generation is an anisotropic clover action with tree-level tadpole coefficients and stout-link smearing [63], using the same parameters as the Hadron Spectrum Collaboration [64].

$$\begin{aligned}\mathcal{S}_F^{C}[U,\bar{\psi},\psi] = \sum_x \bar{\psi}(x)\frac{1}{\tilde{u}_t}\Bigg\{ &\tilde{u}_t\hat{m}_0 + \hat{W}_t + \frac{1}{\gamma_f}\sum_s \hat{W}_s \\ &- \frac{1}{2}\left[\frac{c_s}{\gamma_g}\sum_{s<s'}\sigma_{ss'}\hat{F_{ss'}} + c_t\sum_s \sigma_{ts}\hat{F}_{ts}\right]\Bigg\}\psi(x),\end{aligned} \tag{1.32}$$

where γ_f is the bare fermion anisotropy, $\hat{F}_{\mu\nu} = a_\mu a_\nu F_{\mu\nu}$ and $\hat{m}_0 = a_t m_0$ are dimensionless and $\hat{W}_\mu = a_\mu^2\nabla_\mu - \frac{1}{2}\gamma_\mu a_\mu \Delta_\mu$ is the dimensionless Wilson operator. To distinguish the tadpole factors associated with the smeared gauge fields, we denote them by $\tilde{u}_s$ and $\tilde{u}_t$. The parameters c_s and c_t are known as the clover coefficients.

The physical extent of the lattice in the temporal direction given by

$$\beta \equiv a_\tau N_\tau = \frac{1}{T}. \tag{1.33}$$

Here we must be careful not to confuse the inverse temperature with the lattice coupling β. We can clearly see that since the temporal extent is inversely proportional to the temperature, if we wish to use a high temperature lattice, the extent in the time direction must be small (and thus have a small number of data points). A lattice representing zero temperature has a large temporal extent in comparison to the length of the lattice in each spatial direction. This large number of data points allows for much more reliable results as $T \to 0$.

1.3.4 Scale Setting

There is only one dimensionful parameter in QCD. It is a mass scale Λ_{QCD} which satisfies the equation

$$g^2 \frac{b_0}{8\pi^2} \ln\left(\frac{M}{\Lambda_{QCD}}\right) = 1 \tag{1.34}$$

to leading order, where g is the strong coupling constant, M is the renormalisation scale, and $b_0 = 11 - (2/3)N_f$ for N_f quark flavours. The scale is dependent on the renormalisation scheme, and the $\overline{MS}$ scheme measures it to be $\Lambda_{QCD} \sim 200$MeV. The strong interactions become strong for distances larger than $\sim 1/\Lambda$. This is approximately the size of a light hadron.

Calculating meaningful values for physical quantities on the lattice is only possible if the scale Λ_{QCD} is correctly set. To set the scale, the distance between two adjacent lattice sites, the lattice spacing a, must be fixed. All observables in the action are dimensionless. After a simulation is completed, a physical quantity may be compared to experimental results and the lattice spacing is then fixed.

The choice of observable is important as different physical quantities probe different energy scales. There are many options available to set the scale. It is required that the observable is computable to a reasonable precision, that it is not heavily dependent on the quark mass and that it is experimentally verifiable. The string tension is one choice whose benefit is that it is computable in pure gauge theory, although it can be noisy. The Sommer scale r_0 is a popular choice, though not directly observable in experiments (but it can be related to the Υ spectrum and the heavy quark potential).

Hadron masses are also used to set the scale. The pion is usually used to set the quark mass and is therefore a poor choice to set the scale. The ρ mass depends too heavily on the quark mass. The $\Omega^- = sss$ baryon makes an

excellent choice. While it does depend on the strange quark mass, this can be tuned to a physical value and it has only a weak dependence on the up and down quark masses. Decay constants such as f_π and f_K may also be used, but they require renormalisation. The splittings $1S - 1P$ for charmonium and $2S - 1S$ for bottomonium are also valid choices. The heavy quarks are not dynamical in the simulations and the splittings do not depend strongly on the light and strange quark masses.

Two different generations of lattices are used in this work. To set the scale, the first generation of ensembles used the $1S - 1P$ fine splitting in charmonium. The static quark potential was first used, but after calculations with heavy quarkonia the scale setting was redone. The second generation of ensembles was created by the Hadron Spectrum Collaboration whose work involved calculating the mass of the Ω^- baryon. It was a logical choice for setting the scale.

1.4 Thesis Outline

The aim of this work is to explore the properties of the quark gluon plasma using the charm quark to probe its internal structure. We compute the correlation functions for charmonium and D mesons on a range of finite temperature lattices. The dynamical coefficients of the QGP are encoded in the spectral functions. They are a crucial factor in studying the medium modification of hadrons. Calculating the spectrum is an ill-posed problem and requires the use of the Maximum Entropy Method [65]. Details of the methods used are given in Chapter 2.

Chapter 3 presents the spectral functions for the J/ψ meson obtained on anisotropic lattices with an anisotropy of $\xi = 6.0$ and two dynamical fermion flavours. I analyse the spectral functions of the conserved vector current at finite temperature and non-zero momentum. The vector meson correlator is decomposed into its transverse and longitudinal polarisations. The low frequency range of the spectral functions of the conserved vector current is considered. This provides a limit for the diffusion coefficient of the QGP.

The second generation of lattices has an anisotropy of $\xi = 3.5$ and $2 + 1$ flavours of dynamical quarks. On this set of ensembles I calculate the spectral functions for the S-waves and P-waves for charmonium and the S-waves of the D and D_s mesons at finite temperature. I present the results in Chapter 4. I also present the reconstructed correlators and effective masses for these particles. A comparison to the original correlators shows that there are in-medium thermal modifications. A mass shift is noticable in the spectral functions of both the pseudoscalars and the vectors at temperatures below the deconfinement temperature T_c.

The first results for charmonium have been calculated on a set of anisotropic lattices with an anisotropy of $\xi = 6$ and two dynamical flavours of light quarks with degenerate masses. The next generation then introduced the strange quark at a different mass. In addition to charmonium this allowed me to calculate the spectral functions for the D mesons, which could not have been accurately produced on the first generation. The anisotropy was lowered to $\xi = 3.5$, increasing the temporal lattice spacing a_τ from 0.0268 fm to 0.03506 fm. We aim to create a new generation with $2 + 1$ flavours of dynamical quarks with $\xi = 7$. With each new generation of lattices we are a step closer to more accurately approximating the real world. The results obtained from this new generation of lattices will have smaller discretisation errors and it may be possible to obtain some new results which until now could not be accurately calculated, e.g. the first excited states of charmed mesons. Increasing ξ involves tuning a number of parameters in order to get the lattices we desire. This method is outlined in Chapter 5. This is an ongoing project and when the production of this new generation is complete there will be an opportunity to unveil some new results which were previously unattainable.

Chapter 2

Methodology

2.1 Correlation Functions

The fundamental object describing the properties of a particle is the correlation function (or correlator). For a meson it is defined as the vacuum expectation value of the time ordered product of two meson operators $\mathcal{M}$

$$G(x) = \langle 0|\mathcal{M}(x)\ \mathcal{M}(0)|0\rangle, \tag{2.1}$$

$$\mathcal{M} = \bar{\psi}_i(x)\Gamma_{ij}\psi_j(x), \tag{2.2}$$

where $\psi(x)$ is the fermion field and Γ_{ij} determines the particle channel as per Table 2.1. The meson correlator is composed of the quark propagator and the antiquark propagator connecting the same two points. It is thus known as the point-to-point correlator.

Correlation functions are particularly important in finite temperature studies. Our interest is in the deconfinement crossover and hadron melting. The degrees of freedom and properties of a hadron are expected to change drastically as the system crosses the transition line. Since correlators are temperature independent, they are the ideal candidate to provide information about the melting of mesons. The energy spectrum of a hadron can be extracted from

Particle	Γ	J^P
Pseudoscalar	γ_5	0^-
Scalar	$\mathbb{1}$	0^+
Vector	γ_μ	1^-
Axial Vector	$\gamma_5\gamma_\mu$	1^+

Table 2.1: The different channels for each particle and their corresponding operators, angular momentum and parity.

the correlator at finite temperature as follows:

$$
\begin{aligned}
G(x) &= \sum_m \langle m|A(x)A^\dagger(0)\mathrm{e}^{-\beta H}|m\rangle \\
&= \sum_n \sum_m \langle m|A(x)|n\rangle\langle n|A^\dagger(0)\mathrm{e}^{-\beta H}|m\rangle \\
&= \sum_n \sum_m \langle m|\mathrm{e}^{iHt}A(\vec{x},0)\mathrm{e}^{-iHt}|n\rangle\langle n|A^\dagger(0)\mathrm{e}^{-\beta H}|m\rangle \\
&= \sum_n \sum_m \langle m|\mathrm{e}^{H\tau}A(\vec{x},0)\mathrm{e}^{-H\tau}|n\rangle\langle n|A^\dagger(0)\mathrm{e}^{-\beta H}|m\rangle \\
&= \sum_n \sum_m \mathrm{e}^{E_m\tau}\mathrm{e}^{-E_n\tau}\langle m|A(\vec{x},0)|n\rangle\langle n|A^\dagger(0)|m\rangle\mathrm{e}^{-\beta E_m} \\
&= \sum_n \sum_m \mathrm{e}^{E_m(\tau-\beta)}\mathrm{e}^{-E_n\tau}\langle m|A(\vec{x},0)|n\rangle\langle n|A^\dagger(0)|m\rangle \\
&= \sum_n \sum_m \mathrm{e}^{E_m(\tau-\beta)-E_n\tau}G_n. \qquad (2.3)
\end{aligned}
$$

Here $A(x)$ is the hadron operator in question and $\beta = 1/T$ is the inverse temperature. The ground state energy gives the mass of the hadron. As the temperature increases and the particle dissociates the mass is no longer distinguishable. Calculating the energy spectrum from the correlators can therefore give an indication of the temperature at which the hadron melts.

In the first lattice studies of finite temperature correlators by DeGrand and DeTar it was suggested that hadronic modes could exist at temperatures above T_c [66]. The exponential decay at large distances gives rise to screening masses. Spatial correlators are particularly useful here as they are not restricted by the inverse temperature and can be studied at large separation. The spatial correlator is given by

$$G(z,T) = \int_0^{1/T} \mathrm{d}\tau \int \mathrm{d}x\mathrm{d}y \langle \mathcal{M}(x,y,z,\tau)\, \mathcal{M}(0,0,0,0)\rangle, \qquad (2.4)$$

where $\mathcal{M}$ is the meson operator defined in equation (2.2). They have been used to determine the screening masses of vector mesons at high temperature. Comparing these large-distance weak coupling calculations with lattice QCD studies can provide an understanding of the dissociation of the mesons in medium [67]. In recent years spatial correlation functions have also been used to study the in-medium modifications of the open charm mesons [68]. The screening masses calculated from spatial correlators have theoretically been

connected to the jet quenching observed in URHICs [69].

It has also been shown that at $T > T_c$ there are parity-doubled modes present, i.e. the pseudoscalar and scalar correlators become identical, as do the vector and axial vector [70]. This parity-doubling is a consequence of the fluctuation of the chiral condensate $\langle \bar{\psi}\ \psi \rangle$ [71] and is therefore an indicator of the restoration of chiral symmetry. Since this occurs at temperatures $\sim T_c$, correlators can be used to study the behaviour of hadrons at the deconfinement crossover.

Analysing the temporal correlators defined in equation (2.1) is more difficult as they are limited by the inverse temperature. However, since spatial and temporal correlators can give a different picture for physical quantities, it is important to have an understanding of the full space-time structure. Lattice QCD provides a means to study the temporal correlation functions. The properties of hadrons and thermal effects of the medium can be extracted by studying their corresponding spectral functions. A discussion of these objects follows in the next section.

2.2 Spectral Functions

Spectral functions $\rho(\omega)$ of hadronic operators are important in understanding the properties of hadrons in the QGP. They can be used to calculate many physical observables. A well-known example is the cross section of the $e^+ + e^-$ annihilation into hadrons, which is represented by the spectral function in the vector channel. It is expected that the medium effects will cause a spectral shift [72] and a parity duality in hadrons consistent with chiral symmetry restoration [73].

The spectral function is defined to be the imaginary part of the retarded correlator

$$\rho(\omega) \equiv \mathrm{Im}(D_R(\omega)) = D^{>}(\omega) - D^{<}(\omega), \tag{2.5}$$

where $D^{>}(\omega)$, $D^{<}(\omega)$ are the Fourier transforms of the forward and backward correlators respectively. These correlators are defined by $D^{>}(t,t') \equiv \langle \vec{\mathcal{M}}(t)\ \vec{\mathcal{M}}(t') \rangle \equiv D^{<}(t',t)$ for a meson operator $\mathcal{M}$. The spectral function of a propagating physical particle is positive definite, i.e. $\rho(\omega) \geq 0$.

In finite temperature calculations, analysing the correlation functions close to the critical temperature for deconfinement shows a noticable difference in the properties of the hadronic states between the confined phase and the QGP [74, 75, 76]. In order to discover if these changes are related to the dissociation of the hadrons one needs to study the structure of their corresponding spectral functions. Calculating the spectral functions of interacting particles is a difficult task. One must consider the imaginary time correlator. The Kubo-Martin-

Schwinger (KMS) condition states

$$D^{<}(\omega) = \mathrm{e}^{-\beta\omega} D^{>}(\omega), \tag{2.6}$$

where $\beta = 1/T$ is the inverse temperature. Applying this condition to equation (2.5), we obtain

$$\begin{aligned} \rho(\omega) &= D^{>}(\omega) - \mathrm{e}^{-\omega\beta} D^{>}(\omega) \qquad (2.7) \\ &= (1 - \mathrm{e}^{-\omega\beta}) D^{>}(\omega) \\ \Rightarrow D^{>}(\omega) &= \frac{\rho(\omega)}{(1 - \mathrm{e}^{-\omega\beta})}. \qquad (2.8) \end{aligned}$$

Taking an inverse Fourier transform, we get

$$D^{>}(t) = \int_{-\infty}^{\infty} \frac{\mathrm{d}\omega}{2\pi} \frac{\rho(\omega)\mathrm{e}^{-i\omega t}}{1 - \mathrm{e}^{-\omega\beta}}. \tag{2.9}$$

Now, rotating into imaginary time and using the fact that $\rho(\omega)$ is an odd function, we have that for $\tau \in [0, \beta]$,

$$\begin{aligned} G(\tau) = D^{>}(-it) &= \int_{-\infty}^{\infty} \frac{\mathrm{d}\omega}{2\pi} \frac{\mathrm{e}^{-\omega\tau}}{1 - \mathrm{e}^{-\omega\beta}} \rho(\omega) \\ &= \int_{-\infty}^{0} \frac{\mathrm{d}\omega}{2\pi} \frac{\mathrm{e}^{-\omega\tau}}{1 - \mathrm{e}^{-\omega\beta}} \rho(\omega) + \int_{0}^{\infty} \frac{\mathrm{d}\omega}{2\pi} \frac{\mathrm{e}^{-\omega\tau}}{1 - \mathrm{e}^{-\omega\beta}} \rho(\omega) \\ &= \int_{0}^{\infty} \frac{\mathrm{d}\omega}{2\pi} \left[\frac{\mathrm{e}^{\omega\tau}}{\mathrm{e}^{\omega\beta} - 1} + \frac{\mathrm{e}^{-\omega\tau}}{1 - \mathrm{e}^{-\omega\beta}} \right] \rho(\omega) \\ &= \int_{0}^{\infty} \frac{\mathrm{d}\omega}{2\pi} \frac{\mathrm{e}^{\omega\tau} + \mathrm{e}^{-\omega\tau}\mathrm{e}^{\omega\beta}}{\mathrm{e}^{\omega\beta} - 1} \rho(\omega) \\ &= \int_{0}^{\infty} \frac{\mathrm{d}\omega}{2\pi} \frac{\mathrm{e}^{\omega\tau} + \mathrm{e}^{-\omega\tau}\mathrm{e}^{\omega\beta}}{\mathrm{e}^{\omega\beta} - 1} \rho(\omega) \\ &= \int_{0}^{\infty} \frac{\mathrm{d}\omega}{2\pi} \frac{\mathrm{e}^{\omega\tau}\mathrm{e}^{-\omega\beta/2} + \mathrm{e}^{-\omega\tau}\mathrm{e}^{\omega\beta/2}}{\mathrm{e}^{\omega\beta/2} - \mathrm{e}^{-\omega\beta/2}} \rho(\omega) \\ &= \int_{0}^{\infty} \frac{\mathrm{d}\omega}{2\pi} \frac{\cosh[\omega(\tau - \beta/2)]}{\sinh(\omega\beta/2)} \rho(\omega) \\ &= \int_{0}^{\infty} \frac{\mathrm{d}\omega}{2\pi} K(\omega, \tau)\rho(\omega). \qquad (2.10) \end{aligned}$$

The function $K(\omega, \tau)$ is the standard finite temperature kernel, given explicitly in terms of the temperature T as

$$K(\omega, \tau) = \frac{\cosh[\omega(\tau - 1/2T)]}{\sinh(\omega/2T)}. \tag{2.11}$$

In the $T \to 0$ limit, this kernel reduces to $K(\omega, \tau) \to \mathrm{e}^{-\omega\tau}$ and the correlator is of the form of a standard Laplace transform. Solving for the spectral function $\rho(\omega)$ requires the use of an inverse Laplace transform. This problem is ill-defined and thus requires methods such as the Maximum Entropy Method to solve it. This is described in the next section.

2.3 The Maximum Entropy Method

While Monte Carlo methods on the lattice are sufficient to study static hadronic properties (e.g. correlators), it is more challenging to simulate dynamical quantities such as the spectral functions. This is due to difficulties in calculating the inverse Laplace transform, the statistical noise in the Monte Carlo data, and having a finite number of data points available in imaginary time on a lattice. In the next section we will discuss how to obtain the spectral function given the imaginary time correlator in equation (2.10). For this we employ the Maximum Entropy Method (MEM) as set forward by Asakawa et al [65]. The discussion of this method follows.

2.3.1 Construction of the Maximum Entropy Method

MEM is based upon Bayes' theorem from probability theory [77], which states

$$P[X|Y] = \frac{P[Y|X]P[X]}{P[Y]}, \tag{2.12}$$

where $P[X|Y]$ is the conditional probability of X given Y. In applying this to lattice QCD, we let D be the Monte Carlo data with errors and H be the accumulation of all prior knowledge of the spectral function ρ. Thus, Bayes' theorem tells us that the conditional probability of having the correct spectral function given the data is

$$P[\rho|DH] = \frac{P[D|\rho H]P[\rho|H]}{P[D|H]}. \tag{2.13}$$

Here, $P[D|\rho H]$ is known as the likelihood function and $P[\rho|H]$ is the prior probability. $P[D|H]$ is independent of ρ and is therefore simply a normalisation factor.

For a large number of Monte Carlo measurements (as is used in lattice QCD), the likelihood function obeys a Gaussian distribution and is given by

$$P[D|\rho H] = \frac{1}{Z_L}\mathrm{e}^{-L}, \tag{2.14}$$

$$\text{where } L = \frac{1}{2}\sum_{i,j}\left(D_i - G_i\right)C_{ij}^{-1}\left(D_j - G_j\right). \tag{2.15}$$

Here, i, j are the lattice data points, $D_i = \dfrac{1}{N_{\mathrm{cfg}}}\displaystyle\sum_{m=1}^{N_{\mathrm{cfg}}} D_i^m$ is the lattice data at the timeslice τ_i averaged over the gauge configurations, G_i is the usual imaginary time correlator defined in equation (2.10) at τ_i and C_{ij} is the covariance matrix defined by

$$C_{ij} = \frac{1}{N_{\mathrm{cfg}}(N_{\mathrm{cfg}}-1)}\sum_{m=1}^{N_{\mathrm{cfg}}}\left(D_i^m - D_i\right)\left(D_j^m - D_j\right). \tag{2.16}$$

C_{ij} is an $N \times N$ matrix, where $N = \tau_{max}/a - \tau_{min}/a + 1$ is the number of lattice data points for a lattice spacing a.

Now we'll look at the prior probability which is defined to be

$$P[\rho|H\alpha m] = \frac{1}{Z_S}\mathrm{e}^{\alpha S}, \tag{2.17}$$

where we write the known information α and $m(\omega)$ explicitly, though they're contained within H. S is the Shannon-Jaynes entropy

$$S = \int_0^\infty \left[\rho(\omega) - m(\omega) - \rho(\omega)\ln\left(\frac{\rho(\omega)}{m(\omega)}\right)\right]\mathrm{d}\omega. \tag{2.18}$$

The parameter α is introduced in order to regulate the weight of the entropy against the likelihood function in a self-consistent manner. It is a real and positive parameter which is integrated out in the MEM process. The function $m(\omega)$ is real-valued and positive-definite. It is known as the default model and is used to encode certain knowledge of the spectral shape. Since we are interested in the propagation of physical particles, we require $\rho(\omega) \geq 0$. Introducing $m(\omega) \geq 0$ ensures this. However, the resulting spectral function should not be dependent upon the default model.

Once the likelihood function and prior probability have been obtained, the probability of producing the spectral function can be calculated using equation (2.13). Given this conditional probability $P[\rho|DH\alpha m]$, the most probable

spectral function is the one that satisfies the condition

$$\frac{\delta P[\rho|DH\alpha m]}{\delta \rho} = 0, \tag{2.19}$$

and the reliabilty of the spectral function can be estimated using the second derivative,

$$\frac{\delta^2 P[\rho|DH\alpha m]}{\delta \rho^2}. \tag{2.20}$$

2.3.2 Procedure for Using MEM

The most robust algorithm for MEM is Bryan's method [78]. The procedure begins with finding the most probable spectral function for a given α. Combining equations (2.14) and (2.17) with the conditional probability formula in equation (2.13), we note that

$$P[\rho|DH\alpha m] \propto \frac{1}{Z_L Z_S} \mathrm{e}^{Q(\rho)}, \quad Q(\rho) \equiv \alpha S - L. \tag{2.21}$$

The most probable spectral function ρ_α is achieved by finding the maximum value for $Q(\rho)$. The method for this is laid out in more detail in Section 2.3.3. It can be shown [65] that this solution is unique.

Next, a weighted average over ρ and α is taken in order to obtain the final result for ρ. It is assumed that $P[\rho|DH\alpha m]$ is sharply peaked around ρ_α which should be the case for data with small errors. Thus, the final result is achieved by calculating the integral

$$\begin{aligned} \rho(\omega) &= \int [\mathrm{d}\rho] \int \mathrm{d}\alpha \; \rho(\omega) \; P[\rho|DH\alpha m] \; P[\alpha|DHm] \\ &\simeq \int \mathrm{d}\alpha \; \rho_\alpha(\omega) \; P[\alpha|DHm], \end{aligned} \tag{2.22}$$

where the measure is given by $[\mathrm{d}\rho] = \prod_{i=1}^{N_\omega} \frac{\mathrm{d}\rho_i}{\sqrt{\rho_i}}$ and $P[\alpha|DHm]$ can be calculated using Bayes' Theorem as

$$\begin{aligned} P[\alpha|DHm] &= \int [\mathrm{d}\rho] \; \frac{P[D|\rho H\alpha m] \; P[\rho|H\alpha m] \; P[\alpha|Hm]}{P[D|Hm]} \\ &\propto P[\alpha|Hm] \int [\mathrm{d}\rho] \; \frac{1}{Z_L Z_S} \mathrm{e}^{Q(\rho)}. \end{aligned} \tag{2.23}$$

There are two standard options for the prior probability of α — Laplace's rule ($P[\alpha|Hm] = $ constant) or Jeffrey's rule ($P[\alpha|Hm] = 1/\alpha$). The output should be insensitive to the choice, assuming that the probability is concentrated around its maximum. As the simpler of the two, Laplace's rule is usually adopted for lattice QCD.

In averaging over α, $P[\alpha|DHm]$ is renormalised such that

$$\int_{\alpha_{\min}}^{\alpha_{\max}} \mathrm{d}\alpha \; P[\alpha|DHm] \; = \; 1 \tag{2.24}$$

is satisfied in the region $\alpha \in [\alpha_{\min}, \alpha_{\max}]$. This region is determined by insisting that $P[\alpha|DHm] \geq 0.1P[\alpha_0|DHm]$ where α_0 is the maximum.

Once the spectral function $\rho(\omega)$ has been obtained, it is prudent to do an error analysis as there are correlations between $\rho(\omega)$ at neighbouring values of ω. A study of the sensitivity of the result on the default model $m(\omega)$ is also required. One simply varies the input function $m(\omega)$ and compares the resulting spectral functions. There should be no dependence on $m(\omega)$. In the absence of data, the default model is reproduced as the spectral function.

2.3.3 Maximising $Q(\rho)$

The main difficulty in applying MEM is finding a global maximum for the parameter $Q(\rho)$, defined in equation (2.21), which typically has $\mathcal{O}(10^3)$ degrees of freedom. Bryan showed that the singular value decomposition (SVD) of the kernel K reduces the search to a subspace of the order of the number of data points ($\sim \mathcal{O}(10)$)[78]. This has been the main method of maximising Q since MEM was adopted by lattice theorists.

To determine the spectrum from Monte Carlo data, we must first discretise ω into N_ω points, and consider $\rho_l \equiv \rho(\omega_l)$. Assuming the most probable spectral function is sharply peaked around ρ_α and imposing the extremum condition

$$\left.\frac{\delta Q}{\delta \rho}\right|_{\rho=\rho_\alpha} = 0, \tag{2.25}$$

with the imaginary time correlator in equation (2.10), we obtain the implicit expression for the spectral function ρ_l,

$$-\alpha \ln\left(\frac{\rho_l}{m_l}\right) = \sum_{i=1}^{N} K(\omega_l, \tau_i) \frac{\partial L}{\partial D_\rho(\tau_i)}, \tag{2.26}$$

where $\tau_i = i \cdot a$ is the i^{th} lattice data point. As we are interested in the propagation of physical particles, we can assume that ρ_l is positive definite. This allows us to parametrise it as $\rho_l = m_l \mathrm{e}^{a_l}$, and thus we obtain

$$\begin{aligned} -\alpha \ln\left(\frac{m_l \mathrm{e}^{a_i}}{m_l}\right) &= \sum_{i=1}^{N} K(\omega_l, \tau_i) \frac{\partial L}{\partial D_\rho(\tau_i)} \\ \Rightarrow -\alpha a_i &= \sum_{i=1}^{N} K(\omega_l, \tau_i) \frac{\partial L}{\partial D_\rho(\tau_i)}. \end{aligned} \tag{2.27}$$

This leads to the vector equation

$$-\alpha\vec{a} = K^t \frac{\partial \vec{L}}{\partial D_\rho}, \tag{2.28}$$

where K^t is the transposed kernel, which is an $N_\omega \times N$ matrix and $\dfrac{\partial \vec{L}}{\partial D_\rho}$ is an N dimensional column vector. The singular value decomposition is then applied to $K^t = U\Xi V^t$, where U is an $N_\omega \times N$ matrix satisfying $U^tU = 1$ and contains a full orthonormal basis, V is an $N \times N$ matrix satisfying $VV^t = V^tV = 1$ and Ξ is an $N \times N$ diagonal matrix with positive semi-definite entries. These entries are the singular values of the transposed kernel matrix K^t. The first N_s columns of the matrix U define an N_s dimensional singular space spanned by the columns $\{\vec{u_1}, ..., \vec{u_{N_s}}\}$, where N_s is the number of non-zero entries in Ξ. From this we find that $\vec{a}$ is in the singular space, and thus can be parametrised by a set of parameters $\{b_1, ..., b_{N_s}\}$ as

$$\vec{a} = \sum_{i=1}^{N_s} b_i \vec{u}_i; \qquad \text{i.e.} \qquad a_l = \sum_{i=1}^{N_s} b_i U_{li}. \tag{2.29}$$

This, in turn, leads to the parametrisation of the spectral function which is now determined by the parameters b_i,

$$\rho_l = m_l \exp\left(\sum_{i=1}^{N_s} b_i U_{li}\right). \tag{2.30}$$

2.4 Improving on Bryan's Algorithm

2.4.1 Modifications to the Finite Temperature Kernel

In finite temperature lattice calculations with MEM, it is a common issue that the spectral function reconstruction at the smallest non-zero ω is inconsistent with that of higher energies [79]. As $\omega \to 0$, the kernel in equation (2.11) may diverge, the basis functions become degenerate and MEM is unsuccessful in finding a valid spectral function. This affects the transport coefficients as they are calculated in this low frequency range. The behaviour of ω as it approaches zero depends on its discretisation, which indicates that the problem is in the method.

A solution to this was presented by Aarts et al in [80]. The divergence of the kernel can be counteracted by a simple modification:

$$\tilde{K}(\omega, \tau) = \frac{\omega}{2T} K(\omega, \tau). \tag{2.31}$$

We also get that

$$\tilde{\rho}(\omega) = \frac{2T}{\omega}\rho(\omega), \tag{2.32}$$

so that $\tilde{K}(\omega,\tau)\tilde{\rho}(\omega) = K(\omega,\tau)\rho(\omega)$. This modified kernel is used in place of $K(\omega,\tau)$ throughout the MEM process.

Alternatively, the hyperbolic sine in the denominator of the kernel presented in equation (2.11) can be replaced with the hyperbolic cosine to give

$$\hat{K}(\omega,\tau) = \frac{\cosh[\omega(\tau - 1/2T)]}{\cosh(\omega/2T)} = \tanh(\omega/2T)K(\omega,\tau), \tag{2.33}$$

$$\hat{\rho}(\omega) = \frac{1}{\tanh(\omega/2T)}\rho(\omega). \tag{2.34}$$

While there is no overall difference in the spectral shape, the use of $\cosh(\omega/2T)$ instead of $\sinh(\omega/2T)$ forces the kernel to be regular. In this thesis, we employ the use of the modification given in equation (2.31). In our first generation results presented in Chapter 3, we also modified the denominator of the kernel to the hyperbolic cosine, while in our second generation results (presented in Chapter 4) we used the hyperbolic sine.

2.4.2 Employing an Extended Search Space for the SVD Method

The accuracy of the resulting spectral function using the SVD method laid out by Bryan has recently been called into question [81]. It has been argued that the basis functions spanning the SVD subspace may not be enough to contain all the data. Choosing an initial value for ω, $\omega_{\min}$, which is both large and negative ensures that the singular value decomposition of the kernel in the MEM procedure fails. An extension of this subspace was proposed by Rothkopf in [81]. More columns of the matrix U are included in the parametrisation of ρ_l, so that equation (2.30) now reads

$$\rho_l = m_l \exp\left(\sum_{i=1}^{N_{\text{ext}}} U_{li} b_i\right), \tag{2.35}$$

with $N_s < N_{\text{ext}} < N_\omega$. The number of basis vectors one needs to add is determined by increasing N_{ext} until $Q(\rho)$ reaches an absolute maximum.

The reconstruction of the spectral function peak positions and their widths shows improved accuracy when using $N_{\text{ext}} > N_s$. Choosing N_{ext} too small induces errors as the reconstruction overestimates the peak position due to an insufficient number of degrees of freedom. Mock analysis of this method has shown that the features of the spectral function are readily available, but

the added basis functions introduce extra wiggly patterns. The extra artifacts are identifiable by a study of the dependence of $\rho(\omega)$ on the prior information $m(\omega)$. Employing this extended search space has had a positive effect for MEM calculations for non-relativistic QCD and the static quark potential.

2.4.3 Applying Bryan's Algorithm with a Fourier Basis

In our study of finite temperature QCD with charmed mesons, we discovered that even with the extension of the search space, the basis functions were not correctly reproduced. We then abandoned the SVD method and chose a Fourier basis parametrisation for ρ_l instead [82]. This parametrisation is given by

$$\rho_l = m_l \exp\left[a_1 + \sum_{i=1}^{N_{\text{ext}}/2} a_{2i} \sin[(\omega_l - \omega_{\min})i] + \sum_{i=1}^{N_{\text{ext}}/2} a_{2i+1} \cos[(\omega_l - \omega_{\min})i]\right]. \tag{2.36}$$

The advantage to using a Fourier basis is that there is an analytic formula we can employ to calculate the basis functions, as they are now in terms of sines and cosines, and therefore the SVD is not necessary. We also note that the choice of $\omega_{\min}$ has no effect on the resulting spectral function. This choice of basis yields a more robust determination of $\rho(\omega)$. In our application of this method for the charmonium and D meson correlators, $\omega_{\min} = 0$ by construction.

2.5 Alternative Methods

While the results in this thesis have been calculated using MEM, it is worth noting that there are a number of other methods available for the calculation of spectral functions. Most recently, a novel Bayesian Reconstruction (BR) approach to reconstructing spectral functions has been devised by Burnier and Rothkopf [83]. It addresses several issues affecting MEM, namely its slow convergence for large search spaces, scale dependence in the default model and the Gaussian approximation in the estimation of α. It also aims to be far less computationally expensive. One of the main features of this new method is an updated entropy term. The Shannon-Jaynes entropy in MEM is replaced with

$$S = \alpha \int \mathrm{d}\omega \left(1 - \frac{\rho(\omega)}{m(\omega)} + \ln\left(\frac{\rho(\omega)}{m(\omega)}\right)\right), \tag{2.37}$$

where α is a positive parameter introduced in order to give a dimensional meaning to the integral, $\rho(\omega)$ is the spectral function and $m(\omega)$ is the prior information. While MEM averages over its α parameter, this BR method integrates it out from the joint probability distribution $P[\rho, D, \alpha, m]$. Tests on mock data have been carried out and a number of early results for bottomonium

and the static quark potential in lattice QCD have emerged [84, 85, 86].

Before the introduction of MEM, the most widely used method for the calculation of spectral functions involved assuming certain ansätz about its shape, and fitting the data to this image. This method is still in use, though not as commonplace as it once was. To implement it, it is assumed that the spectral function is composed of (for example) a delta peak, a Breit-Wigner peak, a Lorentzian peak, or a combination of all three. A continuum component is added and the correlator data are fitted to this function. In recent times it has been used to evaluate finite temperature correlators in 2 flavour QCD [87] and electrical conductivity in quenched QCD [88].

Other options include the Backus-Gilbert method, a regularisation method which imposes stability constraints in order to ensure the variation in the spectral function is minimal. This has been applied in [89, 90]. There is also the Tikhonov method with Morozov discrepancy principle, which is a linear regularisation method enforcing smoothness on the spectral function. Its main advantage over MEM is its ability to calculate non-physical spectral densities like those of confined gluons. This method is in use in [91, 92]. Alternatively, there is the method proposed by Cuniberti et al in [93] which analyses the analytic continuation from imaginary time correlators to real time correlators within a certain limit. This is employed in lattice studies in [94, 95].

Chapter 3

Charmonium Spectral Functions at Finite Temperature and Momentum

3.1 Introduction

3.1.1 The Importance of Momentum

In studying the properties of the QGP one expects to observe a significant suppression of J/ψ particles which signals deconfinement [32]. This pattern is thought to originate from the colour screening of the binding force of charmonium states. As such, a sequential suppression pattern is anticipated with the most loosely bound quarkonia states melting before their more tightly bound counterparts. Higher excitations of J/ψ will dissociate before the ground state. The decay products of these higher excitations contribute to the observed yield of quarkonia in the QGP [96]. The range of the colour screening radius is inversely proportional to the temperature. As such, the dissociation of J/ψ provides a gauge with which to measure the temperature of the medium.

The leakage effect on J/ψ production may also affect the suppression pattern. During the time taken for the quarkonium particles to dissociate in the QGP, the J/ψ particles with high transverse momentum leak out of the source of suppression and survive in the medium. The particles with low transverse momentum are absorbed [97].

In collider experiments, charm quarks are only produced in the initial collison. The creation of charmonium mesons from uncorrelated $c\bar{c}$ pairs can enhance the yield of J/ψ particles and hence affect its transverse momentum spectrum [98]. It is sensible to examine the momentum effects of $c\bar{c}$ hadrons in the QGP.

We present a lattice study of the J/ψ spectral functions. The lattices are

isotropic in space and momentum is treated equally in all spatial dimensions. However, in a collider, the particles move in one dimension along the beam axis. The momentum of a particle in a collider can be considered in the forms of its transverse momentum p_T which is directed towards the plane perpendicular to its motion, and rapidity y which follows the beam axis and is defined to be

$$y = \frac{1}{2} \ln \frac{E + p_z c}{E - p_z c}, \tag{3.1}$$

where E is the energy, p_z is the momentum along the beam axis and c is the speed of light. A first study of the momentum dependence of the survival of charmonium may be found in reference [99].

3.1.2 Transport Coefficients

A study of charmonium particles at non-zero momentum may give insight into the behaviour of their spectral functions as $\omega \to 0$. This low frequency region is important in the study of the transport coefficients of the QGP as they are related to the low frequency behaviour of real time correlators using Kubo formulae [100]. The transport coefficients of the medium, namely the heavy quark diffusion and electrical conductivity, may be derived from the low frequency limit of the vector meson spectral functions. Other transport coefficients may be calculated from the correlators of gluonic operators, for example the shear and bulk viscosities [101]. A transport coefficient k may be calculated using the Green-Kubo formula

$$k = \pi \lim_{\omega \to 0} \frac{\rho(\omega, \vec{p} = \vec{0})}{\omega}, \tag{3.2}$$

where $\rho(\omega, \vec{p} = \vec{0})$ is the spectral function for the given operator at zero momentum.

The electrical conductivity is the most studied transport coefficient as its Euclidean correlator can be computed to a high precision. Previous lattice studies of the conductivity may be found in references [102, 103, 87, 104, 105]. However, the heavy quark diffusion coefficient is more difficult to ascertain. For sufficiently heavy quarks, the transport peak obtained in the spectral function is too narrow to apply the same tactics as with the conductivity.

The heavy quark diffusion coefficient D is defined using equation (3.2) as follows

$$D = \frac{1}{6\chi_s} \lim_{\omega \to 0} \sum_{i=1}^{3} \frac{\rho_{ii}^V(\omega, \vec{p} = 0, T)}{\omega}, \tag{3.3}$$

where χ_s is the quark number susceptibility which is defined through the zeroth component of the temporal correlator in the vector channel [106]. When this

coefficient is small, $D \simeq 1/(2\pi T)$, the low energy portion of the vector correlator shows a very small τ-dependence. Linear response theory can be used to connect Langevin dynamics and the diffusion equations to the current-current correlator [107].

In order to calculate the heavy quark diffusion coefficient, the current-current correlator is decomposed into its transverse and longitudinal components as follows

$$C_{JJ}^{ij}(\omega, \vec{p}) = \left(\frac{p_i p_j}{p^2} - \delta_{ij} \right) C_{JJ}^{T}(\omega, \vec{p}) + \frac{p_i p_j}{p^2} C_{JJ}^{L}(\omega, \vec{p}). \tag{3.4}$$

Due to conservation of current, the density-density correlator can be related to the longitudinal component of C_{JJ}

$$\frac{\omega^2}{p^2} C_{NN}(\omega, \vec{p}) = \frac{p_i p_j}{p^2} C_{JJ}^{ij}(\omega, \vec{p}) = C_{JJ}^{L}(\omega, \vec{p}). \tag{3.5}$$

The heavy quark diffusion coefficient is related to this density-density correlator. For timescales much larger than $1/\eta$ where η is the momentum drag coefficient, the heavy quark number N obeys the diffusion equation

$$\partial_t N + D\nabla^2 N = 0. \tag{3.6}$$

The drag coefficient can be related to the diffusion coefficient using the Einstein relation

$$D = \frac{T}{m_Q \eta}, \tag{3.7}$$

where T is the temperature and m_Q is the heavy quark mass. Since the time scale for heavy quark transport m_Q/T^2 is larger than that of the light quarks the Langevin formalism may be used to describe the thermalisation of charm quarks [28]. This method is utilised by Petreczky and Teaney in [107] to provide a density-density correlator of the form

$$C_{NN}(\omega, \vec{p}) = \chi_s(\vec{p}) \int_0^\infty \mathrm{d}t \; \mathrm{e}^{i\omega t} p^2 D (1 - \mathrm{e}^{-\eta t}) \; \mathrm{e}^{-p^2 D t + (p^2 D/\eta)(1 - \mathrm{e}^{-\eta t})}, \tag{3.8}$$

where $\chi_s(\vec{p})$ is the static susceptibility. From this we may deduce that for small momenta $\vec{p}$ such that $Dp^2 \ll \eta$ the integrand reduces to $p^2 D(\mathrm{e}^{-p^2 D t} - \mathrm{e}^{-\eta t})$ and performing the integration reveals

$$C_{NN}(\omega, \vec{p}) = \frac{\chi_s(\vec{p}) D p^2}{-i\omega + D p^2} - \frac{\chi_s(\vec{p}) D p^2}{-i\omega + \eta}. \tag{3.9}$$

The transport information is encoded in the low frequency region of the spectral function. Thus we are particularly interested in frequencies $\omega \sim Dp^2$. In this range the first term dominates and resembles the diffusion operator $(\partial_t + D\nabla^2)^{-1}$. At zero momentum the current-current spectral function in this region may be

computed to be

$$\frac{\rho_{JJ}(\omega,\vec{0})}{\omega} \equiv \frac{1}{\pi}\frac{\mathrm{Im}C_{JJ}(\omega,\vec{0})}{\omega} = \chi_s \frac{T}{m_Q}\frac{1}{\pi}\frac{\eta}{\omega^2+\eta^2}. \tag{3.10}$$

Previous studies have calculated the heavy quark diffusion coefficient using a number of methods – lattice gauge theory [108, 109], perturbative calculations [110] and $\mathcal{N}=4$ Yang-Mills theory [111]. A range for the value of the heavy quark diffusion coefficient was concluded to be

$$D = (0.5 - 1.0)/T. \tag{3.11}$$

This value is much smaller than that which was predicted by the perturbative estimate [28]. However, it is in accordance with the range used in phenomenological models [29].

3.1.3 Outline

In this chapter I present the results for the spectral functions of the J/ψ particle at both zero and non-zero momentum. The vector current was decomposed into its transverse and longitudinal polarisations as in equation (3.4) and the two components were analysed independently. A study of the low frequency region of these spectral functions is presented with a view towards calculating the heavy quark diffusion coefficient.

The spectral functions were computed using Bryan's algorithm in the Maximum Entropy Method detailed in Section 2.3 with the modified kernel presented in equation (2.31). These results were computed on a set of anisotropic lattices with 2 dynamical flavours of fermions. Full details of the ensembles are presented in the next section.

3.2 Formulation

I have simulated charmonium spectral functions on a set of ensembles with two degenerate flavours of dynamical quarks with $m_\pi/m_\rho = 0.54$ which corresponds approximately to the strange quark mass. This is a highly anisotropic set of lattices with spatial lattice spacing $a_s = 0.162$ fm and an anisotropy of $\xi = 6$. The full set of lattice parameters are given in Table 3.1.

A Two-plaquette Symanzik Improved gauge action as defined in equation (1.27) and a fine-Wilson, coarse Hamber-Wu fermion action with stout-link smearing as in equations (1.28), (1.29) were employed. Both the light sea quarks and the heavy valence quarks are computed using the same fermion action although the charm quark anisotropy was tuned separately [112]. The

Param	Gen 1
N_f	2
a_s (fm)	0.162
a_τ (fm)	0.0268
a_τ^{-1} (GeV)	7.35
ξ	6.03
T_c (MeV)	219
m_π/m_ρ	0.54

Table 3.1: Lattice parameters for the first generation of lattices.

critical temperature was estimated to be $T_c = 219$MeV for this set of ensembles. The lattice volumes and their relationship to T_c are given in Table 3.2. This corresponds to the "first generation" of ensembles of the FASTSUM Collaboration.

$N_s \times N_\tau$	T (MeV)	T/T_c	N_{cfg}
$12^3\times$ 16	459	2.09	1000
18	408	1.86	700
20	368	1.68	1000
24	306	1.39	500
28	263	1.20	1000
32	230	1.05	875
80	92	0.42	250

Table 3.2: Lattice size, temperature and number of configurations for the 1st generation of lattices.

The momentum values are given by

$$p^2 = \left(\frac{2\pi}{a_s N_s}\right)^2 n^2, \tag{3.12}$$

where $n^2 = n_x^2 + n_y^2 + n_z^2 = 0, 1, 2, 3, 4$, which corresponds to momentum values of $p = 0, 0.66, 0.93, 1.14, 1.32$ GeV respectively. Due to discretisation effects, the local current is not conserved and must be renormalised by a factor $Z_V(g^2)$ which depends on the square of the strong coupling [113]. However, since the masses of our quarks are degenerate, there is an exact vector symmetry which produces a conserved Noether current. A conserved current requires no renormalisation.

The spatial component of the conserved current for the Hamber-Wu action is given in equation (3.13). Here $r_A = 6s = 6/8$, where $s = 1/8$ is the spatial

Wilson parameter. The temporal component is the usual conserved Wilson current, which is described in equation (3.14), where r is the usual Wilson parameter and we set $r = 1$ by construction.

$$\begin{aligned} V_i^A(x) = &-\frac{2}{3}\bar{\psi}(x)(r_A - \gamma_i)U_i(x)\psi(x+\hat{\imath}) + \frac{2}{3}\bar{\psi}(x+\hat{\imath})(r_A + \gamma_i)U_i^\dagger(x)\psi(x) \\ &+ \frac{1}{12u_s}\Big[\bar{\psi}(x)(2r_A - \gamma_i)U_i(x)U_i(x+\hat{\imath})\psi(x+2\hat{\imath}) + (x \to x - \hat{\imath})\Big] \\ &- \frac{1}{12u_s}\Big[\bar{\psi}(x+\hat{\imath})(2r_A + \gamma_i)U_i^\dagger(x)U_i^\dagger(x-\hat{\imath})\psi(x-\hat{\imath}) + (x \to x + \hat{\imath})\Big]. \end{aligned} \tag{3.13}$$

$$V_t(x) = \frac{1}{2}[\bar{\psi}(x+\hat{t})(r + \gamma_0)U_t^\dagger(x)\psi(x) - \bar{\psi}(x)(r - \gamma_0)U_t(x)\psi(x+\hat{t})]. \tag{3.14}$$

3.3 Spectral Functions at Zero Momentum

Using the Maximum Entropy Method, I determined the spectral functions for both the longitudinal and transverse components of the conserved vector current at different temperatures and momenta with the following default models,

$$m(\omega) = m_0, \tag{3.15}$$

$$m(\omega) = m_0\omega^2, \tag{3.16}$$

$$m(\omega) = m_0\omega(m_1 + \omega). \tag{3.17}$$

In each case, m_0 is an overall normalisation parameter. In calculating the integral to obtain the imaginary time correlator in equation (2.10) with the kernel given in equation (2.11), the result is fitted to the correlator and the best approximation for m_0 is produced.

Our interest lies in the low frequency region of the spectral function as we are aiming to calculate the diffusion coefficient. Thus, the default model presented in equation (3.17) is the most useful. It provides insight into the $\omega \to 0$ region without the spectral shape being dominated by systematic errors. It has the benefit of matching the ω-dependence at large ω due to perturbative effects in continuum theory. It also yields a non-zero intercept at $\rho(\omega)/\omega$ as $\omega \to 0$ and thus provides a transport peak. The constant default model in equation (3.15) is divergent at $\omega \to 0$ and the quadratic default model in equation (3.16) converges to 0. As $\omega \to 0$, τ is large and there are very few data points. As such, MEM struggles to overcome the default model in this region.

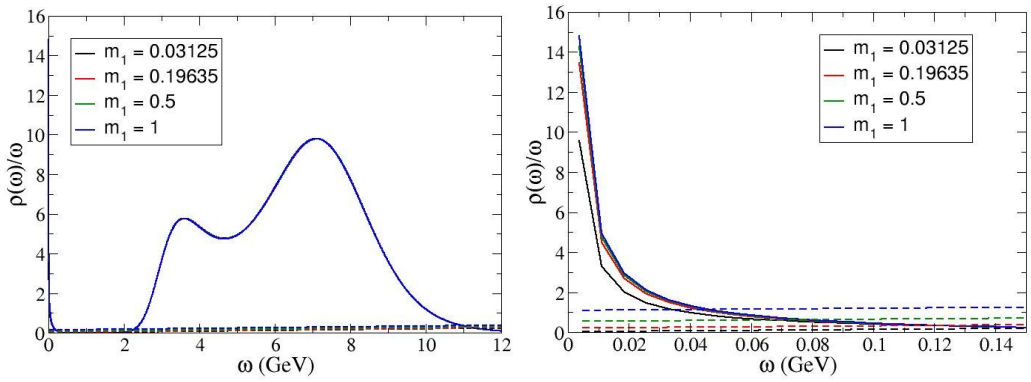

Figure 3.1: Analysis of the variation of m_1 in the default model $m(\omega) = m_0\omega(m_1 + \omega)$ for J/ψ at temperature $T/T_c = 1.05$ and zero momentum. The left panel shows the full spectral function obtained and the right panel focuses on the low frequency range. The dashed lines represent the default model in the absence of data.

These two default models are not good candidates for obtaining a transport peak at low frequency. We will therefore concentrate on $m(\omega)$ given in equation (3.17). The first two timeslices were discarded in the analysis since these will be dominated by lattice artifacts.

In equation (3.17), the parameter m_1 is chosen to be $m_1 = 1$. An investigation into the best choice of parameter was carried out. Figure 3.1 shows the results obtained when m_1 is varied for the vector current correlator at temperature $T/T_c = 1.05$ and zero momentum. The parameter $m_0 = 1.09375$ was kept constant throughout. The left panel shows the full spectral function. The overall shape is unaffected by the choice of m_1. However, when focusing on the low frequency region of the spectral function we see a difference in the transport peak. Setting $m_1 = T = 0.03125$ produces a transport peak which is significantly lower than the other three values. The peak becomes much more stable with the larger values of m_1. This finding is reflected in the results obtained by Aarts et al in [105].

Figure 3.2 shows the spectral functions obtained for momentum $p = 0$ for each temperature. A peak structure is evident for the lowest two temperatures $(T/T_c = 1.05, 1.20)$ indicating the ground state energy of the J/ψ particle is at that value. The peaks lie at a slightly higher value than the J/ψ mass, which is represented by the dashed vertical line in the plot. However, taking into consideration the width of the peaks, we can say that the J/ψ meson appears to be present in the medium at these temperatures. For the higher temperatures we see no evidence of a peak, suggesting that the J/ψ particle melts at approximately $1.2 - 1.4T_c$, in agreement with previous charmonium studies [106, 114]. J/ψ was found to melt at a slightly higher temperature of $T = 1.6 - 1.9T_c$ in [115] which is reasonably consistent with our result. The local vector current for the same set of ensembles yielded a dissociation temperature

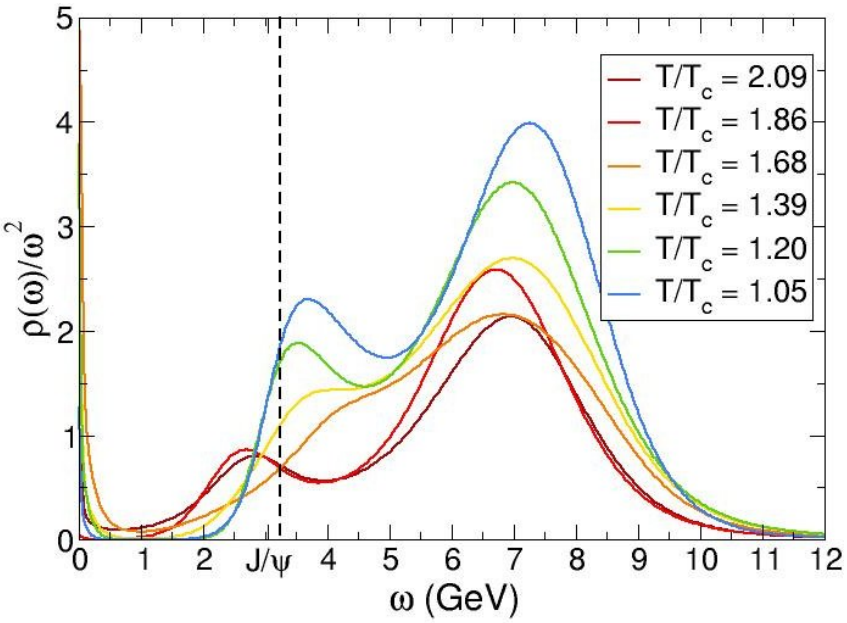

Figure 3.2: Spectral functions for each temperature with $p^2 = 0$. The vertical line represents the experimental value for the J/ψ mass.

of $T = 1.7T_c$ [99]. Aarts et al calculated that J/ψ would also dissociate at $T = 1.7T_c$ on the forerunner to our first generation ensembles with lattice size $8^3 \times N_\tau$ using the local current [112]. Although the exact temperature at which the J/ψ melts is unclear, it seems certain that the particle survives at temperatures exceeding the critical temperature for deconfinement. The secondary peak can be attributed to lattice artifacts.

It should be noted that the uncertainty in the MEM procedure increases as the temperature increases, and it is therefore not possible to say with certainty that the pattern observed at the higher temperatures is genuine or merely reflects the inability of the MEM algorithm to determine the spectral function given the available data. The systematic errors appear to be too large to give conclusive evidence of a melting J/ψ bound state. This remains the case for all momenta.

The spectral functions obtained with each default model for the highest temperature $T/T_c = 2.09$ at zero momentum are presented in Figure 3.3. A stable peak at the correct value for the ground state is apparent for $m(\omega) = m_0\omega^2$. However, the other two default models provide different peak structures, rendering the results unreliable. Only 6 temporal data points are available for this temperature, allowing the systematic uncertainties to dominate.

I also carried out a study of the dependence of the spectral shape on the default model for the higher temperatures. The results are very encouraging. Figure 3.4 shows the spectral functions calculated with each of the default models given in equations (3.15)–(3.17) for the J/ψ particle at temperature $T/T_c = 1.05$ and zero momentum. The free parameters were set to $m_0 = 1.09375$

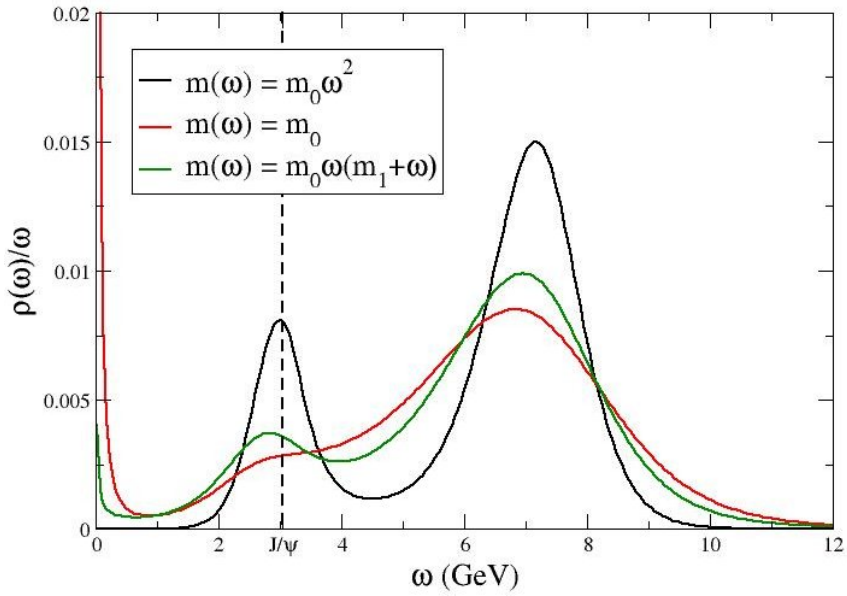

Figure 3.3: Spectral functions for J/ψ at $T/T_c = 2.09$ with zero momentum obtained using three different default models.

and $m_1 = 1$. The spectral functions have no discernible differences and as such we can be confident that our choice of $m(\omega)$ has no affect on our results.

I also conducted a study of the dependence of the spectral shape on the parameter m_0. Figure 3.5 shows the results of varying m_0 in the default model $m(\omega) = m_0\omega(m_1 + \omega)$ for $T/T_c = 1.05$ with zero momentum. The parameter $m_1 = 1$ was fixed. The optimum choice $m_0 = 1.09375$ was increased and decreased by a factor of 10. There is no overall change in the spectral shape. The ground state peak is in the same position with a similar width for each value of m_0. We can be confident that our results for $p = 0$ are not reliant on the parameter m_0.

3.4 Spectral Functions at Finite Momentum

At nonzero momentum, the vector meson correlator is decomposed into its transverse and longitudunal polarisations as in equation (3.4). The transversely and longitudinally polarised J/ψ may in principle behave differently in a QGP medium. I have therefore analysed the two separately.

The spectral functions for the lowest two temperatures are presented here. Figure 3.6 shows the spectral functions for the longitudinal component of the current for a range of momenta at $T/T_c = 1.20, 1.05$. The J/ψ mass is given by the dashed vertical line. Although the highest momentum value $p = 1.32$ GeV appears to give a peak structure at the J/ψ mass, it is unreliable. The inability of MEM to reconstuct this peak at lower momentum is an indication of the uncertainty of these results. At $T/T_c = 1.20$ there is a stable peak structure evident for $p = 0.66$ GeV. It appears as though this peak melts with increasing

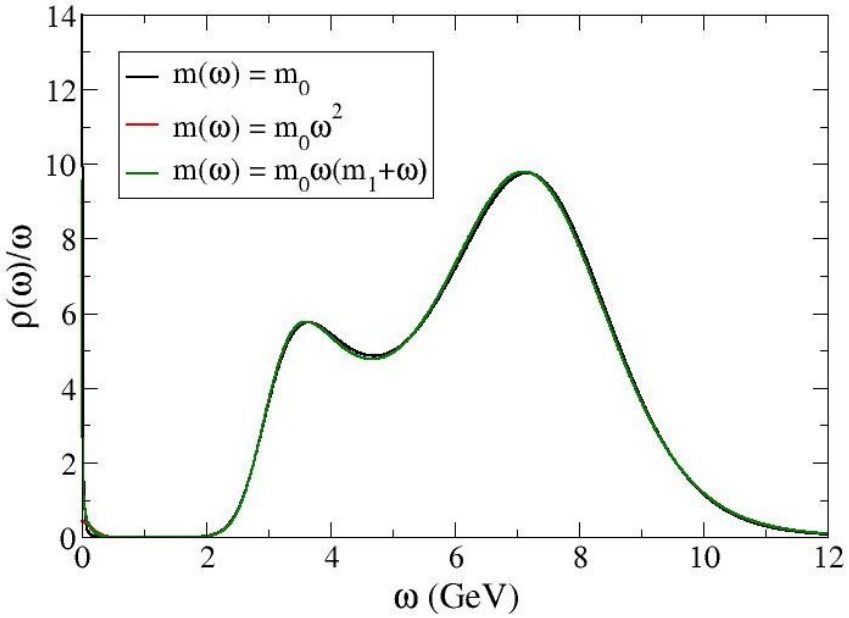

Figure 3.4: Variation of $m(\omega)$ for the J/ψ particle on the $T/T_c = 1.05$ lattice at zero momentum.

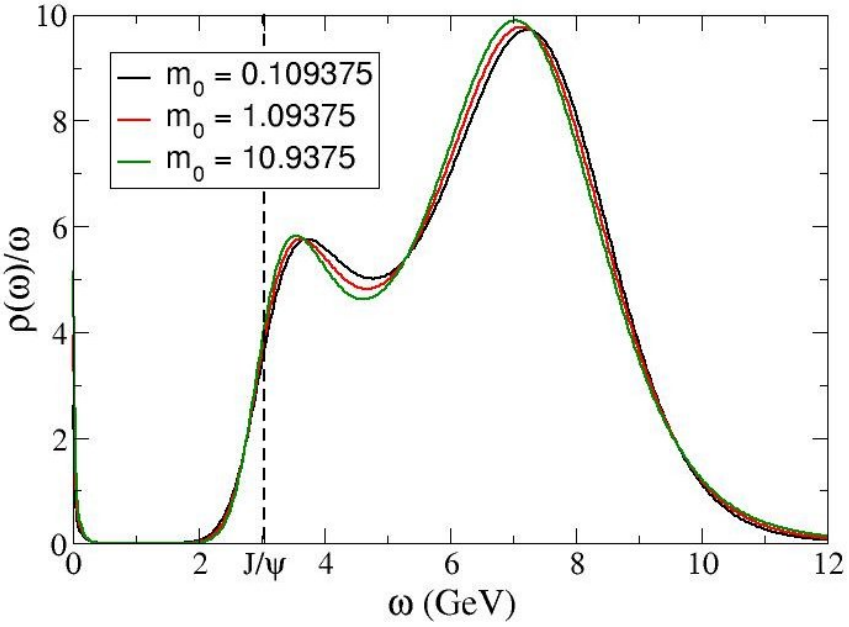

Figure 3.5: Variation of the normalisation parameter m_0 in $m(\omega) = m_0\omega(m_1+\omega)$ for $T/T_c = 1.05$ with $p = 0$.

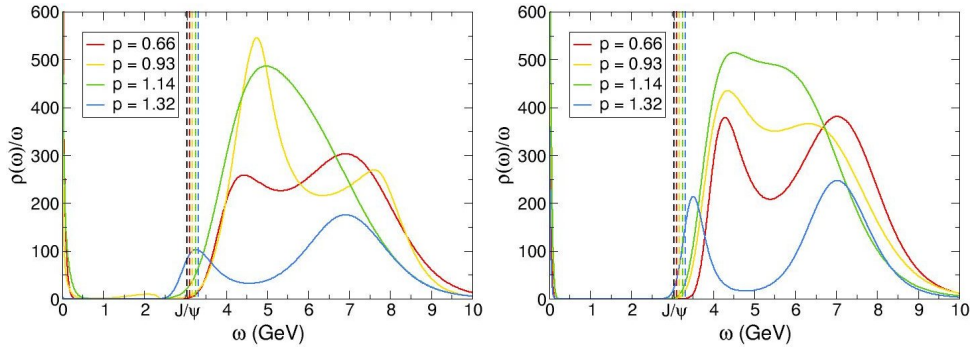

Figure 3.6: Spectral functions for the longitudinal polarisation of the conserved vector current at the lowest two temperatures with finite momentum (in GeV). $T/T_c = 1.20$ is the panel on the left and $T/T_c = 1.05$ is on the right. The dashed vertical lines indicate the mass of J/ψ at each given momentum.

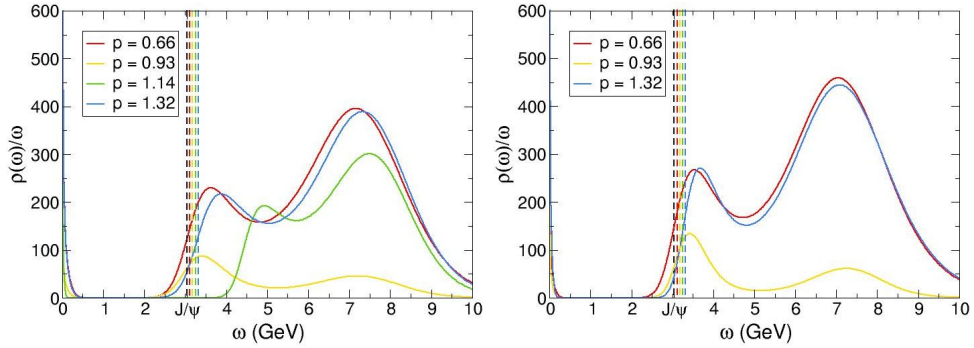

Figure 3.7: Spectral functions for the transverse polarisation of the conserved vector current at the lowest two temperatures with finite momentum (in GeV). $T/T_c = 1.20$ is the panel on the left and $T/T_c = 1.05$ is on the right. The dashed vertical lines indicate the mass of J/ψ at each given momentum.

momentum. A similar picture is presented for $T/T_c = 1.05$. The peak structure survives to $p = 0.93$ GeV. Unfortunately the uncertainty in the correlators and the systematic errors are too large to make a claim on the survival of the J/ψ meson with any level of certainty.

The longitudinal component of the current is expected to produce a peak structure in the low frequency region. This is discussed in more detail in Section 3.5. This structure is not apparent in Figure 3.6. As seen in Figure 3.1, $m(\omega)$ itself provides a small intercept with the $\rho(\omega)/\omega$ axis. The intercept of the spectral functions from the longitudinal component is on a much larger scale and it is therefore difficult to directly compare them. However, the shape of the intercept is consistent with the default model. This suggests that in this region, the MEM is not sufficiently capable of reproducing the correct transport peak due to the small number of data points.

In Figure 3.7 the transverse component is presented for the same temperatures. A peak structure is visible across all momenta for both temperatures. These peaks appear to be more stable than their longitudinal counterparts, with the exception of $p = 1.14$ GeV. For $T/T_c = 1.20$ this momentum gives a

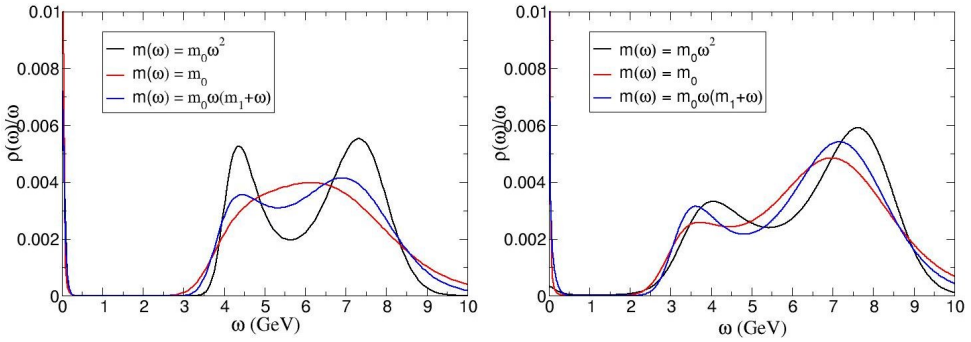

Figure 3.8: Spectral functions for the conserved vector current at $T/T_c = 1.20$ for the longitundinal (left) and transverse (right) polarisations at momentum $p = 0.66$ GeV calculated with different default models.

very different picture than what is expected and for $T/T_c = 1.05$ we simply could not get a sensible result. Again, the uncertainties appear to be too large to give any accurate insights into the melting of bound charmed states, or how momentum affects it. However, in both the transverse and longitudinal polarisations a transport peak is evident as $\omega \to 0$. While the exact location of the peak may not be trustworthy, it may provide a bound on the value of the transport coefficients. This low frequency region is explored in Section 3.5.

As with the $p = 0$ results, it is prudent to check the systematic errors involved in the MEM process. Figure 3.8 shows the results of varying the default model for each of the longitudinal (left) and transverse (right) polarisations of momentum $p = 0.66$ GeV at temperature $T/T_c = 1.20$. The spectral function was calculated using MEM with each of the prior functions listed in equations (3.15) – (3.17). The longitudinal component of the current appears to have a great dependence on the choice of default model. This is not a desirable outcome and could explain the difficulties in extracting a reasonable result from these correlators. The spectral shape is inconsistent across each $m(\omega)$. While the constant default model does not find any peak structure, the other two models at least have the peak in the same position.

The spectral functions for the transverse component of the correlator, in the right panel of Figure 3.8, are much more consistent. The peaks are in approximately the same position with the same height. As such the transverse component's results are more reliable. The peak is not sharp and thus could be an indication of the early stages of J/ψ melting.

For the higher temperature lattices I was not able to gain stable results. In the previous section we saw that the $T/T_c = 2.09$ results are not reliable at $p = 0$. Here, we consider the same temperature at finite momentum. Figure 3.9 shows the spectral functions for $T/T_c = 2.09$. The longitudinal polarisation of the vector current is presented in the left panel. There is no clear peak structure of any kind in the region of the J/ψ mass. While this could indicate

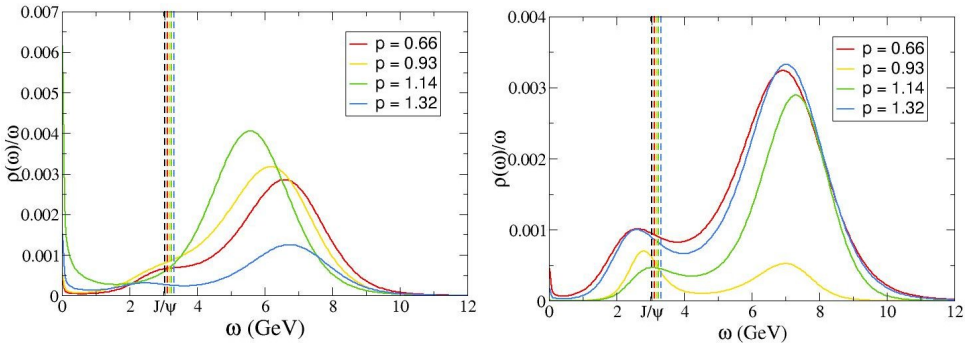

Figure 3.9: Spectral functions for J/ψ at $T/T_c = 2.09$ with finite momentum. The longitudinal polarisation of the current is on the left and the transverse polarisation is on the right. The dashed vertical lines indicate the mass of J/ψ at each given momentum.

that the particle has melted, it is probable that the uncertainties involved are affecting the results. The longitudinal polarisation has not provided stable results in general. The transverse component of the current (in the right panel) appears to have a peak structure at all momenta. In general, the transverse results are more reliable but in this case it is likely that the peak is an effect of the MEM procedure.

Again, the default model of most interest to us is $m(\omega) = m_0\omega(m_1 + \omega)$. A finite momentum study in the variation of the parameter m_0 was conducted. Figure 3.10 shows these results for $T/T_c = 1.05$ at $p = 0.66$ GeV, again separating the longitudinal (left) and transverse (right) components. The longitudinal polarisation reproduces a stable peak in the same position for each value of m_0. The width of the peak suggests that the position is accurate, but we can clearly see that its location is ~ 1 GeV higher than expected. Also, the height of each peak is significantly different. This suggests that m_0 has a considerable effect on the overall normalisation of the spectral function, which is not desirable. Again, the transverse polarisation yields far more reliable results. A stable peak is obtained with a roughly equal height from each default model. The width of each peak allows for their position to be a little higher than expected.

3.5 Low Frequency

Our objective is to calculate the diffusion transport coefficient, and thus we are interested in the low frequency region of the spectral functions. Previous results in this sector show a stable transport peak shifted away from $\omega = 0$ at finite momentum [107]. Figure 3.11 shows this region for a temperature of 230 MeV (1.05 T_c) and a mometum $p = 0$. Each of the three default models presented in Section 3.3 are represented here, with $m_0 = 1.09375$ and $m_1 = 1$.

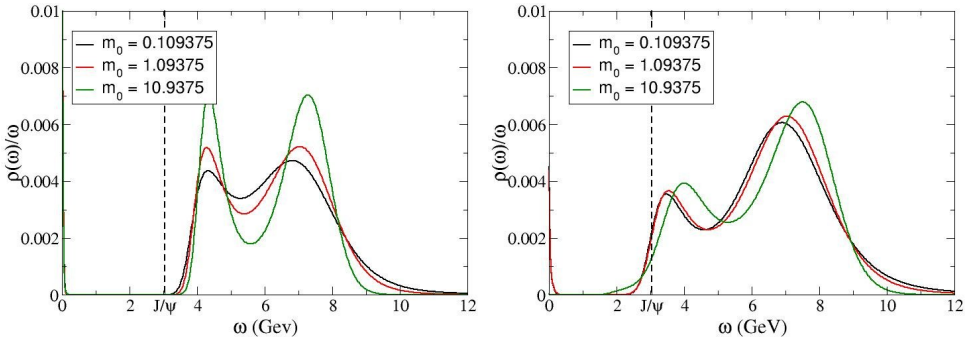

Figure 3.10: Testing the variation of m_0 in the default model $m(\omega) = m_0\omega(m_1 + \omega)$ using spectral functions for the conserved vector current at $T/T_c = 1.05$ for the longitudinal (left) and transverse (right) polarisations at momentum $p = 0.66$ GeV.

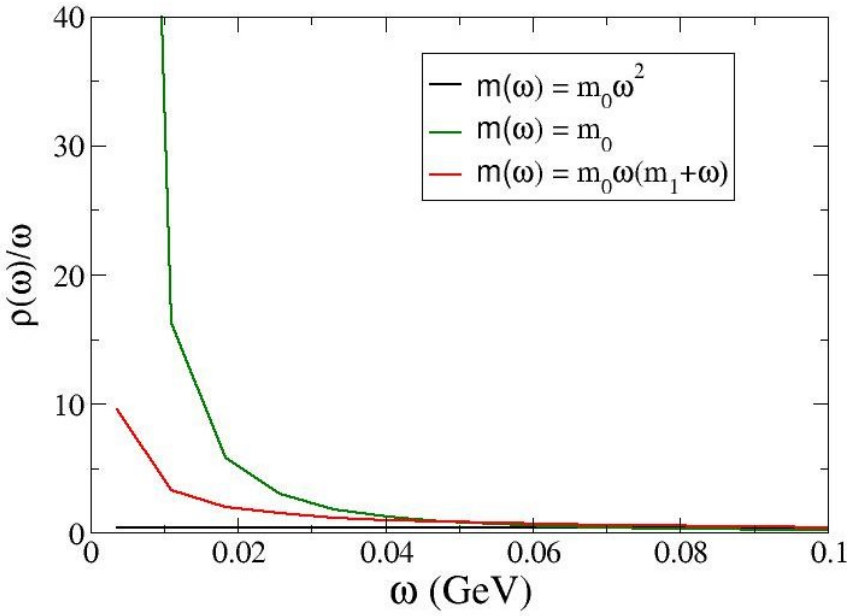

Figure 3.11: Low frequency region of spectral function from the $T/T_c = 1.05$ at zero momentum calculated with $N_\omega = 5000$.

The first of these, $m(\omega) = m_0$, yields an intercept with a large value for $\rho(\omega)/\omega$, while the second, $m(\omega) = m_0\omega^2$, appears to converge to zero. This behaviour is expected as these default models dominate over the data in the spectral shape at low frequency. They will give extreme upper and lower bounds on the value of a transport peak in this region. The default model we are most interested in, $m(\omega) = m_0\omega(m_1 + \omega)$, will yield the diffusion coefficient.

The value of the transport peak at $\omega \to 0$ is decidedly between the upper and lower bounds set by the constant and quadratic default models. The mass peak positions of each spectral function presented in Sections 3.3 and 3.4 alluded to an uncertainty in our results. The same uncertainty will be prevalent in the low frequency range. Although we cannot predict a precise value for the transport peak, it is encouraging to see that it falls between the values given by the other two default models.

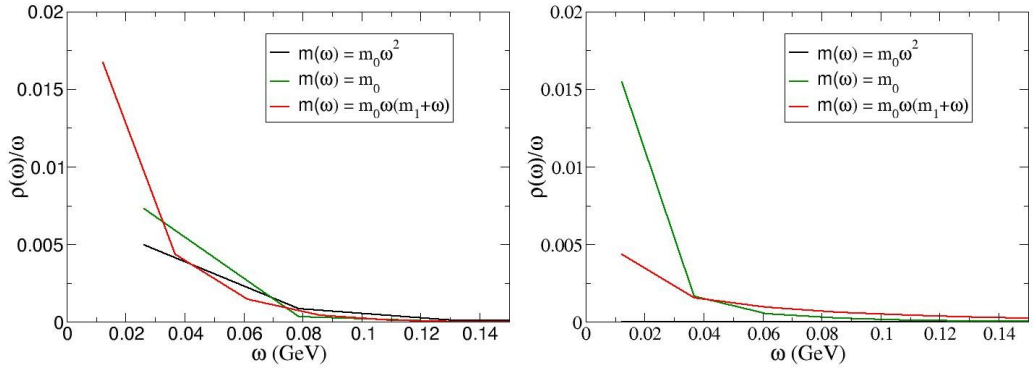

Figure 3.12: Low frequency region of spectral function from the $T/T_c = 1.05$ at momentum $p = 0.66$. The longitudinal polarisation is to the left and the transverse to the right.

Figure 3.12 shows the low frequency zone for the longitudinal (left) and transverse (right) polarisations of the vector current correlator with momentum $p = 0.66$ GeV and temperature $T/T_c = 1.05$. The transverse polarisation is as expected where the default models given in equations (3.15), (3.16) provide upper and lower bounds on the transport peak and the remaining $m(\omega)$ falls between them. However, the longitudinal component gives a different picture. The transport peak appears to diverge to infinity and $m(\omega) = m_0\omega^2$ does not converge to zero. As seen in Section 3.4 the longitudinal polarisation is not well behaved. We therefore cannot make any reasonable assumptions about the upper and lower bounds of the transport peak at finite momentum.

A direct comparison of these spectral functions to the default models in the absence of data is difficult as the scale of their respective intercepts is very different. Figure 3.13 shows the graphs of the default models. The constant default model diverges much more quickly than the spectral function of the transverse polarisation as $\omega \to 0$. This suggests that the data has some influence on the peak position. The green curves representing $m(\omega) = m_0\omega(m_1 + \omega)$ in Figures 3.12, 3.13 have a similar shape but a different intercept value. Again, this may indicate a contribution from the data in the transport peak.

The form of the transport peak at finite momentum is the same as in the zero momentum case, where the spectral function has a non-zero intercept with the vertical axis. In their studies of finite momentum spectral functions using the Langevin equations, Petreczky and Teaney found that the transport has a stable peak structure shifted slightly away from $\omega = 0$ [107]. We are uncertain as to why our results are in conflict with their findings. The momentum values we used are larger and this may be a consideration. Our momenta may not be small enough to yield an accurate representation of this peak. The finite resolution in ω may also cause some difficulties in reconstructing the transport peak. It is also possible that the MEM was unable to correctly reproduce the transport peak at finite momentum due to systematic errors.

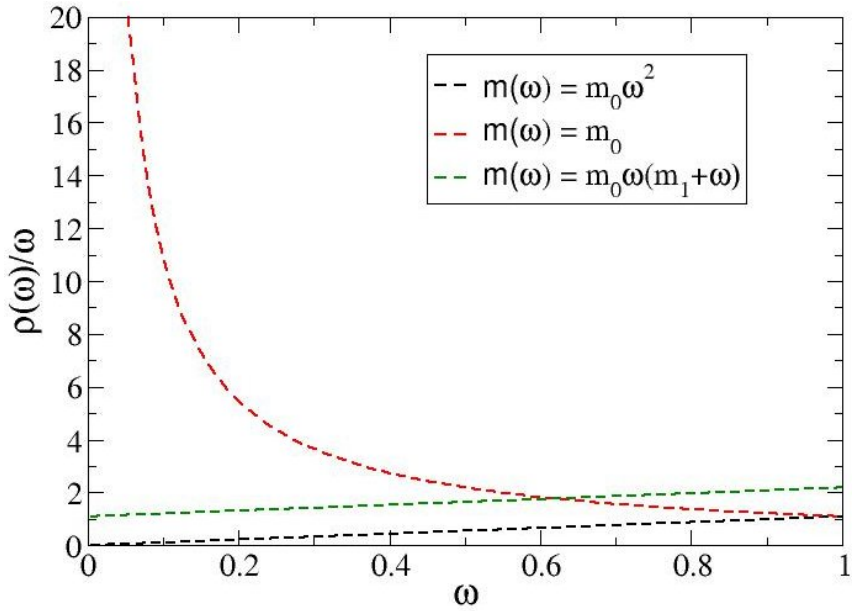

Figure 3.13: Low frequency region of the default models in the absence of data.

3.6 Conclusions and Outlook

I obtained spectral functions for the J/ψ meson from the conserved vector current on a set of highly anisotropic lattices. At zero momentum, the results indicate that the J/ψ particle melts in the QGP within a temperature range of $1.2 - 1.4T_c$. We consider the results to be accurate within this temperature range, suggesting that the J/ψ meson survives beyond the critical temperature for deconfinement. The results are less stable for higher temperatures due to the systematic uncertainties in the MEM process. It is possible that J/ψ survives beyond $1.4T_c$. Further analysis of the higher temperatures is required. However, this may not be possible with this generation of lattices.

I conducted a study of J/ψ at non-zero momentum but it is yet unclear if the melting of the J/ψ is dependent upon its momentum as the data are dominated by systematic errors. The transverse polarisation of the vector current correlator was found to be better behaved than the longitudinal component. The J/ψ meson appears to survive in the medium at non-zero momentum within the same temperature range of $1.2 - 1.4T_c$. Again, further analysis of the higher temperatures is required to draw meaningful conclusions.

Focusing on the low frequency region of the spectral functions, I obtained a transport peak from which we may calculate the heavy quark diffusion coefficient using the Green-Kubo formula in equation (3.3). An approximate range for the height of the transport peak has been found for J/ψ with zero momentum and for the transverse component of the current with finite momentum. This can provide a preliminary range for the value of the diffusion coefficient. However, the quark number susceptibility must first be calculated as it provides an overall normalisation scale. This is left for future work.

The results from this particular set of data are not completely reliable. Calculations from more accurate spectral reconstructions are required to complete this project. A new generation of lattices is currently in production (see Chapter 5) in the FASTSUM collaboration. This generation aims to increase the anisotropy to $\xi = a_s/a_\tau = 7$ with $a_s \simeq 0.125$ fm and will allow for smaller statistical uncertainties in the correlators. There have also been advances in the implementation of MEM. The use of Fourier basis vectors in the calculation of $\rho(\omega)$ can improve the accuracy of the results (See Section 2.4.3). Combining this amendment to the MEM procedure with the new correlation functions should yield spectral functions with smaller statistical and systematic uncertainties. It may then be possible to construct a transport peak with a more reliable height and thus compute a good approximation for the heavy quark diffusion coefficient.

Chapter 4

A Study of Open Charm Mesons

4.1 Motivation

Suppression of high transverse momentum hadrons is one of the principal signatures for the formation of the quark-gluon plasma. Jet quenching for light mesons in heavy ion collisions can be explained by radiative energy losses [116]. However, early RHIC measurements observed a suppression of non-photonic electrons for heavy mesons at high p_T, indicating a substantial heavy quark energy loss [117] which radiative energy loss alone could not sufficiently describe [118]. Considering corrections from collisional energy loss accounted for this discrepancy [20]. Since the electrons are predominately produced in the decays of D and B mesons, it was predicted that these heavy mesons would be formed and subsequently dissociate in-medium [25]. The time scale at which this diffusion occurs is comparable to the lifetime of the fireball in the URHICs. Thus the heavy quark spectrum contains information about the modifications imposed by the medium. In order to gain a theoretical understanding of this process, we must consider the spectral functions of the D mesons. In general, theoretical models of the D mesons' behaviour in the QGP are challenged by simultaneously considering the elliptic flow and the nuclear modification factor R_{AA}. However, it has been shown that comparing the D meson's elliptic flow and R_{AA} to that of the D_s meson can provide valuable insight into the recombination of hadrons in medium and the transport properties of the hadronic phase [119].

Experimentally, it can be difficult to extract information about the D mesons from their leptonic decay products. The kinematics for charm hadrons and electrons are only weakly correlated and the electrons measured in the yield contain contributions from a number of D and B decays. Measuring the charm hadrons from their hadronic decays leads to a better understanding of the properties of the medium [120]. Recent measurements by the ALICE Collaboration of the nuclear modification factor R_{pPb} for D mesons in proton-

lead collisions at the LHC found that the strong suppression of heavy quarks they observed is not due to cold nuclear matter effects, but to the strong coupling of the charm quarks to the QGP medium [121, 122].

D mesons can also be used to probe chiral symmetry restoration at finite density. Modifications to the chiral condensate are directly related to a mass shift in the D meson at high densities [123, 124, 125]. In a hot pion medium, D meson modifications were found to strongly influence J/ψ production during the expansion of the fireball in URHICs [126].

Previous lattice studies of D mesons can be found in references [68, 127, 128]. They employed the use of cumulants and spatial correlators to determine the survival of open charm bound states in the QGP. I present an analysis of the spectral functions of the S-wave D and D_s mesons at finite temperature. I also show the correlators and effective masses for these particles. This work has been presented at a conference and the proceedings can be found in reference [129]. For completeness, S-wave charmonium results from the same set of gauge configurations and a preliminary study of the charmonium P-waves have been included.

4.2 Formulation

I have computed charmonium and D meson correlators on FASTSUM's second generation of lattices. This ensemble employs $2+1$ flavours of dynamical quarks where the light quark masses are degenerate and a strange quark is included in the medium. The light quarks correspond to a pion mass of $m_\pi \simeq 380$ MeV and the strange quark mass is tuned to its physical value so that $a_\tau m_s = -0.0743$. A full set of lattice parameters is given in Table 4.1.

Param	Gen 2
N_f	$2+1$
a_s (fm)	0.1227
a_τ (fm)	0.03506
a_τ^{-1} (GeV)	5.63
ξ	3.5
T_c (MeV)	185
m_π/m_ρ	0.446

Table 4.1: Lattice parameters for the second generation of lattices.

This set of ensembles employs a Symanzik-Improved gauge action with tree-level tadpole coefficients as seen in equation (1.31). The fermion action is the anisotropic clover action with tree-level tadpole coefficients and stout-link

smearing given in equation(1.32). The clover action requires a choice of clover coefficients c_s and c_t. We follow the Hadron Spectrum Collaboration in their choice and set them to be

$$c_s = \frac{\nu}{\tilde{u}_s^3} \qquad \text{and} \qquad c_t = \frac{1}{2}\left(\nu + \frac{1}{\xi}\right)\frac{1}{\tilde{u}_s^2 \tilde{u}_t}, \tag{4.1}$$

where $\nu = \gamma_g/\gamma_f$ is the ratio of the bare gauge anisotropy to the bare fermion anisotropy, ξ is the desired renormalised anisotropy, and $\tilde{u}_s$ and $\tilde{u}_t$ are the smeared spatial and temporal mean links.

The charm quark action is the same as for the light and strange quarks with a minor adjustment in the bare fermion anisotropy. This was tuned separately by the Hadron Spectrum Collaboration [130]. The dispersion relation

$$(a_\tau E_{\eta_c})^2 = (a_\tau m_{\eta_c})^2 + \left(\frac{1}{\xi_{\eta_c}}\right)^2 (a_s p)^2 \tag{4.2}$$

determine was calculated for the η_c meson with the same parameters as the dynamical quarks ($\gamma_f = \gamma_l = 3.4$), resulting in a slight deviation from the pion dispersion relation. The fermion anisotropy was tuned to $\gamma_f = 3.988$, yielding the desired $\xi_{\eta_c} = 3.5$.

The critical temperature for deconfinement is determined from the renormalised Polyakov loop using the renormalisation prescription in [131]. The Polyakov loop $\langle L \rangle$ is related to the free energy F_q of a static quark via

$$L = \mathrm{e}^{-F_q(T)/T}. \tag{4.3}$$

The free energy has an additive renormalisation which provides a multiplicative renormalisation for the Polyakov loop. The renormalised Polyakov loop at $T = 355$MeV is set to be equal to 1 such that the free energy is zero at this temperature. For any temperature, it is then possible to calculate the renormalised Polyakov loop from the bare Polyakov loop [132]. The critical temperature for this set of lattices was calculated to be $T_c = 185$MeV. The lattice volumes and corresponding temperatures for the second generation are given in Table 4.2.

4.3 Correlator Analysis

As we have seen in Section 2.1, the imaginary time correlation function is the basic tool to study propagation of a particle on the lattice. The finite temperature correlators for the $D = \bar{l}c$ meson are presented on a logarithmic scale in Figure 4.1. The pseudoscalar D is shown in the left panel and the vector D^* is on the right. The correlators were computed using point-to-point

$N_s \times N_\tau$	T (MeV)	T/T_c	N_{cfg}
$24^3 \times 16$	352	1.9	1001
20	282	1.52	567
24	235	1.27	1002
28	201	1.09	1001
32	176	0.95	1000
36	156	0.84	501
40	141	0.76	502
$16^3 \times 128$	44	0.24	499

Table 4.2: Lattice size, temperature and number of configurations for the 2nd generation of lattices.

propagators as defined in equation (2.1).

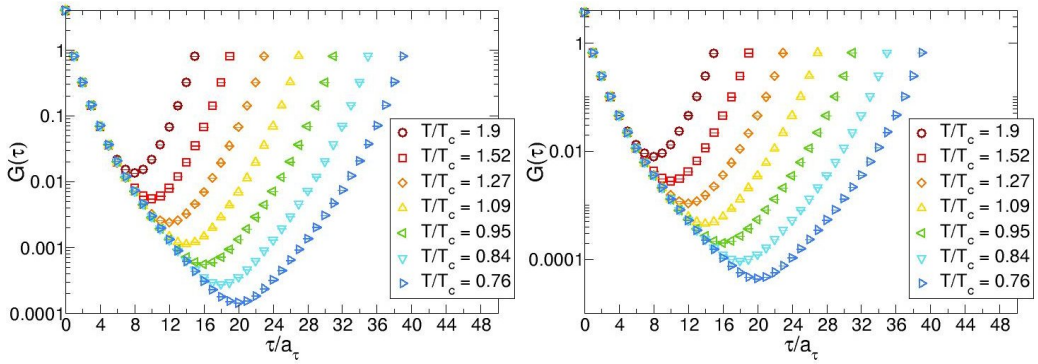

Figure 4.1: Correlator plots for the D meson in the pseudoscalar (left) and vector (right) channels.

Figure 4.2 shows the correlators for the $D_s = \bar{s}c$ meson. As before, the pseudoscalar D_s meson is presented on the left, and the vector D_s^* is on the right.

It is difficult to discern any physical results by looking at the correlators in this form. A better picture is provided by the effective mass of the mesons and by reconstructing the correlators using a reference temperature and comparing these reconstructions to the original correlator data.

4.3.1 Effective Masses

The correlation functions of a hadron may be used to calculate its effective mass. This is the mass of the particle according to the lattice parameters in use. As it is a lattice calculation, we define it in lattice units as follows.

$$a_\tau m_\tau = \ln\left(\frac{G(\tau)}{G(\tau + a_\tau)}\right) \tag{4.4}$$

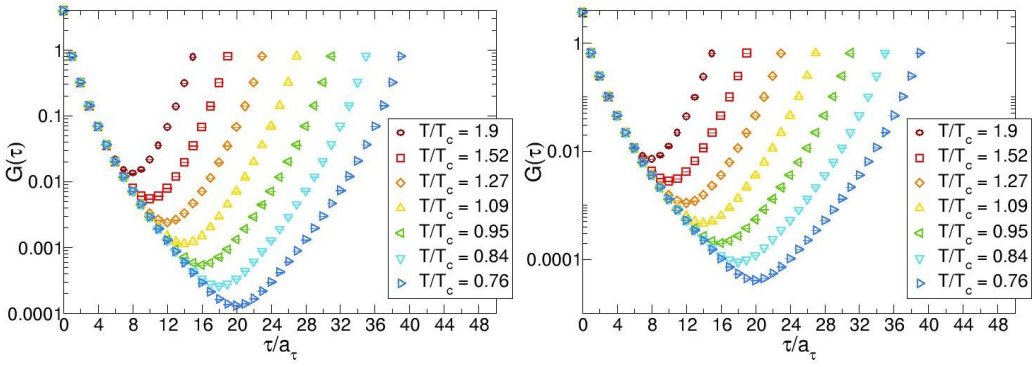

Figure 4.2: Correlator plots for the D_s meson in the pseudoscalar (left) and vector (right) channels.

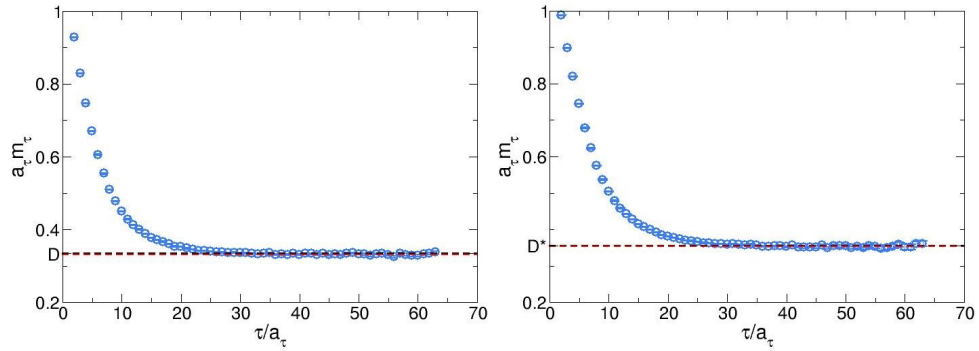

Figure 4.3: Effective mass plots for the D meson in the pseudoscalar channel (left) and the vector channel (right) at zero temperature. The black dashed horizontal lines represent the calculated masses, and the red represent the physical masses.

For small time separations τ, contributions from excited states are present in the effective mass. These give way to a plateau at the ground state mass at higher τ.

I have calculated the effective masses for the D meson at the lowest available temperature, $T = 0.24T_c = 44$ MeV and they are shown in Figure 4.3. The pseudoscalar meson is shown in the left panel, and the vector on the right. The black dashed horizontal lines represent the values of the ground state masses as determined by Moir et al in [133] and the red are the physical masses. Variational analysis was used to calculate these masses and the values obtained for the light quarks are larger than their physical masses. Hence, the D meson mass is also larger than its physical value. A clear plateau can be seen in each plot where my calculations correctly reproduce the masses.

A similar case is presented for my work on the D_s meson at $T = 0.24T_c = 44$ MeV in Figure 4.4. Again, the pseudoscalar is presented on the left and the vector on the right. A stable plateau is achieved at the expected value for D_s in each channel.

I have also calculated the effective masses for the pseudoscalar and vector D mesons at finite temperature, and these are presented in Figure 4.5. The

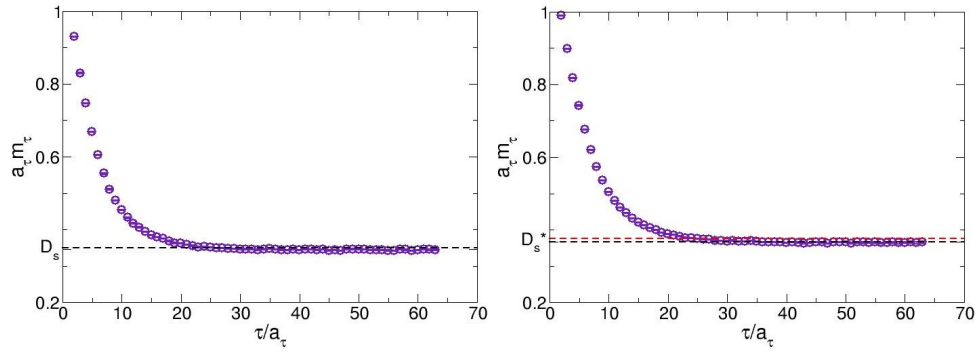

Figure 4.4: Effective mass plots for the D_s meson in the pseudoscalar channel (left) and the vector channel (right) at zero temperature. The black dashed horizontal lines represent the calculated masses, and the red represent the physical masses.

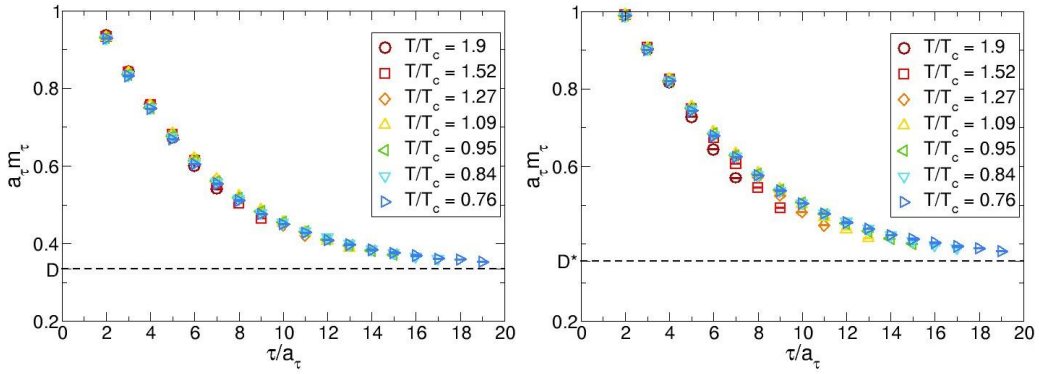

Figure 4.5: Effective mass plots for the D meson in the pseudoscalar (left) and vector (right) channels. The dashed horizontal lines represent the calculated masses.

D meson is expected to survive in the medium until temperatures reach $\sim T_c$ [127, 68]. A plateau is therefore expected at the mass value for temperatures below T_c. This expectation is not fulfilled for either the pseudoscalar or the vector. However, we cannot draw conclusions about the melting of either particle from the effective mass alone. In Figure 4.3 we notice that the plateau is not attained until $\sim \tau/a_\tau = 25$. Thus it is unlikely that the number of data points is sufficient in any high temperature calculation. The $24^3 \times 40$ lattice is our coldest (non-zero temperature) lattice, which provides 20 temporal data points due to the symmetry of the correlators. Nonetheless, there is a clear trend towards the calculated mass value visible in both D and D^*. There are temperature dependent deviations at a number of timeslices in both channels, particularly the vector. This may be due to the zero modes present in the vector channel. Further analysis of the transport coefficients could shed some light on this effect.

Turning now to the D_s and D_s^*, we see a very similar picture. The high temperature effective masses are trending towards a plateau. Again, in the zero temperature results, the plateau is achieved at $\sim \tau/a_\tau = 25$ (see Figure

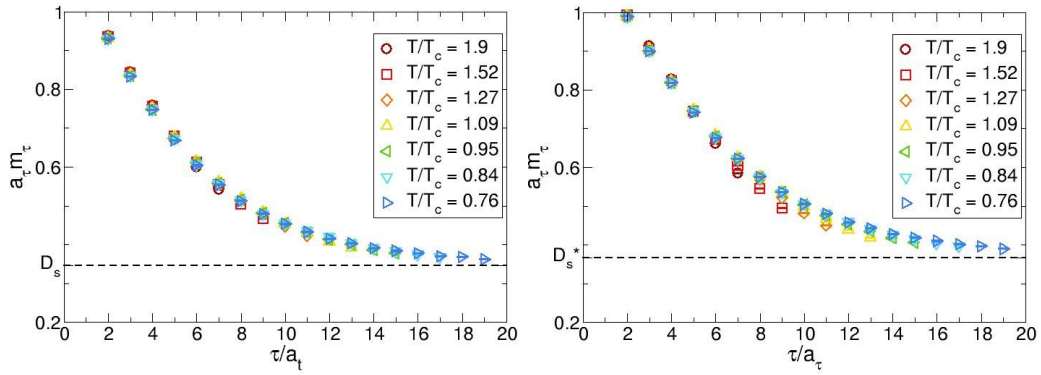

Figure 4.6: Effective mass plots for the D_s meson in the pseudoscalar (left) and vector (right) channels. The dashed horizontal lines represent the calculated masses.

4.4). We can again ascertain that the number of data points is insufficient to draw conclusions about the exact mass of the particles at high temperature. As with the D meson, there are small deviations at certain timeslices visible. Again, we cannot be certain from the effective mass alone if they are an effect of the medium or of the correlator itself.

4.3.2 Reconstructed Correlators

Thermal effects of the medium can impact the correlators and subsequently, the spectral functions. In order to distinguish these effects from the trivial temperature dependence of the kernel $K(\omega, \tau, T)$, the correlator can be compared to a reconstructed correlator at a given temperature [134]. The reconstructed correlator is defined as

$$G_{\mathrm{rec}}(\tau, T; T') = \int_0^\infty \mathrm{d}\omega\ \rho(\omega; T') K(\omega, \tau, T), \tag{4.5}$$

where T' is a reference temperature at which the spectral function can be reliably constructed. Since the temperature is inversely proportional to the number of temporal data points, $T \propto 1/N_\tau$, the coldest lattices yield the most accurate results. As such, T' is usually taken to be the lowest temperature in the data set.

The ratio of the measured correlator to the reconstructed correlator $G(\tau, T)/G_{\mathrm{rec}}(\tau, T; T')$ is considered in order to gain insight into the temperature dependence of the spectral function. Without any in-medium modifications, this ratio is expected to be unity. It is possible to reconstruct the correlator without first computing the spectral function at the reference temperature T' [106]. From the definition of the finite temperature kernel and using the fact

that $N_\tau = 1/T$ we have that

$$K(\omega, \tau, T) \equiv \frac{\cosh[\omega(\tau - 1/2T)]}{\sinh(\omega/2T)} = \frac{\cosh[\tilde{\omega}(\tilde{\tau} - N_\tau/2)]}{\sinh(\tilde{\omega}N_\tau/2)}, \tag{4.6}$$

where $\tilde{\omega} = a_\tau\omega$ and $\tilde{\tau} = \tau/a_\tau$ are in lattice units. Applying the following relation

$$\frac{\cosh[\tilde{\omega}(\tilde{\tau} - N_\tau/2)]}{\sinh(\tilde{\omega}N_\tau/2)} = \sum_{n=0}^{m-1} \frac{\cosh[\tilde{\omega}(\tilde{\tau} + nN_\tau - mN_\tau/2)]}{\sinh(\tilde{\omega}mN_\tau/2)}, \tag{4.7}$$

where

$$m = \frac{N'_\tau}{N_\tau} \in \mathbb{Z}, \tag{4.8}$$

for $T = 1/N_\tau$ and $T' = 1/N'_\tau$, we obtain a formula for the reconstructed correlator,

$$G_{\text{rec}}(\tilde{\tau}, T; T') = \sum_{n=0}^{m-1} G(\tilde{\tau} + nN_\tau, T'). \tag{4.9}$$

To ensure $m \in \mathbb{Z}$, some additional zeros were introduced in the middle of $G(\tau, T')$ where necessary. As this method does not rely on the reconstruction of the spectral function, it is clear that any deviation from $G/G_{\text{rec}} = 1$ indicates thermal effects of the QGP. In this work I chose the lowest temperature $T' = 0.24T_c = 44$ MeV to be the reference temperature.

The results for the D meson are presented in Figure 4.7. At the lowest temperature $T/T_c = 0.76$ they are consistent with $G/G_{\text{rec}} = 1$, indicating no medium effects at this temperature in both the pseudoscalar and the vector channels. There are significant thermal modifications visible at temperatures above T_c, indicating a strong thermal effect from the QGP. Interestingly, at $T/T_c = 0.84$ a significant deviation from unity is also apparent, suggesting that there are thermal modifications below T_c.

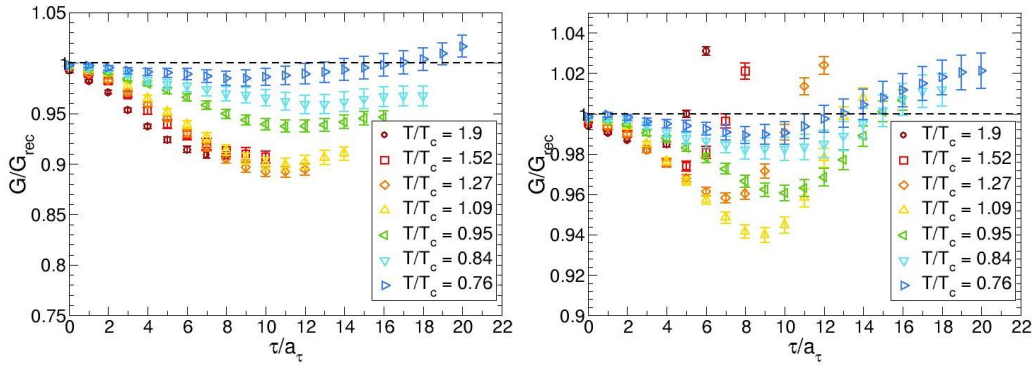

Figure 4.7: Ratio of correlator to reconstructed correlator for the D meson using a reference temperature of $T = 44$ MeV in the pseudoscalar (left) and vector (right) channels.

A very similar picture is evident in the D_s meson results, which are pre-

sented in Figure 4.8. In both the pseudoscalar and vector channels, the lowest temperature indicates no modifications. At high temperature and in particular at $T/T_c = 0.84$ we again see a deviation from $G/G_{\text{rec}} = 1$, indicating thermal modifications in the QGP, but also in the hadronic phase. With the exception of the highest temperature $T/T_c = 1.9$, the modifications in the D_s sector are smaller than D sector, supporting the prediction of an increased D_s yield relative to D in heavy ion collisions [119, 135].

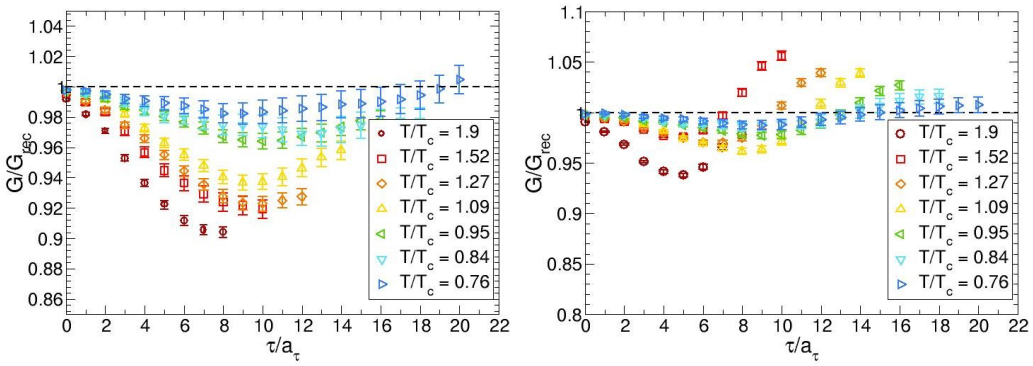

Figure 4.8: Ratio of correlator to reconstructed correlator for the D_s meson using a reference temperature of $T = 44$ MeV in the pseudoscalar (left) and vector (right) channels.

From these results we may deduce that the temperature of the medium plays an important role in the lifespan of the D and D_s mesons. There is a clear contribution from thermal effects of the QGP. In order to understand this contribution, we must consider the finite temperature spectral functions for these particles, which are presented in Section 4.5.

4.4 Spectral Functions at Zero Temperature

Spectral functions for the D and D_s mesons have been computed in the pseudoscalar and vector channels using Bryan's algorithm in the MEM process with the modified kernel in equation (2.31) and the Fourier basis vectors discussed in Section 2.4.3. I employed the use of two of the default model functions we saw in the last chapter

$$m(\omega) = m_0, \tag{4.10}$$

$$m(\omega) = m_0\omega(m_1 + \omega). \tag{4.11}$$

At large ω, $m(\omega) = m_0 w^2$ is consistent with the default model in equation (4.11). Details of these functions can be found in Section 3.3. As there is no transport peak to consider, the parameter m_1 does not play an important role. We have shown in Section 3.3 that it is influential only for $\omega \to 0$. For this

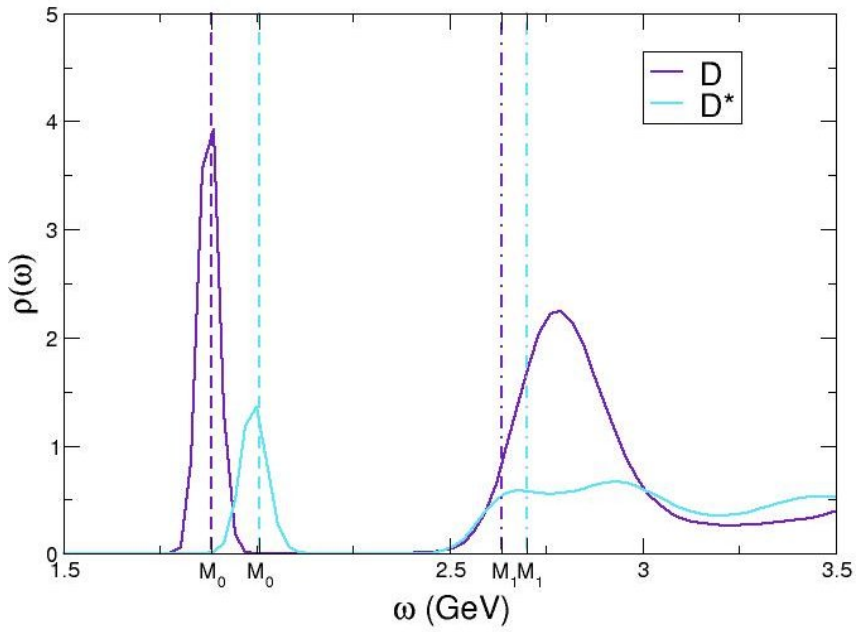

Figure 4.9: Spectral functions for the D and D^* mesons at zero temperature. The dashed vertical lines represent the ground state M_0 and first excited state M_1 as calculated by [133].

work, I set $m_1 = 1$. I present the results for the D, D^*, D_s, and D_s^* mesons at zero temperature.

Figure 4.9 shows the spectral functions for the D meson in the pseudoscalar and vector channels. I have included dashed vertical lines to indicate the masses of the ground state M_0 and the first excited state M_1 from [133]. A stable peak structure at the ground state masses for each of the D and D^* mesons is evident. The respective heights of the peaks are very different, but since the correlators have not been normalised we can attach no physical significance to this.

While the spectral function rises to another peak in the vicinity of the first excited state for the pseudoscalar D meson, we cannot say with any certainty that the MEM has correctly reproduced it. The peak sits at a much higher value than the calculated first excited state and is quite broad. It likely contains contributions from a number of higher excited states and is subject to finite volume effects. The vector D^* does not achieve a stable peak at its first excited state. The spectral function rises in a very broad structure but the MEM fails to reproduce a reliable reconstruction of this state. Lattice artifacts and the systematic errors involved in MEM dominate in this region and we cannot conclusively say that we see evidence of the first excited state for either particle.

The spectral functions for the D_s meson are presented in Figure 4.10. We can see the spectral function again produces a stable peak at the calculated ground state of both the D_s and D_s^* mesons. The first excited state has no

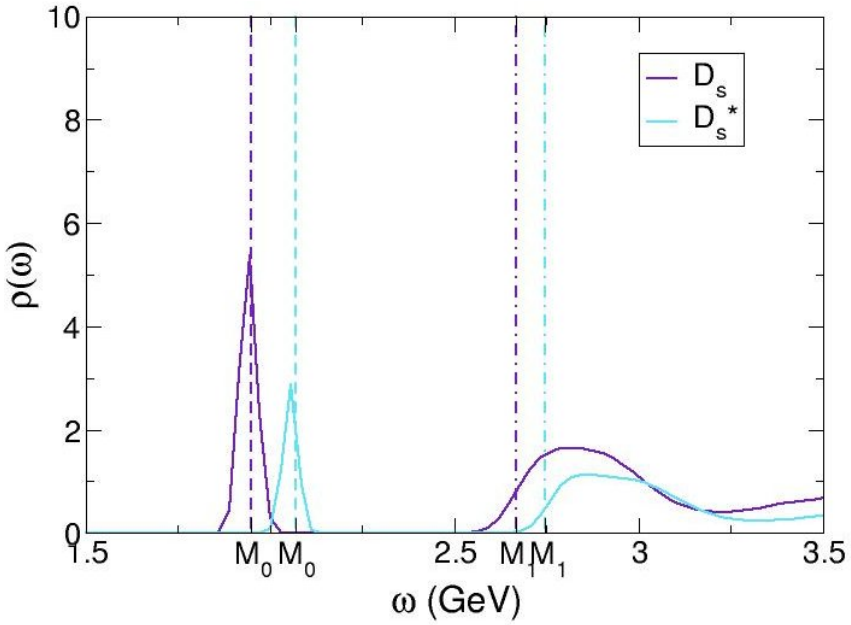

Figure 4.10: Spectral functions for the D_s and D_s^* mesons at zero temperature. The dashed vertical lines represent the ground state M_0 and first excited state M_1 as calculated by [133].

clearly defined feature for either the pseudoscalar or vector particles. The MEM appears to form another peak structure around this value but it has a large width. We cannot with any certainty identify the first excited states. This can be attributed to lattice artifacts and limited statistics in this region.

I tested the dependence of MEM on the number of data points available. An unconvincing ground state peak is visible in Figure 4.11 when the number of temporal data points is significantly reduced. Reducing the number of timeslices available from 126 to 15 has a big impact on the construction of the spectral function. The data is not correctly reproduced and even the ground state has not been pinpointed.

It seems that a small number of temporal data points on the lattice presents a big problem for the MEM reconstruction. This unfortunately means that for the high temperature data the MEM may not be correctly reproducing their spectral functions. This may also be due to the statistical errors in the correlator data. I used the spectral functions to reconstruct the correlator data and as can be seen in Figure 4.12 they are not all consistent. At finite temperature the reconstructed correlators appear to be the same as the original correlators, within errors. However, these errors are larger than expected and thus the results may not be trustworthy. It gives a very different picture than the reconstructions in Figure 4.7 which did not rely on $\rho(\omega)$. The zero temperature reconstruction deviates significantly from the original data which is a cause for concern. The large deviations may be related to the resolution of the spectral functions. An investigation into these errors is underway and we

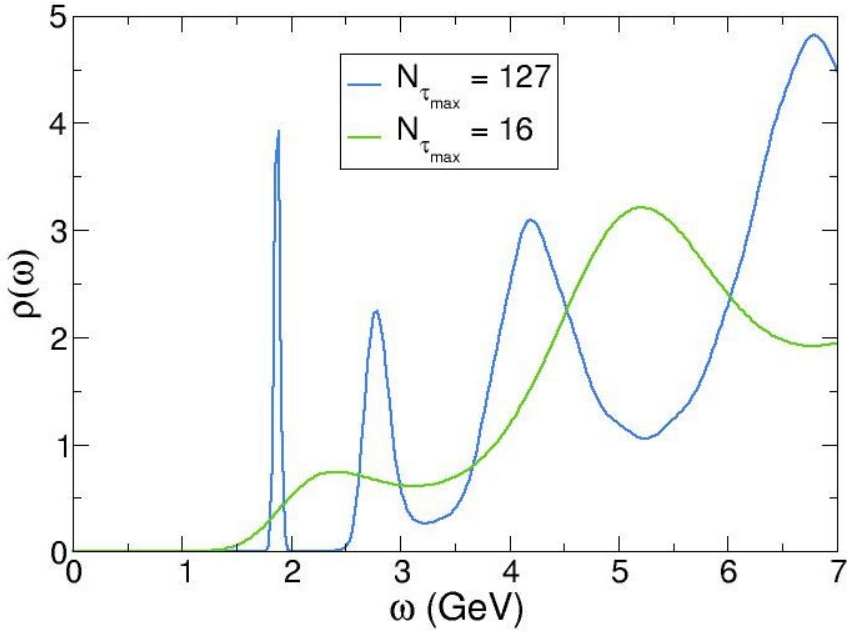

Figure 4.11: Effect of varying the number of timeslices used for the zero temperature pseudoscalar D meson.

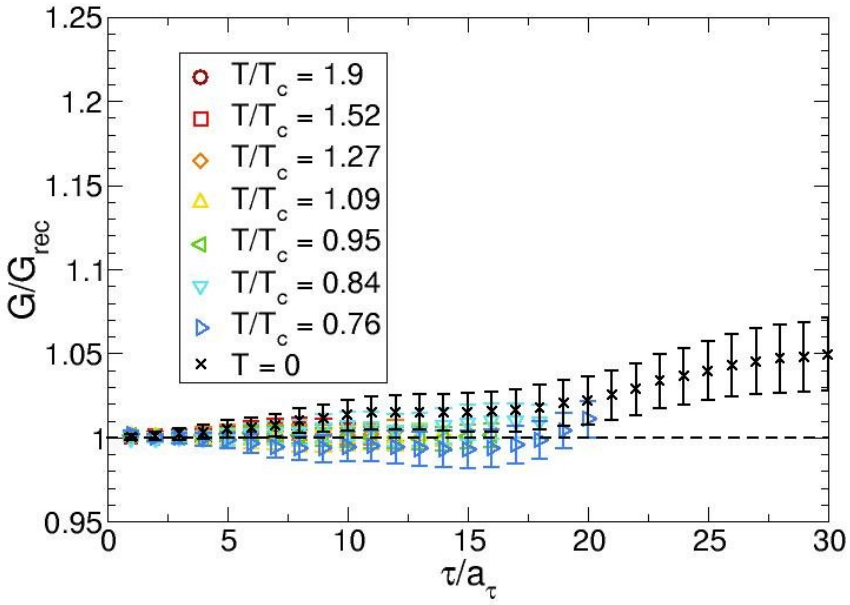

Figure 4.12: Ratio of the original correlator to the correlator reconstructed from the spectral functions for the pseudoscalar D meson.

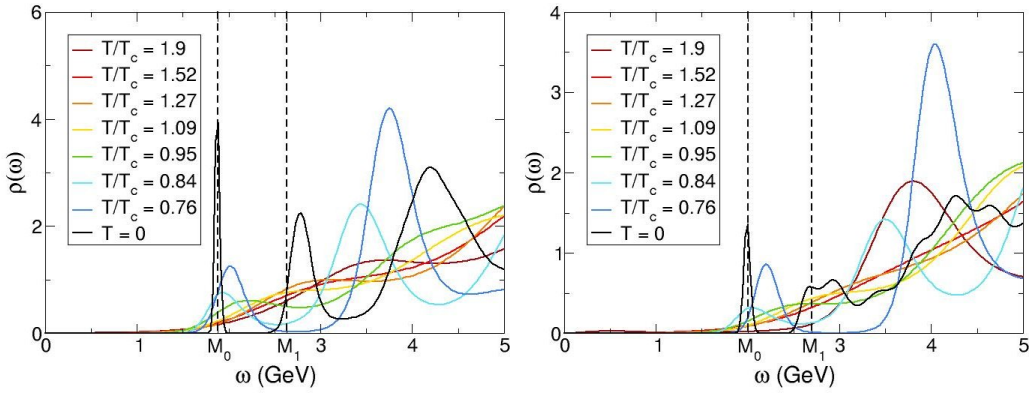

Figure 4.13: Spectral functions for the D meson in the pseudoscalar (left) and vector (right) channels. The dashed vertical lines represent the ground state M_0 and first excited state M_1 as calculated by [133].

are currently producing correlators with more point sources which may improve their accuracy.

4.5 Spectral Functions at Finite Temperature

In this section I present the spectral functions for the D, D^*, D_s, D_s^* mesons at finite temperature. I present the results at zero temperature along with those of higher temperatures for a more complete picture.

First, consider the D meson spectral functions which are presented in Figure 4.13. The pseudoscalar D meson is in the left panel and the vector D^* is on the right. A well-defined peak structure is reproduced for $T/T_c = 0.76, 0.84$. This indicates that these particles survive up to the critical temperature. In the higher temperature lattices this peak loses its definition and we may conclude that the D and D^* mesons do not survive beyond T_c. The vector channel does not give a convincing peak even at $T/T_c = 0.84$, suggesting that the D^* meson melts below T_c.

Now we will turn to the D_s meson. As before, the lowest two temperatures give a well defined peak around the ground state mass in both the pseudoscalar and vector channels, as can be seen in Figure 4.14. Above these temperatures ($\sim T/T_c = 0.84$), in both cases, the particles do not appear to survive in the medium. The D_s^* meson appears to melt even sooner than the D_s meson. The peak structure at $T/T_c = 0.84$ is very broad. It appears as though the D_s meson melts at $\sim T_c$, which supports previous calculations using spatial correlation functions [68]. We may draw the conclusion that none of the D mesons survive at temperatures exceeding the critical temperature. However, the high temperature data are subject to uncertainties in the MEM.

I conducted a study of the systematic uncertainties in MEM using the D meson data. Figure 4.15 shows the variance of the spectral function under the

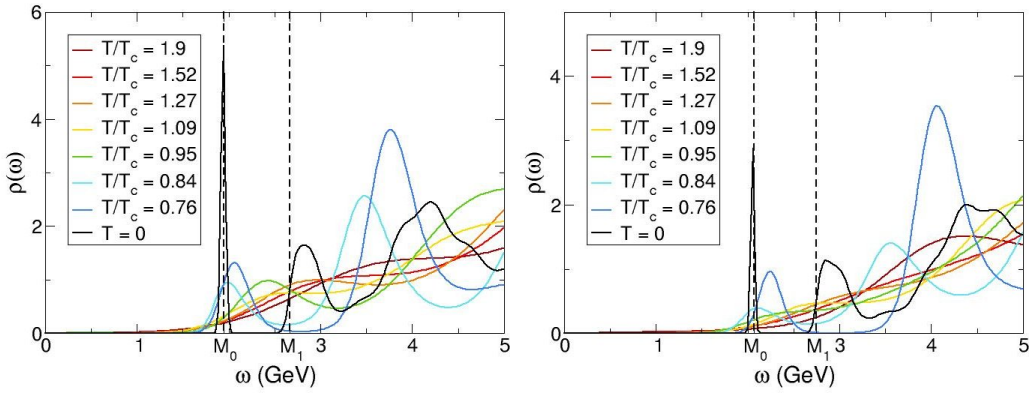

Figure 4.14: Spectral functions for the D_s meson in the pseudoscalar (left) and vector (right) channels. The dashed vertical lines represent the ground state M_0 and first excited state M_1 as calculated by [133].

change in the prior function $m(\omega)$ for the pseudoscalar D meson at temperature $T/T_c = 0.84$. A variation in the normalisation parameter m_0 with the quadratic default model is presented alongside the constant default model. The peak positions at the ground state mass are consistent and even the secondary peak structures visible at $\omega \sim 3.4$ GeV are similar. These secondary peaks are known to contain lattice artifacts and are not at the correct position for the first excited state. However, their agreement with one another is a promising indication that our results do not depend strongly on the default model.

I also tested the MEM using only half of the timeslices available on the $24^3 \times 36$ lattice. This is the blue line in Figure 4.15. It presents a much weaker structure than the other graphs, suggesting that the number of temporal data points is an important factor in the ability of MEM to reproduce a reliable spectral function. The spectral function rises in the region of the ground state mass but does not reproduce a stable peak. It indicates that MEM does not work well for $N_\tau \lesssim 20$.

An interesting effect has arisen in these results. There appears to be a thermal mass shift below T_c. The position of the ground state peak in the spectral functions at the lowest temperature $T/T_c = 0.76$ is higher than expected, and higher indeed than the mass given by the $T/T_c = 0.84$ peak. This can be seen in the pseudoscalar and vector channels for each of the D and D_s mesons. We have seen in Figure 4.15 that the spectral reconstruction at $T/T_c = 0.84$ has no dependence on the default model. In Figure 4.16 I present the spectral functions for the D meson at the lowest two temperatures calculated with our two different default models. These preliminary plots suggest that this feature is robust and does not arise from an abnormality in the method used to extract the spectral functions. Further study is required to fully understand the true nature of this thermal effect.

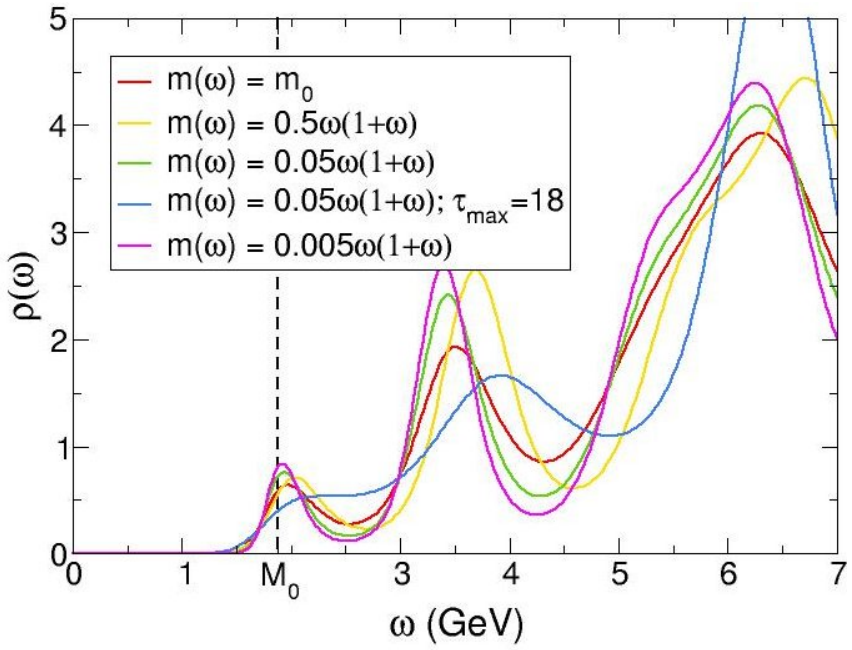

Figure 4.15: A study of default model dependence of the MEM process on the pseudoscalar D meson at temperature $T/T_c = 0.84$. The dashed vertical line represents its calculated mass.

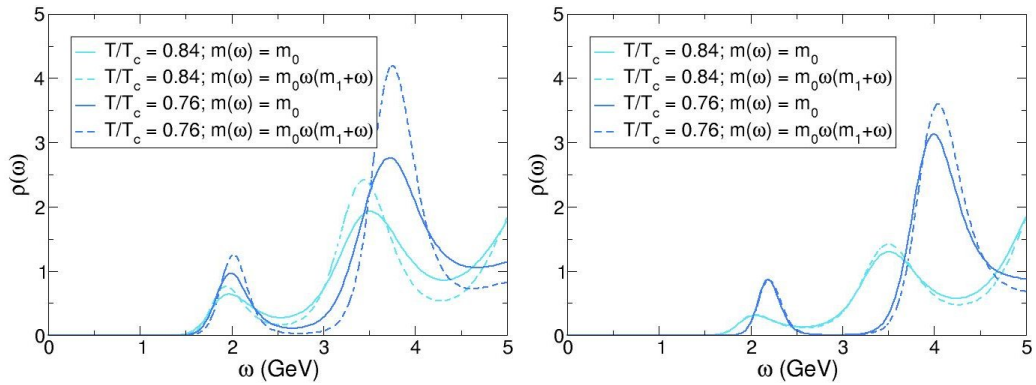

Figure 4.16: Spectral functions of the D meson in the pseudoscalar (left) and vector (right) channels at temperatures $T/T_c = 0.76, 0.84$ with two different default models.

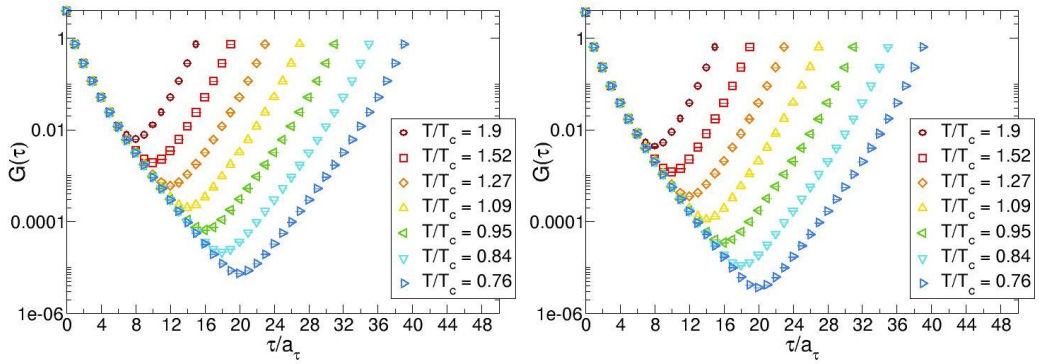

Figure 4.17: Correlator plots for η_c (left) and J/ψ (right) at finite temperature on a logarithmic scale.

4.6 Charmonium Results

The second generation of ensembles gave us access to temperatures below T_c. In the charmonium studies presented in the previous chapter, each temperature was above T_c. These lower temperatures can give more insight into the interactions of charmonium with the medium and provide more information on their behaviour as they cross the deconfinement threshold. Here I present results for the S-wave η_c and J/ψ and some preliminary work on P-wave charmonium.

4.6.1 Correlators and Effective Masses for S-Wave Charmonium

We begin with the correlators for the η_c and J/ψ mesons, presented in Figure 4.17 with the pseudoscalar on the left and the vector on the right. The correlators have the shape we expect at each temperature. However, the errors in these functions are approximately 3% which limits our ability to make precise determinations of their effective masses and spectral functions. I have computed the effective masses and they are presented in Figure 4.18 with the η_c on the left and J/ψ on the right. As we can see, a stable plateau is visible for both mesons at their respective masses as determined by Liu et al in [130]. It is clear that the number of temporal data points plays a significant role in the determination of spectral quantities. As with the D mesons, the plateau is only attained at $\tau/a_\tau \sim 25$.

A very similar picture emerges for charmonium at finite temperature as for the D mesons. The effective masses are presented in Figure 4.19. From the results presented in the previous chapter, J/ψ survives to temperatures $T \sim 1.4T_c$. The effective mass of the mesons below this temperature should be detectable in the form of a plateau. However, the small number of data points available for these temperatures limits their ability to achieve a plateau. For both η_c and J/ψ we see a trend towards the calculated mass of the mesons,

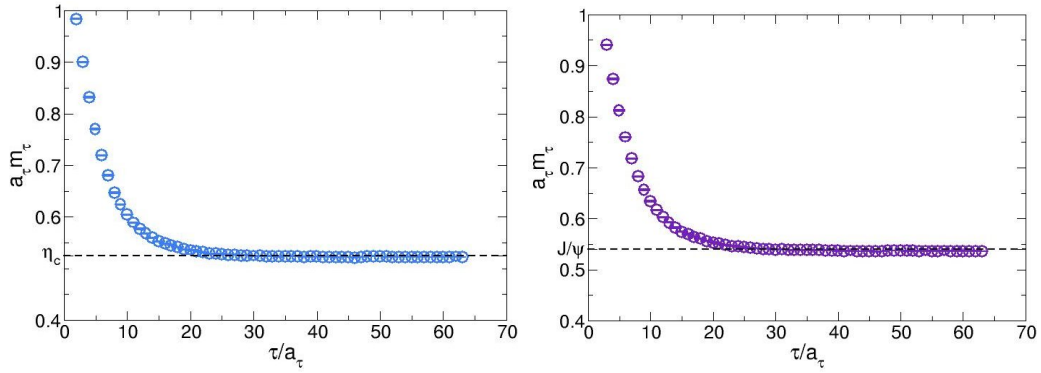

Figure 4.18: Effective mass plots for η_c (left) and J/ψ (right) at zero temperature. The dashed horizontal lines represented the calculated masses.

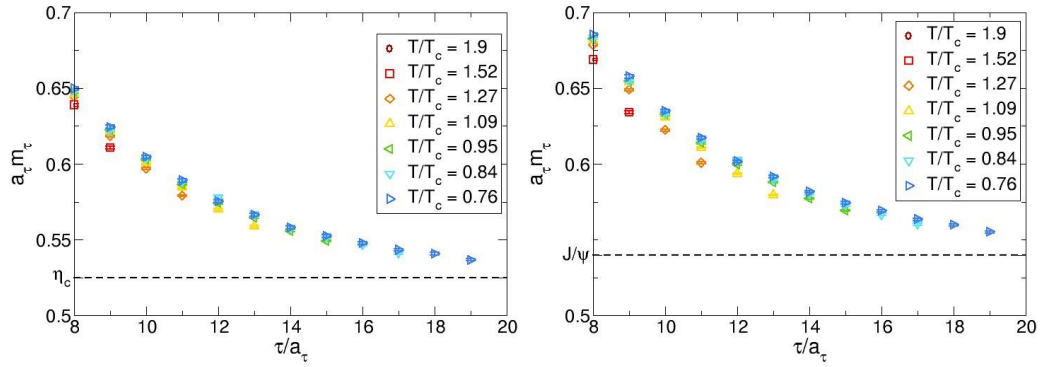

Figure 4.19: Effective mass plots for η_c (left) and J/ψ (right) at finite temperature. The dashed horizontal lines represented the calculated masses.

but even for $T < T_c$ a plateau is not attained.

The reconstructed correlators were calculated as per Section 4.3.2 using a reference temperature of $T' = 0.24T_c = 44$ MeV. The ratios of the original correlator data to their reconstructions are presented for the S-waves in Figure 4.20 with the η_c on the left and J/ψ on the right. For the η_c there is a significant thermal effect apparent in the correlators. As with the D mesons, it is unclear exactly what effect these medium modifications will have on the particle.

A similar situation is seen for the J/ψ vector meson. The effect is far

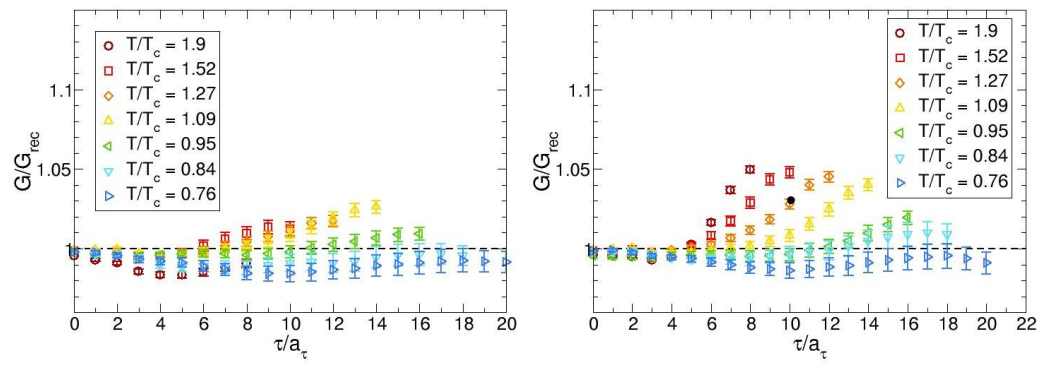

Figure 4.20: Ratio of correlator to reconstructed correlator for η_c (left) and J/ψ (right) at finite temperature.

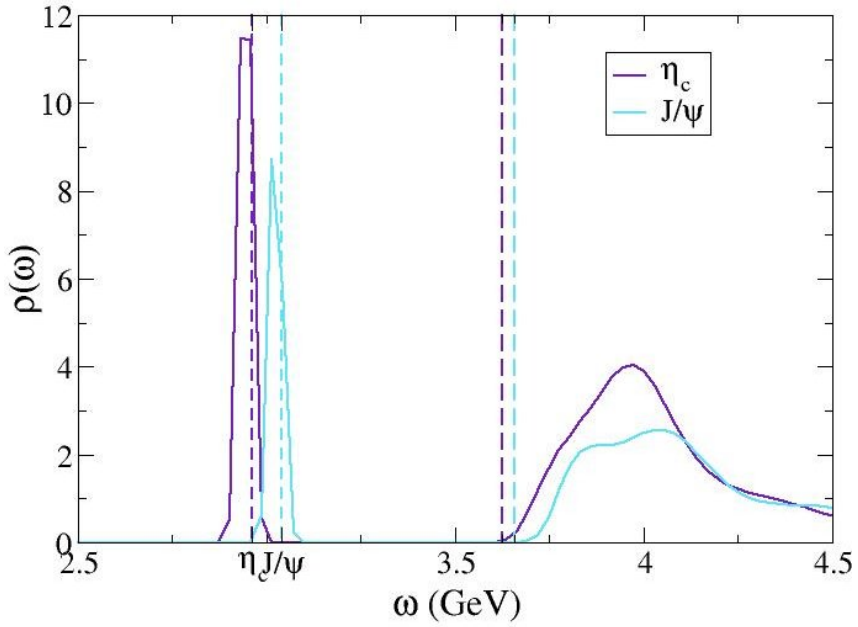

Figure 4.21: Spectral functions for the η_c and J/ψ mesons at zero temperature. The dashed vertical lines represent the ground state M_0 and first excited state M_1 as calculated by [130].

more pronounced at higher temperatures than in the pseudoscalar case. This suggests that the properties of the QGP heavily influence the movement of the J/ψ particle through it. This is consistent with the results of the last chapter. The survival of J/ψ in-medium allows for a transport peak to be detected in the spectral function at low frequency. A thermal effect was seen in the results from the first generation. An analysis of the transport peaks of high temperature vector charmonium in the second generation will provide insight into the characteristics of the QGP.

4.6.2 Spectral Functions for S-Wave Charmonium

We turn now to the spectral functions of S-wave charmonium. They are presented at zero temperature in Figure 4.21. The MEM procedure used to evaluate these functions is Bryan's method with the modified kernel and Fourier basis vectors as before. There is a sharp stable peak at the ground state masses for both the η_c and J/ψ mesons as calculated by Liu et al in [130]. The spectral function rises in a broad secondary peak for each meson. However, it is not at the correct position for the first excited state and likely includes contributions from higher excitations and lattice artifacts.

I also conducted a study of the spectral functions at finite temperature, which are presented in Figure 4.22 with the η_c meson on the left and the J/ψ meson on the right. The zero temperature results are included and the dashed vertical lines represent the ground state and first excited state energies. There is a peak structure evident at the ground state mass in the pseudoscalar at

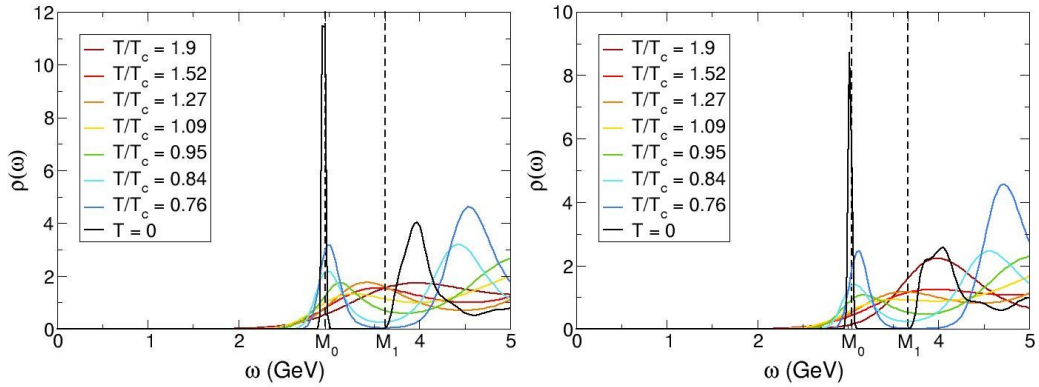

Figure 4.22: Spectral functions for η_c (left) and J/ψ (right) at finite temperature. The dashed vertical lines represent the ground state M_0 and first excited state M_1 as calculated by [130].

temperatures $T < T_c$. However, at $T/T_c = 0.95$ the peak is much broader and is shifted slightly from M_0. The η_c meson does not appear to survive beyond this point. However, the statistical uncertainties in the correlators and the systematic uncertainties in MEM may play a role in this. Previous analysis of these configurations with a different MEM code showed η_c melting at a temperature $T \sim 1.6T_c$ [136]. A similar picture is presented in the vector channel. The peak structure at $T/T_c = 0.95$ is even broader than it is in the pseudoscalar channel. We see no evidence of the survival of J/ψ at temperatures above T_c. This is in conflict with our results from Section 3.3 which showed a J/ψ dissociating at temperatures $T \sim 1.4T_c$. The systematic uncertainties may dominate in the high temperature data.

4.6.3 Reconstructed Correlators for P-Wave Charmonium

I have done preliminary work on the scalar χ_{c0} and axial vector χ_{c1} charmonium correlation functions. The correlator plots themselves do not give us much insight into the in-medium propagation of these mesons. We consider instead the ratio of the correlators to the reconstructed correlators, which can provide more information on the effect of the medium. They are presented in Figure 4.23 with the scalar on the left and the axial vector on the right. As with the D mesons and S-wave charmonium, the correlators were reconstructed with reference temperature $T' = 0.24T_c = 44$ MeV. There appears to be a very significant thermal effect present for both the scalar and the axial vector. The high temperature correlators show a dramatic difference in this ratio. This supports previous results using anisotropic lattices by Aarts et al in [112]. Since the signal-to-noise ratio is high for P-wave states and they have a known zero mode, we cannot say for certain how strong the thermal effect is. Similar results were found for the P-wave states by Ding et al [106].

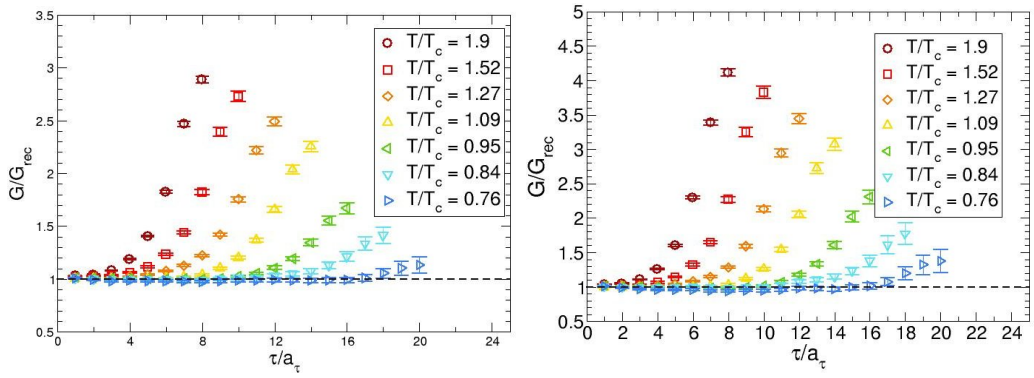

Figure 4.23: Ratio of correlator to reconstructed correlator for the scalar (left) and axial vector (right) at finite temperature.

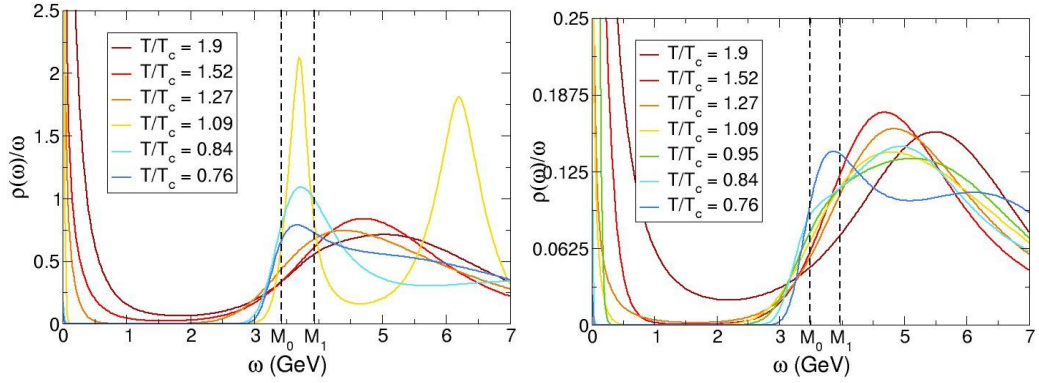

Figure 4.24: Spectral functions for scalar (left) and axial vector (right) at zero momentum. The dashed vertical lines represent the ground state M_0 and the first excited state M_1 as calculated by [130].

4.6.4 Spectral Functions for P-Wave Charmonium

The spectral functions at finite temperature are presented in Figure 4.24. The zero temperature results are work in progress and are therefore not shown here. In the scalar channel, there is a peak structure for temperatures below T_c, but no evidence of a peak above T_c. This indicates that χ_{c0} survives up to the critical temperature for deconfinement but perhaps not beyond it. Even at the lowest temperature $T/T_c = 0.76$, the peak is broad and is not centred on the calculated value for the ground state mass. Although there appears to be a well-defined peak at $T/T_c = 1.09$ the instability in the lower temperature spectra suggests that MEM is not correctly reproducing the ground state. Systematic uncertainties in MEM and a poor signal-to-noise ratio may dominate in these results. We are currently working to improve upon this.

The spectral function for χ_{c1} shows only a small peak at the lowest temperature. For temperatures $T/T_c \geq 0.84$ there is no evidence of a peak. Umeda et al found that the axial vector dissociates at temperatures $T \sim T_c$ [137]. This may indicate that the axial vector does not survive at these temperatures. Comparing these results to the spectral functions obtained in [112], I suggest

that the systematic uncertainties dominate over the data and with our current data, MEM cannot accurately reconstruct the spectral functions for P-wave charmonium.

4.7 Conclusions and Outlook

The first lattice results for S-wave open charm mesons from temporal correlation functions have been presented. In comparing reconstructions of the correlators to the original functions I have shown there are significant medium modifications for both the D and D_s mesons above and below T_c. I have also presented the spectral functions for these mesons at finite temperature. Neither the D nor the D_s appear to survive beyond the critical temperature for deconfinement. An apparent thermal mass shift was detected in the spectral functions at the lowest temperatures. The position of the ground state peak at $T/T_c = 0.84$ agrees with the $T/T_c = 0.24$ result. However, a slightly larger mass was measured at $T/T_c = 0.76$. This feature appears to be robust, though further analysis is required to determine its nature.

I have also presented results for S-wave and P-wave charmonium. A significant thermal effect is apparent from the ratio G/G_{rec} for both the S- and P-waves. In the spectral analysis of the S-waves with our current data, we see no evidence of survival above T_c for η_c or J/ψ. This is in conflict with my previous results in Chapter 3. The correlators for this generation of ensembles were calculated using point-to-all propagators. The first generation used all-to-all propagators and hence had much smaller statistical uncertainties. This may account for the discrepancy in the results. The statistical uncertainties in the correlator data for the second generation may prohibit an accurate reconstruction of the spectral functions. At present, we are producing additional correlators with extra point sources to improve the statistics of the data. In the near future, new spectral functions will be produced for these mesons.

My analysis of the P-wave spectral functions suggests that the scalar and axial vector dissociate at temperatures $T \sim T_c$. However, these spectral reconstructions may be dominated by statistical and systematic uncertainties. Further analysis of P-wave charmonium will be completed with the additional sources. We are currently also producing a new generation of highly anisotropic ensembles which may allow the spectral quantities of P-waves to become more accessible.

Chapter 5

A New Generation of Lattices

5.1 Motivation

For the results presented in this thesis thus far, I have used two generations of lattices to calculate the spectral functions of charmonium and D mesons. The defining parameters for each generation are quite different (see Tables 3.1, 4.1). Our aim is to create a new generation of lattices which doubles the anisotropy $\xi = a_s/a_\tau$ from the second generation by halving the temporal lattice spacing a_τ, keeping all other parameters constant. This allows us to double N_τ at constant temperature. As this is one of the main limiting factors for MEM, it will dramatically improve the ability of MEM to reconstruct the spectral functions for charmed mesons. It will also be possible to reach higher temperatures while reducing the $\mathcal{O}(a_\tau^2)$ errors.

With the improved resolution on these new ensembles, we hope to gain new insights, for example analysing some excited-state physics for the charmed mesons which we could not reliably discern from either of the previous two generations. The P-wave states should also become more accessible. In this chapter, I outline the process by which we are creating this new generation of ensembles.

5.2 Set Up

I followed a method previously established by Edwards et al [138] for tuning parameters for three flavour anisotropic clover fermions with stout link smearing. Using the lattice coupling β, the bare gauge anisotropy γ_g, the bare fermion anisotropy γ_f and the quark mass (in lattice units) $a_\tau m_0$ as input parameters I found results for the spatial lattice spacing a_s, the ratio of the pion mass to the rho mass m_π/m_ρ, the gauge anisotropy ξ_g and the fermion anisotropy ξ_f. The target spatial lattice spacing is of the order $a_s = 0.125$ fm with a target anisotropy of $\xi_g = \xi_f = 7.0$. This would give a very fine temporal lattice spacing

Target Parameters	
ξ_g	7.0
ξ_f	7.0
a_s	0.125fm
m_π/m_ρ	0.545

Table 5.1: The target output parameters for the tuning of the third generation of lattices.

$a_\tau = 0.018$ fm. The target parameters for this new generation of lattices is given in Table 5.1.

Tuning to the 3-flavour symmetric point reduces the number of tuned parameters as we use only a single quark mass. The strange quark mass can be set to its physical value after the tuning is completed. It is useful to use dimensionless quantities so we utilise the parameter m_π/m_ρ. To get this value, consider the Gell-Mann–Oakes–Renner (GMOR) relation

$$m_\pi^2 = (m_u + m_d)\langle\bar{\psi}\ \psi\rangle\frac{1}{f_\pi^2}, \tag{5.1}$$

where m_u and m_d are the masses of the up and down quarks respectively and f_π is the pion decay constant. This relation can be generalised for pseudoscalar consisting of any two quarks with masses m_1, m_2 as follows

$$m_{PS}^2 = (m_1 + m_2)\langle\bar{\psi}\ \psi\rangle\frac{1}{f_{PS}^2}. \tag{5.2}$$

Adhering to the QCDSF Collaboration's philosophy, we consider the plane in which the average quark mass is constant. On this plane a number of physical quantities are invariant. This reduces the number of parameters which need to be tuned. We need $m_u + m_d + m_s =$ constant and so we apply the generalised GMOR relation to the kaon.

$$m_K^2 = (m_l + m_s)\langle\bar{\psi}\ \psi\rangle\frac{1}{f_\pi^2}, \tag{5.3}$$

where m_l is the mass of the up or down quark. Now we consider the quantity $m_\pi^2 + 2m_k^2$.

$$m_\pi^2 + 2m_k^2 = 2m_l\langle\bar{\psi}\ \psi\rangle\frac{1}{f\pi^2} + 2(m_l + m_s)\langle\bar{\psi}\ \psi\rangle\frac{1}{f_\pi^2}$$

$$= \frac{2\langle\bar{\psi}\ \psi\rangle}{f_\pi^2}(2m_l + m_s)$$

$$= \frac{2\langle\bar{\psi}\ \psi\rangle}{f_\pi^2}(m_u + m_d + m_s). \tag{5.4}$$

We can see that $m_\pi^2 + 2m_K^2$ is a good choice of parameter, but we would like to have a dimensionless quantity. The vector meson mass is linear in the quark mass, and we can use this to obtain the dimensionless quantity

$$\frac{m_\pi^2 + 2m_K^2}{(m_\rho + 2m_{K^*})^2}. \tag{5.5}$$

As we are tuning to the 3 flavour symmetric point, the masses of the up, down and strange quarks are degenerate, i.e. $m_u = m_d = m_s$. Thus we also have $m_\pi = m_K$ and $m_\rho = m_{K^*}$, yielding

$$\begin{aligned}\frac{m_\pi^2 + 2m_K^2}{(m_\rho + 2m_{K^*})^2} &= \frac{m_\pi^2 + 2m_\pi^2}{(m_\rho + 2m_\rho)^2} \\ &= \frac{3m_\pi^2}{(3m_\rho)^2} \\ &= \frac{1}{3}\left(\frac{m_\pi}{m_\rho}\right)^2. \end{aligned} \tag{5.6}$$

Now, to find the value of m_π/m_ρ, I used the meson masses in lattice units provided by Lin et al in reference [64]. This results in a mass ratio of $m_\pi/m_\rho = 0.545$, corresponding to a pseudoscalar pion mass of 496MeV.

Using equation (4.1), the clover coefficients c_s and c_t were calculated. Here, the anisotropy is set to the target value of $\xi = 7.0$. The smeared mean links $\tilde{u}_s$ and $\tilde{u}_t$ were recalculated after the system had thermalised to keep the parameters self-consistent. The Rational Hybrid Monte Carlo (RHMC) method was used to generate the gauge configurations [139]. This was done using the Chroma software package [140] with computational facilities provided by the Irish Centre for High End Computing (ICHEC) and the Distributed Research utilising Advanced Computing (DiRAC). I then computed the Wilson flow for these configurations which enabled me to calculate ξ_g and a_s. This method is detailed in Section 5.3.2. I also calculated the dispersion relations for the pion and rho meson, giving results for ξ_f and m_π/m_ρ. Details of this can be found in Section 5.3.6.

Tuning four parameters simultaneously requires a number of iterations of the process. For an initial estimate of the input parameter γ_g, linear equations were built using an isotropic system which gives $\gamma_g = \gamma_f = \xi = 1$ and the second generation parameters for which $\gamma_g = 4.3$ and $\xi = 3.5$ yielding

$$\gamma_g = A + B\xi$$

$$\Rightarrow 1 = A + B(1);$$

$$4.3 = A + B(3.5), \tag{5.7}$$

where A and B are constants. Solving this system of equations results in $\gamma_g = 8.412$. A similar process was used to estimate $\nu = \gamma_g/\gamma_f = 1.636$. The strange quark mass in lattice units is $a_\tau m_s = -0.073$ from the second generation ensembles. In the third generation the aim is to halve a_τ, so a rough estimate for the mass is $a_\tau m_s = -0.03$. As a conservative guess, I began by using $a_\tau m_0 = 0$. The lattice coupling $\beta = 1.5$ was left unchanged from the second generation. Once the results for the output parameters were obtained, minor adjustments were made for the next iteration. Examining the results obtained by slight variations in one or two parameters in each iteration gave insight into the dependence of the output parameters on the input and allowed us to perform an improved interpolation to the desired values. A detailed account of the analysis is provided in Sections 5.3.5 and 5.3.7.

The input parameters for each run are shown in Table 5.2 and the results are given in Tables 5.3, 5.4. Runs 1 - 9 have been omitted as an error was made in the calculation of the clover coefficients. As the resulting parameters depend on these coefficients we cannot have any confidence in their accuracy. Run 13 has also been omitted as it contained a non-degenerate strange quark mass.

5.3 Method

In calculating the target parameters the Wilson flow and the meson dispersion relation are used. These methods are detailed in this section. I also studied the effect of smearing on the parameters and included it in many of the later runs. First, a brief account of smearing.

5.3.1 Smearing

Quark and gluon fields may be smeared in order to improve the measurements made using their correlation functions. Smearing is introduced in order to reduce the unphysical fluctuations at short distances on the lattice and to account for the finite size of a hadron. While this results in a stronger signal, there is also a stronger distortion close to the source. The quarks and gluons are smeared independently using different methods.

For the gluons, stout link smearing is employed which is detailed in reference [62]. A weighted average of neighbouring plaquettes is added to the links on the lattice and this is iterated a number of times to obtain the final smeared link variables. A Hermitian, traceless matrix $Q_\mu(x)$ is introduced in order to

Run no.	β	γ_g	γ_f	$a_\tau m_0$
10	1.65	9.0	5.5	-0.01
11	1.65	9.0	6.4	-0.01
12	1.65	9.0	6.9	-0.02
14	1.68	9.0	6.9	-0.01
15	1.68	7.5	5.8	-0.01
16	1.68	9.0	7.5	-0.01
17	1.68	7.5	6.25	-0.01
18	1.75	9.0	7.5	-0.01
19	1.68	9.0	6.9	-0.02
20	1.68	9.0	6.9	-0.022
21	1.68	9.0	7.5	-0.025
22	1.7	9.0	6.9	-0.022
23	1.7	9.0	7.5	-0.025
24	1.7	8.0	6.7	-0.025
25	1.75	8.0	6.7	-0.01
26	1.75	8.0	6.7	-0.02
27	1.75	8.0	6.7	-0.025
28	1.75	8.0	6.7	-0.028
29	1.75	8.0	7.3	-0.025
30	1.7	8.3	8.3	-0.03
31	1.6	9.5	7.5	-0.025
32	1.6	10.0	8.0	-0.01
33	1.7	8.3	8.3	-0.038
34	1.6	9.5	7.5	-0.03
35	1.6	9.5	8.0	-0.025
36	1.6	9.5	7.0	-0.023
37	1.6	9.0	7.5	-0.025
38	1.6	10.0	7.5	-0.025
39	1.58	9.5	7.5	-0.025
40	1.62	9.5	7.5	-0.025

Table 5.2: Input parameters for each tuning run. Note that runs 1-9 have been omitted as an error was made in calculating the clover coefficients. Run 13 is omitted as it had $2+1$ denegerate quark flavours.

Run no.	ξ_g	$\xi_f(\pi)$	$\xi_f(\rho)$	a_s	m_π/m_ρ
10	7.8(2)	4.9(1)		0.1141(19)	0.76(4)
11	7.2(2)	6.1(3)		0.1395(12)	0.805(18)
12	7.19(7)	6.8(1)	6.71(7)	0.1633(9)	0.716(6)
14	7.05(4)	5.9(1)	6.3(1)	0.1677(6)	0.819(5)
15	5.83(3)	6.6(1)	6.29(8)	0.2090(8)	0.679(7)
16	7.05(12)	7.1(1)		0.1889(8)	0.831(8)
17	6.03(2)	5.99(8)	6.1(1)	0.2273(3)	0.862(3)
18	7.75(18)	7.2(1)		0.183(1)	0.824(5)
19	6.80(6)	5.6(1)	4.64(4)	0.1273(7)	0.804(8)
20	7.72(7)	6.3(2)	6.9(1)	0.1263(6)	0.605(9)
21	8.1(1)	6.9(1)	7.32(9)	0.146(1)	0.613(6)
22	7.6(1)	5.7(1)		0.1167(7)	0.64(1)
23	6.99(9)	6.0(1)	6.89(7)	0.140(2)	0.661(5)
24	6.83(22)	6.34		0.1601(14)	0.759(9)
25	6.6(1)	6.3(1)		0.1917(9)	0.846(5)
26	7.02(19)	7.0(1)		0.169(2)	0.75(2)
27	6.61(19)	6.14(5)		0.144(1)	0.73(1)
28	7.49(27)	6.3(2)	5.80(4)	0.139(1)	0.67(1)
29	7.0(3)	6.10(13)	6.05(9)	0.175(2)	0.747(8)
31	7.41(9)	5.79(5)	6.05(2)	0.1292(5)	0.556(7)

Table 5.3: Output parameters for each tuning run calculated with point quark sources. Note that runs 1-9 have been omitted as an error was made in calculating the clover coefficients. Run 13 is omitted as it had $2+1$ denegerate quark flavours.

Run no.	ξ_g	$\xi_f(\pi)$	$\xi_f(\rho)$	a_s	m_π/m_ρ
24 (s)	6.8(2)	6.6(1)	6.34(7)	0.160(1)	0.727(7)
25 (s)	6.6(1)	7.1(3)	7.3(2)	0.1917(9)	0.611(9)
26 (s)	7.0(2)	6.77(7)	6.45(7)	0.170(2)	0.775(5)
27 (s)	6.6(2)	5.77(8)	6.05(2)	0.144(2)	0.698(4)
28 (s)	7.5(3)	6.3(1)	5.89(9)	0.139(1)	0.623(7)
29 (s)	7.0(3)	6.1(2)	6.26(9)	0.175(2)	0.755(5)
30 (s)	7.5(1)	7.94(7)	8.16(6)	0.1993(5)	0.728(2)
31 (s)	7.41(9)	5.50(5)	6.50(4)	0.1292(5)	0.563(6)
32 (s)	7.71(4)	7.6(1)	7.7(1)	0.1972(5)	0.819(3)
33 (s)	7.8(2)	6.4(2)	6.68(5)	0.1638(6)	0.37(2)
34 (s)	7.56(5)	6.01(7)	6.99(4)	0.1457(6)	0.550(4)
35 (s)	7.9(4)	6.74(5)	6.80(4)	0.1636(9)	0.564(6)
36 (s)	6.6(3)	5.5(2)	6.07(9)	0.1275(9)	0.483(12)
37 (s)	6.6(1)	7.27(3)	7.29(3)	0.366(4)	0.843(1)
38 (s)	8.35(5)	5.4(5)	6.24(3)	0.1465(5)	0.506(9)
39 (s)	7.4(1)	5.11(3)	6.85(6)	0.139(1)	0.52(1)
40 (s)	7.5(1)	6.9(1)	6.71(5)	0.125(1)	0.507(9)

Table 5.4: Output parameters for each tuning run calculated with smeared (s) quark sources and sinks. Note that runs 1-9 have been omitted as an error was made in calculating the clover coefficients. Run 13 is omitted as it had $2+1$ denegerate quark flavours.

ensure the resulting smeared link is an element of $SU(3)$. This matrix is given by

$$Q_\mu(x) = \frac{i}{2}\left[\Omega_\mu^\dagger(x) - \Omega_\mu(x)\right] - \frac{i}{2N}\mathrm{tr}\left[\Omega_\mu^\dagger(x) - \Omega_\mu(x)\right], \tag{5.8}$$

where

$$\Omega_\mu(x) = \sum_{\pm\nu\neq\mu} \rho_{\mu\nu} U_\nu(x) U_\mu(x+\hat{\nu}) U_\nu^\dagger(x+\hat{\mu}) U_\mu^\dagger, \tag{5.9}$$

is the generator of the stout smearing transformation and $\rho_{\mu\nu}$ are the smearing parameters. Thus the smeared link variable is defined to be

$$U_\mu^{(n+1)}(x) = \mathrm{e}^{iQ_\mu^{(n)}(x)} U_\mu^{(n)}(x). \tag{5.10}$$

Since $Q_\mu(x)$ is Hermitian and traceless, the exponential term is an element of $SU(3)$. Thus the smeared link variable must also be in $SU(3)$.

Quarks are smeared by replacing the point sources with sources which have a finite size. This is a more realistic interpretation of the quark source. Smeared operators are constructed from these finite-size sources and give an increased overlap in the lower energy states. This is advantageous in the calculation of ground state masses. A gauge-covariant scheme in which the smeared quark fields are substituted by a Gaussian weighted average of the surrounding sites on the same timeslice is implemented [141]. On the lattice, the smeared quark fields are then approximated by

$$\tilde{\psi}(x) = \left(1 + \frac{\sigma_s^2}{4n_\sigma}\Delta\right)^{n_\sigma} \psi(x), \tag{5.11}$$

where Δ is the 3-dimensional gauge covariant Laplacian

$$\Delta\psi(x) = \sum_{n=\pm1}^{\pm3} \left(U_n(x)\psi(x+\hat{n}) - \psi(x)\right), \tag{5.12}$$

σ_s is the smearing radius, and n_σ is the number of iterations for the smearing procedure.

For tuning these lattices, both gluon and quark smearing are used. The smearing parameters are kept consistent across all tuning runs. The weight parameter in equation (5.9) for link smearing is $\rho_{\mu\nu} = 0.14$ and the gauge-invariant Gaussian weight parameter is $\sigma_s = 1.2$ for the quark field smearing in equation (5.11).

5.3.2 Wilson Flow

The most popular method to determine the anisotropy in the gauge sector is by comparing the spatial-spatial to the spatial-temporal Wilson loops. In

dynamical simulations the statistical uncertainties are larger in the tuning process than in the quenched approximation. A more robust method to correctly tune the gauge anisotropy is required. A new method to achieve this was proposed by Borsányi et al in [142] which concentrates on the Wilson flow. This method is beneficial as it does not require the evaluation of large Wilson loops (which have a poor signal to noise ratio) nor does it rely on the interpolation of lattice data between the lattice sites.

The Wilson flow in the continuum is defined to be the solution of the differential equation

$$\frac{\mathrm{d}A_\mu}{\mathrm{d}\tau} = D_\nu F_{\nu\mu}, \tag{5.13}$$

where $A_\mu(x,\tau)$ is a gauge field with an initial condition at $\tau = 0$. The flow is parametrised by τ, which has dimensions of length squared. Lüscher showed that the gauge field defined by the flow is renormalised and no ultraviolet divergences appear to any order in perturbation theory for any time $\tau > 0$ [143]. In order to study the Wilson flow on the lattice, equation (5.13) must be discretised. The discrete flow equation has been studied in detail by Lüscher in [144] and is given by

$$\frac{\mathrm{d}U_\mu}{\mathrm{d}\tau} = Q_\mu(U)U_\mu, \tag{5.14}$$

where Q_μ is the generator of the stout smearing transformation given in equation (5.8). It is required that the smearing parameters obey $\rho_{i4} = \xi_g^2$ and $\rho_{ij} = \rho_{4i} = 1$ for the discrete flow equation to correctly reproduce the continuum equation (5.13). $\xi_g = a_s/a_\tau$ is the gauge anisotropy which describes the theory on the scale of the lattice spacing. Since for any time $\tau > 0$ the gauge field along the Wilson flow is already renormalised, we can conclude that the anisotropy parameter appearing in the Wilson flow is the renormalised gauge anisotropy ξ_g. In implementing the Wilson flow, successive stout smearing steps are taken on a gauge field configuration with a small smearing parameter.

5.3.3 Scale Setting with the Wilson Flow

In Section 1.3.4 I introduced the idea of scale setting for lattice calculations. A parameter is chosen to set the scale in order to attach a physical meaning to the results. As we are using the Wilson flow in this new generation of lattices, we set the scale with a parameter provided by the flow itself. One option is to use the $\sqrt{t_0}$ as presented by Lüscher in [145]. The Wilson flow is calculated up to a scale τ when a dimensionless observable reaches a preset value. The flow time taken to achieve this is $\tau = t_0$. To obtain t_0, the flow is integrated and the following equation solved.

$$\left[\tau^2\langle E(\tau)\rangle\right]_{\tau=t_0} = 0.3, \tag{5.15}$$

where $\langle E(\tau)\rangle$ is the quantum expectation value of the Yang-Mills action density given by

$$E(\tau) = \frac{1}{4}\sum_{x} F^2_{\mu\nu}(x,\tau). \tag{5.16}$$

However, $\tau^2\langle E(\tau)\rangle$ contains information about gauge configurations at scales larger than $\mathcal{O}(1/\sqrt{\tau})$. This is undesirable as it can include scales around the cut-off. Borsányi et al proposed a new scale which depends only on scales around $\mathcal{O}(1/\sqrt{\tau})$ and is called the w_0 scale [146]. It is particularly advantageous as the behaviour of the flow at small flow times $\sqrt{\tau} \sim a$ is subject to lattice discretisation effects. Also, it only has a minor quark mass dependence and its definition does not depend on any extrapolation. The w_0 scale is defined to be

$$\left[\tau\frac{\mathrm{d}}{\mathrm{d}\tau}\tau^2\langle E(\tau)\rangle\right]_{\tau=w_0^2} = 0.3, \tag{5.17}$$

where $\langle E(\tau)\rangle$ is the same action density as in equation (5.16). It is not possible to directly measure the w_0 scale in experiment, but its physical value was calculated in [146] to be $w_0 = 0.1755(18)(04)$ fm. Neither the $\sqrt{t_0}$ nor the w_0 scales require renormalisation. This was shown by perturbative calculation in [145]. The w_0 scale was calculated at various pion and kaon masses and was found to depend weakly on the quark mass. In this work we take $w_0 = 0.1755$ and do not consider the quark mass dependence. To calculate the Wilson flow coefficients we adopted the public code by Borsányi [146].

5.3.4 Obtaining ξ_g from the Wilson Flow

The parameter ξ_g can be determined from the Wilson flow calculations. We saw the Yang-Mills action density in equation (5.16). Now we consider the spatial and temporal components separately.

$$E_{ss}(\tau) = \frac{1}{4}\sum_{x,i\neq j} F^2_{ij}(x,\tau), \tag{5.18}$$

$$E_{st}(\tau) = \frac{1}{2}\sum_{x.i} F^2_{i4}(x,\tau). \tag{5.19}$$

The expectation values of E_{ss} and E_{st} in physical units are equal. Since for any $\tau > 0$ these operators are renormalised, we can use them to provide a definition for the renormalised gauge anisotropy. The ratio of the field strength tensors at a given point τ along the flow is given by

$$\frac{\langle a_s^4 E_{ss}(\tau)\rangle}{\langle a_s^2 a_t^2 E_{st}(\tau)\rangle} = \frac{a_s^4\langle E_{ss}(\tau)\rangle}{a_s^2 a_t^2\langle E_{st}(\tau)\rangle} = \frac{a_s^4}{a_s^2 a_t^2} = \frac{a_s^2}{a_t^2} = \xi_g^2. \tag{5.20}$$

For convenience, we will work in lattice units from this point forward. In

these units, the parameters become

$$a^4 E_{ss}(\tau) \to E_{ss}(\tau)$$

$$a_s^2 a_t^2 E_{st}(\tau) \to E_{st}(\tau)$$

$$\tau / a_s^2 \to \tau$$

$$w_0 / a_s \to w_0. \tag{5.21}$$

We will also adjust the definition of ξ_g to aid the calculations. For convenience, the ratio of derivatives of the action densities is used instead of using the field tensors directly. This yields the ratio

$$R_E \equiv \xi_g^2 = \frac{\left[\tau \frac{\mathrm{d}}{\mathrm{d}\tau} \tau^2 \langle E_{ss}(\tau) \rangle\right]_{\tau = w_0^2}}{\left[\tau \frac{\mathrm{d}}{\mathrm{d}\tau} \tau^2 \langle E_{st}(\tau) \rangle\right]_{\tau = w_0^2}}. \tag{5.22}$$

Note that the spatial component of this ratio is the w_0 scale as in equation (5.17).

For our calculations we made a minor adjustment to this scheme. We define two parameters w_s and w_t and treat space and time differently.

$$\left[\tau \frac{\mathrm{d}}{\mathrm{d}\tau} \tau^2 \langle E_{ss}(\tau) \rangle\right]_{\tau = w_s^2} = 0.15, \tag{5.23}$$

$$\left[\tau \frac{\mathrm{d}}{\mathrm{d}\tau} \tau^2 \langle E_{st}(\tau) \rangle\right]_{\tau = w_t^2} = \frac{0.15}{\xi_w^2}, \tag{5.24}$$

where ξ_w is an estimate for the gauge anisotropy parameter used in the flow equation.

In order to solve the equations for ξ_g, w_s and w_t, the Wilson flow is evaluated at a number of anisotropy parameters $\rho_{i4} = \xi_w^2$ and $\rho_{ij} = \rho_{4i} = 1$ in equation (5.9). We choose five values of ξ_w ($\xi_w = 6.0, 6.5, 7.0, 7.5, 8.0$) for which we obtain the gauge anisotropy ξ_g and we are then able to interpolate a result $\xi_g = \xi_w$. Thus the gauge anisotropy is determined by

$$\xi_g = \xi_w \Big|_{w_s / w_t = 1}. \tag{5.25}$$

For each ξ_w the flow time τ for which the equations (5.23), (5.24) hold is calculated and this is then input into equation (5.25)

It is a simple matter to extend this calculation to compute the spatial lattice

Input Parameters	
β	1.6
γ_g	9.5
γ_f	7.5
$a_\tau m_\tau$	-0.025

Table 5.5: Input parameters for tuning run 31.

ξ_w	w_s	w_t
6.0	1.349(18)	1.486(19)
6.5	1.353(17)	1.434(18)
7.0	1.353(17)	1.385(18)
7.5	1.352(16)	1.341(17)
8.0	1.350(16)	1.301(17)

Table 5.6: Wilson flow coefficients w_s and w_t with errors for different values of ξ_w calculated for run 31 parameters on a $12^3 \times 128$ lattice with 166 configurations.

spacing as follows

$$a_s = \frac{w_0}{w_s}. \tag{5.26}$$

This is shown in detail in Section 5.3.5.

5.3.5 Results for ξ_g and a_s from the Wilson Flow

I will use tuning run 31 to illustrate how the Wilson flow achieves the desired results. The input parameters for this run are given in Table 5.5. Table 5.6 shows the Wilson flow output w_s and w_t with errors for 5 different values of ξ_w. This was calculated on a $N_s^3 \times N_t = 12^3 \times 128$ lattice with 166 configurations.

The Wilson flow produces values for w_s and w_t. The ratio of these numbers then provides the gauge anisotropy $\xi_g = w_s/w_t$. The resulting values for ξ_g are plotted along with a linear fit. This is shown in Figure 5.1. The dashed horizontal line $w_s/w_t = 1$ is included and the interpolated gauge anisotropy $\xi_g = 7.41(9)$ is then given by its point of intersection with the linear fit.

The statistical uncertainties are calculated using the bootstrap method. Bootstrap sets are generated from the data set by choosing a data point at random, replacing it, and repeating this process. I used 100 bootstrap samples as standard for every data set.

The spatial lattice spacing a_s is determined by equation (5.26). a_s is calculated for each value of ξ_w and the results are plotted with a linear fit as shown in Figure 5.2. Included in this plot is a dashed vertical line representing the calculated value for the renormalised gauge anisotropy ξ_g. The intersection

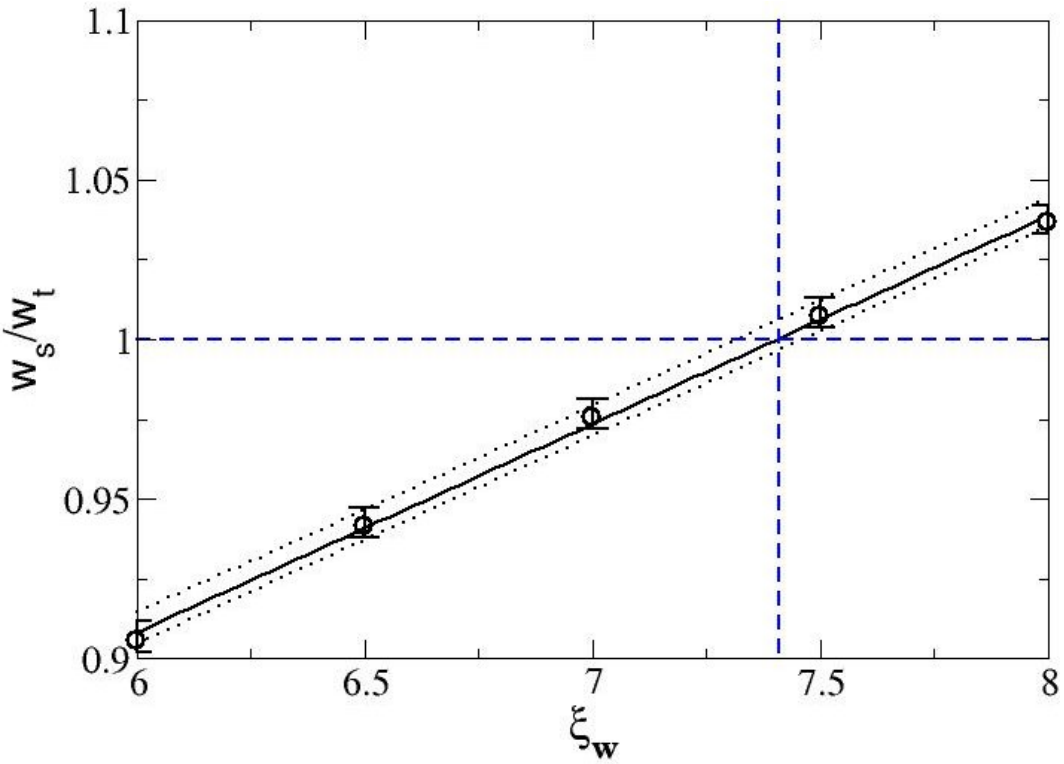

Figure 5.1: Ratio of Wilson coefficients against the chosen anisotropy values ξ_w for run 31. The intersection of the dashed horizontal line at $w_s/w_t = 1$ and the linear fit gives the gauge anisotropy ξ_g, which is respresented by the dashed vertical line.

of this line with the linear regression gives the spatial lattice spacing for this set of parameters. There is a very weak dependence on ξ_w for this set of parameters. In general, I have found this dependence may be stronger.

5.3.6 Meson Dispersion

The meson dispersion relation can be used to calculate the mass ratio m_π/m_ρ at zero momentum and the fermion anisotropy ξ_f at small momentum. On an anisotropic lattice, this dispersion relation is given by

$$a_\tau^2 E^2 = a_\tau^2 m_0^2 + \frac{a_s^2 p^2}{\xi_f^2}, \tag{5.27}$$

where E is the energy and p is the momentum on the lattice given by

$$p^2 = \frac{4}{a_s^2}\left[\sin^2\left(\frac{a_s p_x}{2}\right) + \sin^2\left(\frac{a_s p_y}{2}\right) + \sin^2\left(\frac{a_s p_z}{2}\right)\right]. \tag{5.28}$$

The effective mass (in lattice units) $a_\tau m_{\text{eff}}(\tau)$ for the π and ρ mesons can be calculated from the correlator using the definition in equation (4.4). At large τ a plateau should be visible in the effective mass plots at each momentum value. This plateau provides the fitting range for the final mass value. The mass ratio

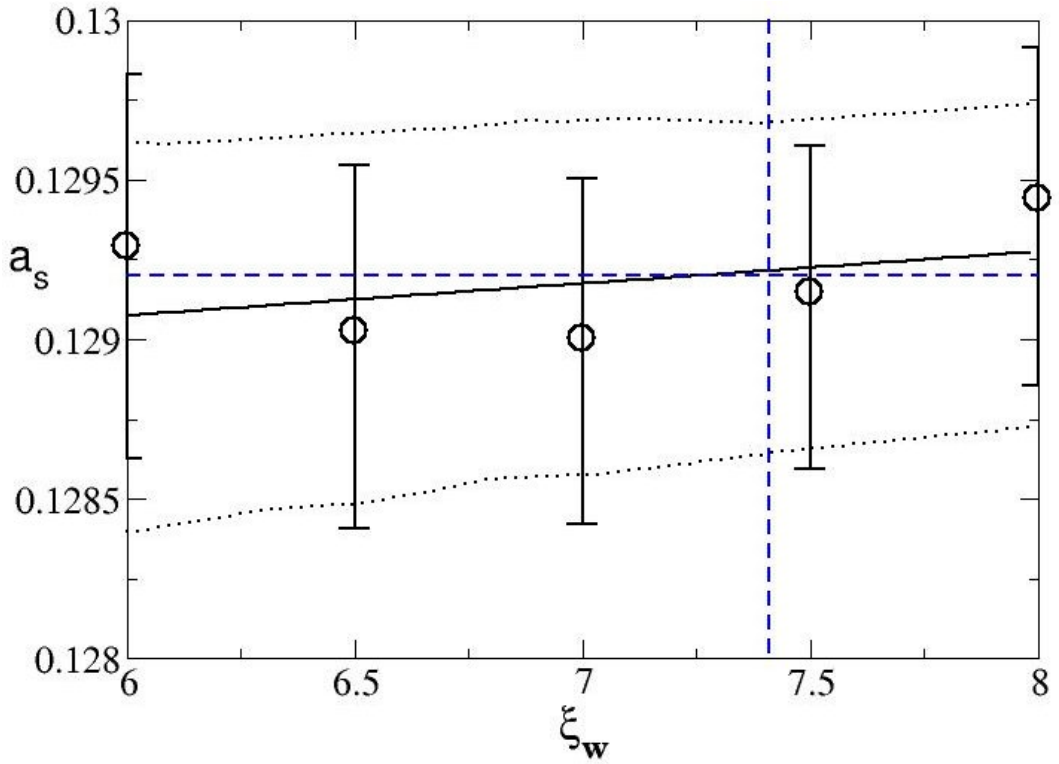

Figure 5.2: a_s values for each ξ_w fitted to a linear regression the the run 31 parameters. The dashed vertical line is the calculated gauge anisotropy ξ_g for this set of data.

m_π/m_ρ is then determined from these fits.

For small momentum we can see in equation (5.27) that the fermion anisotropy can be determined by the slope of the dispersion relation. Once the linear fit at each momentum value is complete, its slope is given by $1/\xi_f^2$.

5.3.7 Results for ξ_f and m_π/m_ρ from the Dispersion Relation

The dispersion relation is calculated for the pion and rho meson for each tuning run. This yields the results for the fermion anisotropy ξ_f, the pion mass (in lattice units) $a_\tau m_\pi$, the ratio of the pion mass to the ρ meson mass m_π/m_ρ and the effective energies at different momenta. The fermion anisotropy should equal the gauge anisotropy, and the target value is $\xi_f = 7.0$. Again, tuning run 31 is used to describe the method.

The dispersion relation at zero momentum yields the effective mass. I present the effective masses for both the pion and the ρ meson in Figure 5.3. A plateau is achieved at the value of the mass for each meson, giving a ratio of $m_\pi/m_\rho = 0.556(7)$. At non-zero momentum, the dispersion relation produces the effective energies of the π and ρ mesons. In Figure 5.4 the effective energies

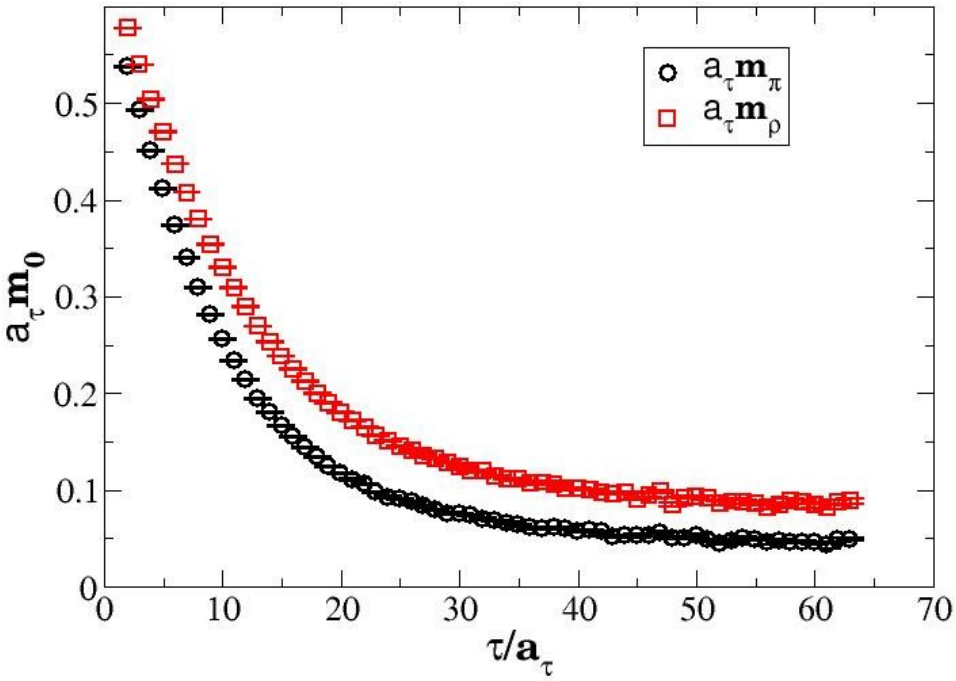

Figure 5.3: The effective mass for the pion and rho meson calculated using the parameters given in tuning run 31.

Fit Ranges							
n^2	0	1	2	3	4	5	6
π	34–63	34–56	23–35	28–47	26–36	25–38	22–34
ρ	39–63	39–63	23–45	32–63	26–43	25–47	25–40

Table 5.7: The values of τ/a_τ used for each momentum value $a_s^2 p_n^2 = \left(\frac{2\pi}{N_s}\right)^2 n^2$ to calculate the fermion anisotropy ξ_f of the π and ρ mesons.

for each meson are presented for each momentum value given by

$$a_s^2 p_n^2 = \left(\frac{2\pi}{N_s}\right)^2 n^2, \tag{5.29}$$

where $n^2 = n_x^2 + n_y^2 + n_z^2 = 0, 1, 2, 3, 4, 5, 6$. The statistical uncertainties at high momentum are very large. Beyond $a_s p_1^2$, a plateau is difficult to discern. As the plateaux are used to determine the fitting ranges for the fermion anisotropy, this can affect the output value ξ_f. The fitting ranges chosen for run 31 are given in Table 5.7. At high momentum , the dispersion relation for the ρ meson is less noisy than for the pion. Thus ρ gives a better determination of the fermion anisotropy.

Figure 5.5 shows the dispersion relation for the pion and the rho meson with both smeared and unsmeared sources. We see a significant difference in the energies calculated with smeared sources compared to the calculation with point sources. This affects the fermion anisotropy as it is inversely related

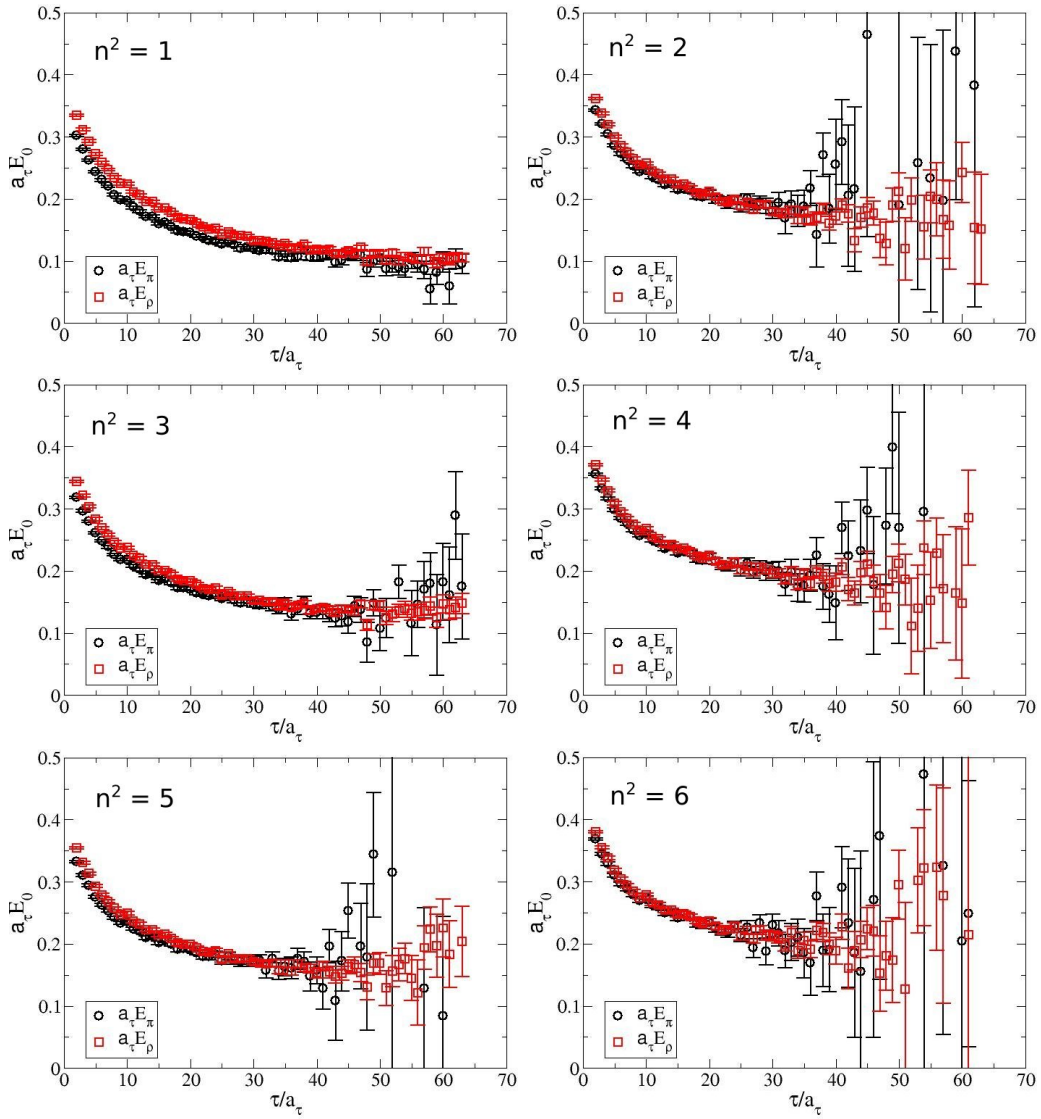

Figure 5.4: The effective energies at each momentum value for the parameters given in tuning run 31 calculated using $a_s^2 p_n^2 = \left(\frac{2\pi}{N_s}\right)^2 n^2$.

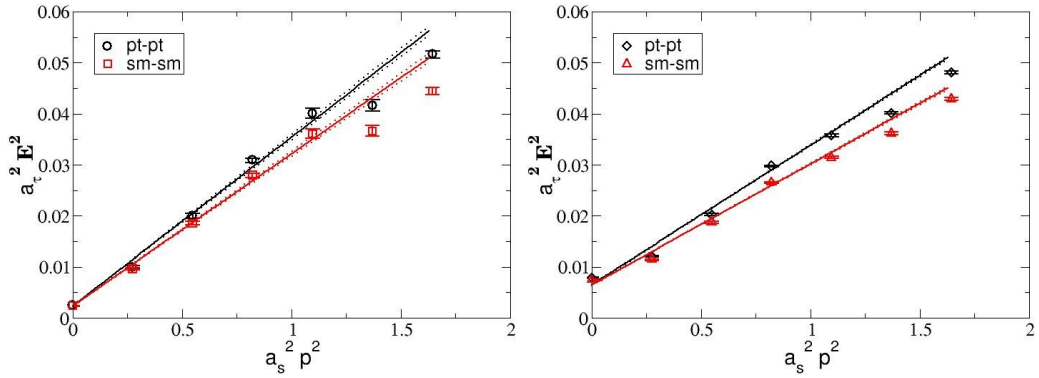

Figure 5.5: The dispersion relation for the pion (left) and rho meson (right) calculated with point sources and smeared sources for the parameters given in tuning run 31.

to the slope of the line. The fermion anisotropy for the pion increases from 5.50(5) to 5.79(5) and for the ρ meson increases from 6.05(2) to 6.50(4) for run 31. The mass ratio is also affected. Including smeared sources and sinks $m_\pi/m_\rho = 0.563(6)$, and with point sources we obtain $m_\pi/m_\rho = 0.556(7)$.

5.4 Tuning Results

Tuning an anisotropic lattice is not an easy task. The inclusion of the bare gauge and fermion anisotropies gives two additional parameters on which the output parameters may depend. The use of the clover action also complicates matters as the clover coefficients must be considered in the tuning process. We have found that the output parameters are indeed heavily dependent on the clover coefficients. We attempted to reduce the difficulties in this area by detemining c_s and c_t self-consistently using equation (4.1).

For tuning runs 10–30 small adjustments were made to the input parameters to test the dependence of the output parameters on them. After analysing each run we made an estimate of a reasonable value for β, γ_g, γ_f, and $a_\tau m_0$ in order to reach the target results, which are given in Table 5.1. β was increased in runs 18, 22–29 in an effort to reduce the lattice spacing. A preliminary analysis of these runs was carried out in which we assumed a linear ansatz across the parameters from each run. This fit provided us with a sensible set of input parameters which became run 31. Minor adjustments were made to this in runs 34-40 to test the variance of the output parameters and the strength of their dependence on each input parameter.

The quark mass dependence may be studied by focusing on runs 25–28. Figure 5.6 shows the dispersion relations for these runs calculated with smeared sources. The dispersion relations of the ρ meson are more consistent with one another than those of the π meson. This is mirrored in the effective energies of the π and ρ mesons. The fermion anisotropy is therefore more consistent

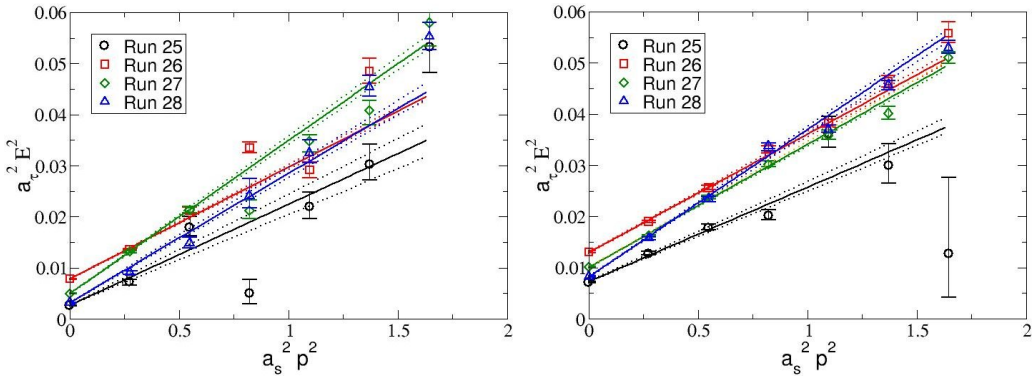

Figure 5.6: The dispersion relations for the pion (left) and ρ meson (right) calculated with smeared sources for tuning runs 25, 26, 27, 28.

when calculated from the ρ meson data. The results for all output parameters are provided in Table 5.4. As the quark mass is decreased, the spatial lattice spacing a_s decreases. However there is a non-trivial effect apparent in the gauge anisotropy ξ_g. It neither increases nor decreases monotonically. This is also true of the mass ratio m_π/m_ρ, making it difficult to ascertain the true nature of the quark mass dependence.

Runs 19, 20, 21 also display the effect of changing the quark mass. We present the results for the dispersion relation, ξ_g, and a_s for these runs in Figure 5.7. The bare fermion anisotropy γ_f was also increased in run 21. There is a notable difference in the dispersion relations of the pion and ρ meson in run 19. The fermion anisotropy ξ_f calculated from the ρ dispersion relation is much smaller than that of the pion. The data points do not fit well onto a line and this may explain the disparity. The fermion and gauge anisotropies for runs 20 and 21 are in good agreement, suggesting that increasing γ_f while decreasing $a_\tau m_0$ provides a stable set of output parameters. The mass ratio for run 20 is $m_\pi/m_\rho = 0.605(9)$ and for run 21 is $m_\pi/m_\rho = 0.613(6)$. While these results are considerably higher than the target ratio, their agreement supports the argument for simultaneously increasing γ_f. However, in the bottom right plot, the spatial lattice spacing vastly differs for these two runs. Further ajustments must be made to accommodate a_s.

We further test the relationship between the quark mass and bare fermion anisotropy with runs 31, 35, 36. The lattice coupling β and the bare gauge anisotropy γ_g are again kept constant and we vary γ_f and $a_\tau m_0$. The results are presented in Figure 5.8. The dispersion relations for the pion and the ρ meson are in good agreement. However, in the calculation of ξ_g we see a much larger difference between the three runs. It is difficult to distinguish exactly how ξ_g depends on the quark mass and bare fermion anisotropy. In run 36, the quark mass from run 31 was increased very slightly ($-0.025 \rightarrow -0.023$) while γ_f was decreased from 7.5 to 7.0. The results for the spatial lattice spacing

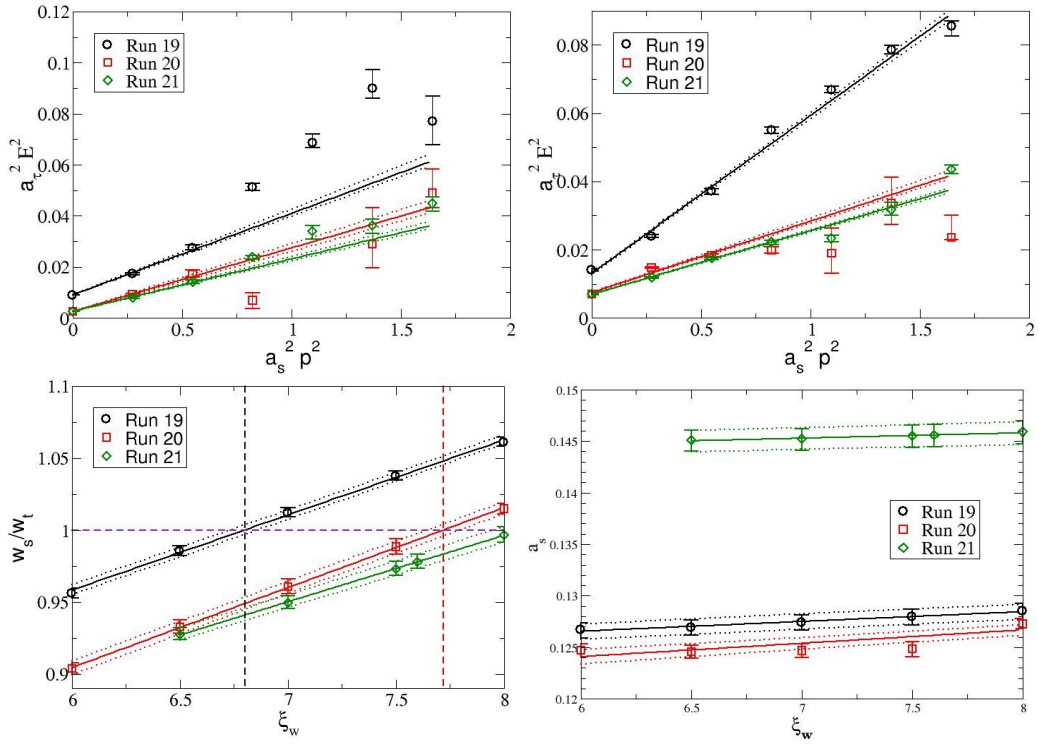

Figure 5.7: Top row: Dispersion relations for the π (left) and ρ (right) mesons for runs 19, 20, 21. Bottom row: Gauge anisotropy (left) and spatial lattice spacing (right) for runs 19, 20, 21. The intersection of the dashed horizontal line at $w_s/w_t = 1$ with the linear fits in the plot for ξ_g yields ξ_g for each run. These values are represented by the dashed vertical lines.

are consistent. An increase in γ_f without a corresponding adjustment in the mass has a huge effect on a_s which can be seen by comparing run 31 to run 35. From run 35 to run 36 both γ_f and $a_\tau m_0$ were decreased and this gives a desirable result for a_s.

The dependence of the output parameters on the lattice coupling β can be studied using runs 31, 39, 40. These results are presented in Figure 5.9. The dispersion relations for the π and ρ mesons agree quite well. The value for the gauge anisotropy ξ_g is very similar for each run. Looking at runs 31 and 39, decreasing β from 1.6 to 1.58 has had no effect on ξ_g. Comparing runs 31 and 40 we see that increasing β from 1.6 to 1.62 has a marginal effect on ξ_g, increasing it from 7.4 to 7.5. The spatial lattice spacing shows a strong dependence on β. Even for such minor adjustments, a_s is significantly changed. Decreasing β causes a_s to increase away from its target value.

Overall, runs 31 and 40 are the closest to the target parameters. These runs have been extended to test the finite volume effects on the parameters. New sets of gauge configurations with the input parameters for runs 31 and 40 are currently in production on a $N_s^3 \times N_\tau = 24^3 \times 256$ lattice. The increased number of temporal data points will reduce the statistical uncertainties and the difficulties in the calculation of γ_f. We hope that a repetition of our analysis

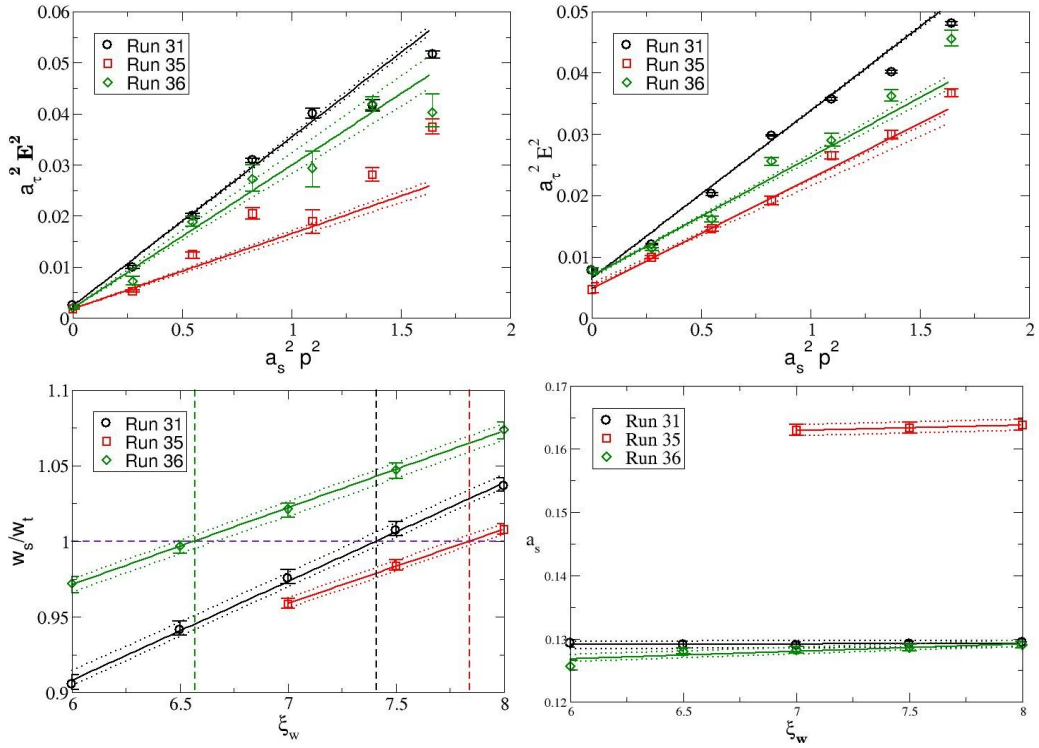

Figure 5.8: Top row: Dispersion relations for the π (left) and ρ (right) mesons for runs 31, 35, 36. Bottom row: Gauge anisotropy (left) and spatial lattice spacing (right) for runs 31, 35, 36. The intersection of the dashed horizontal line at $w_s/w_t = 1$ with the linear fits in the plot for ξ_g yields ξ_g for each run. These values are represented by the dashed vertical lines.

on these configurations will provide the target tuning parameters.

5.5 Conclusion

The aim of this chapter is to outline the method by which we tune the defining parameters of a third generation of lattices. These new ensembles will be an improvement on the second generation of anisotropic lattices which has anisotropy $\xi = 3.5$ and $2 + 1$ dynamical flavours of fermions. The objective is to double the anisotropy by halving the temporal lattice spacing and keeping all other parameters constant. I have presented the preliminary tuning of the lattice coupling β, the bare gauge and fermion anisotropies γ_g, γ_f, and the quark mass in lattice units $a_\tau m_0$. The results for the gauge and fermion anisotropies ξ_g and ξ_f, the spatial lattice spacing a_s and the mass ratio of the π and ρ mesons m_π/m_ρ are presented. I have found there are strong, non-trivial dependencies of the output parameters on the input and on the clover coefficients, which depend on γ_f.

The results for the output parameters in each run have been approximated by a linear fit and interpolated to an exact result. By comparing these results across a number of tuning runs we have identified two likely sets of parameters

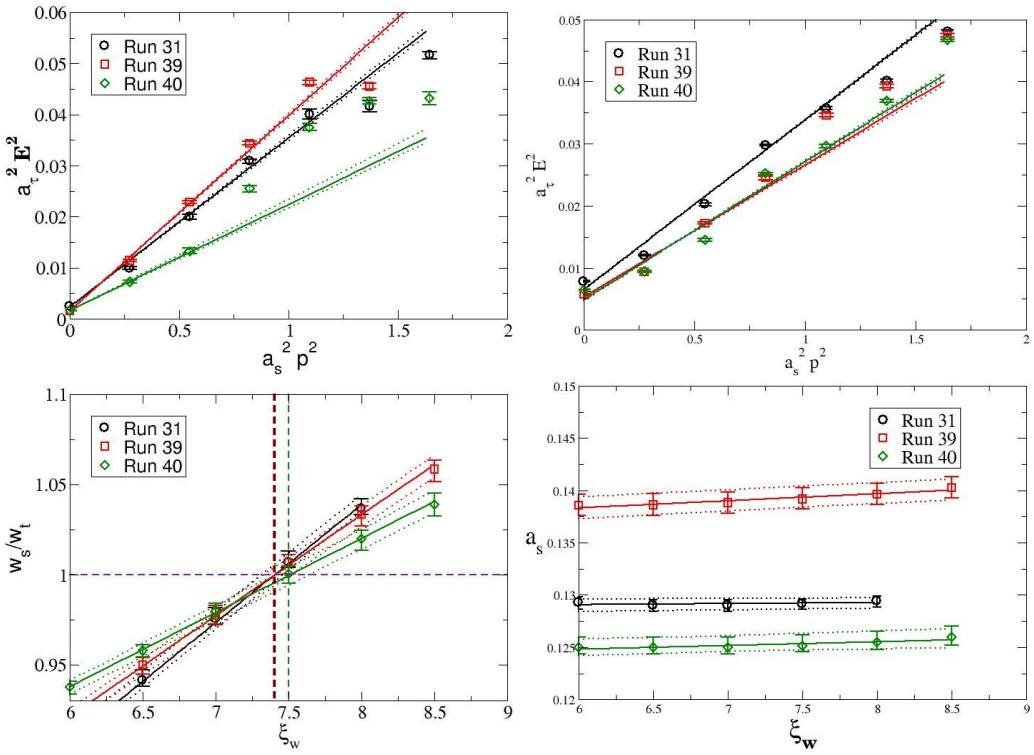

Figure 5.9: Top row: Dispersion relations for the π (left) and ρ (right) mesons for runs 31, 39, 40. Bottom row: Gauge anisotropy (left) and spatial lattice spacing (right) for runs 31, 39, 40. The intersection of the dashed horizontal line at $w_s/w_t = 1$ with the linear fits in the plot for ξ_g yields ξ_g for each run. These values are represented by the dashed vertical lines.

that give results close to the target value in runs 31 and 40. New configurations for these parameters are currently being generated on a larger volume to analyse the finite volume effects. The larger number of temporal data points will also enable us to calculate γ_f more accurately.

A preliminary analysis of the spectral function of Upsilon at high temperature with non-relativistic QCD (NRQCD) data has been done with the run 31 parameters. The results have been presented in [147] and are shown in Figure 5.10 alongside the second generation result. There is clear agreement between the two spectral functions suggesting that the run 31 parameters are close to the target values.

The next step is to fit the measured output parameters from every tuning run and interpolate an ideal set of parameters. Taking run 31 as a central parameter set to which we relate the parameters of the remaining tuning runs, the following system of linear equations can be set up

$$\Delta a_s = c_{11}\Delta\beta + c_{12}\Delta\gamma_g + c_{13}\Delta\gamma_f + c_{14}\Delta m_0$$

$$\Delta\xi_g = c_{21}\Delta\beta + c_{22}\Delta\gamma_g + c_{23}\Delta\gamma_f + c_{24}\Delta m_0$$

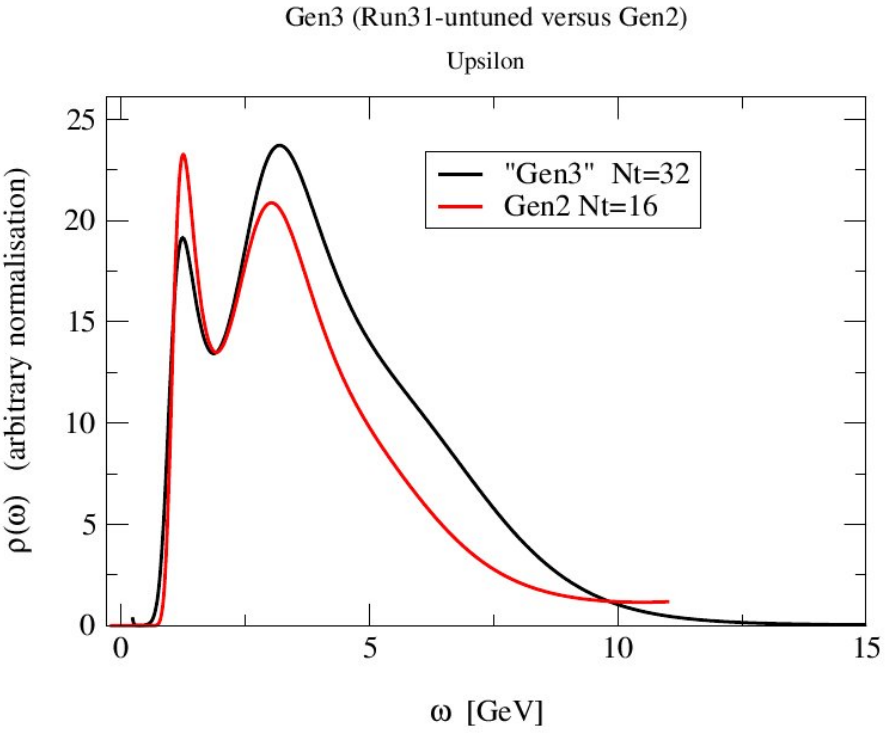

Figure 5.10: Comparison of the Upsilon spectral function using the third generation's run 31 parameters and the second generation parameters [147].

$$\Delta\xi_q = c_{31}\Delta\beta + c_{32}\Delta\gamma_g + c_{33}\Delta\gamma_f + c_{34}\Delta m_0$$

$$\Delta m_\pi^2 = c_{41}\Delta\beta + c_{42}\Delta\gamma_g + c_{43}\Delta\gamma_f + c_{44}\Delta m_0, \tag{5.30}$$

where

$$\Delta A = \frac{A - A^{(0)}}{A^{(0)}} \tag{5.31}$$

for some parameter A, and the parameters superscripted by (0) take their values from run 31. The coefficients c_{ij} for $i, j \in \{1, 2, 3, 4\}$ can then be calculated and we solve the matrix equation

$$\begin{pmatrix} \Delta\beta \\ \Delta\gamma_g \\ \Delta\gamma_q \\ \Delta m_0 \end{pmatrix} = \Big(C_{ij}\Big)^{-1} \begin{pmatrix} \Delta a_s \\ \Delta\xi_g \\ \Delta\xi_q \\ \Delta m_\pi^2 \end{pmatrix} \tag{5.32}$$

resulting in an interpolated set of tuned input parameters.

Once the parameters have been tuned to their target values, the strange quark mass will be separated from the light quarks and set to its physical value. We can then begin production. Imaginary time correlators and spectral functions for hadrons at finite temperature may be calculated to a higher precision on this new set of ensembles. The accuracy of the spectral functions

in the charm sector will be improved and the P-wave states may become accessible. These ensembles will also provide the foundation for the future studies of hadrons and transport properties in the medium with improved accuracy such as the electrical conductivity and heavy quark diffusion, baryons, and NRQCD dynamics in the bottom sector.

Conclusions and Outlook

The quark-gluon plasma is predicted to have existed in the early stages of the universe. It exists at very high temperatures and densities. Little is yet known about its internal properties. In this thesis I utilised the charm quark to probe the QGP at high temperatures. Chapter 2 gives a detailed account of the methods employed to study the dynamical properties of the QGP. As J/ψ suppression is conjectured to be a signal for deconfinement, it is vital to understand the interactions of this meson with the medium.

In Chapter 3 I focus on the J/ψ meson. I presented the spectral functions obtained for charmonium from the conserved vector current at zero and finite momentum. At $p = 0$, the J/ψ appears to survive at temperatures above the deconfinement crossover, and subsequently melts at temperatures of $1.2 - 1.4T_c$. The systematic uncertainties in the method make it difficult to ascertain the exact temperature at which J/ψ dissociates and as such it is possible that the meson survives beyond these temperatures.

For the finite momentum studies, the vector current correlator was decomposed into its transverse and longitudinal components. These were analysed separately and the longitudinal polarisation was found to be less stable than the transverse polarisation. At $p > 0$, J/ψ again appears to dissociate at temperatures of $1.2 - 1.4T_c$. It is unclear if the melting of J/ψ depends on the momentum as the results are dominated by systematic uncertainties.

The heavy quark diffusion coefficient may be calculated by examining the low frequency region of the J/ψ spectral functions. My analysis has revealed an approximate range for the height of the transport peak. The quark number susceptibility acts as a normalisation factor for this calculation, which has not yet been determined. I leave this for future work. The transport peak is expected to have a finite width at non-zero momentum and this was not the case. While this may be due to our high momentum values, we cannot be certain of this. Further analysis is required to understand this discrepancy.

In Chapter 4 we consider the correlators and spectral functions of open charm mesons. I have found significant medium modifactions, not only at high temperature but also at $T = 0.84T_c$. This is evident in the reconstructed correlators of both the D and D_s meson in the pseudoscalar and vector channels.

It is worth noting that these modifications are weaker for D_s. The spectral functions at finite temperature have also been examined. There is no evidence of survival for either the D or D_s meson beyond T_c. A thermal mass shift has been detected at a temperature of $T = 0.76T_c$. At present we are not certain of the true nature of this feature, and further analysis of the spectral functions for D mesons is required.

A first-look analysis of charmonium spectral functions for the S- and P-waves is also presented. A significant thermal effect appears in the reconstructed correlators for each meson. The P-waves have a zero mode which may contribute to this, and as such we are uncertain how strong this effect is for these states. Analysis of the spectral functions indicates that the S- and P-waves dissociate at temperatures $T \sim T_c$. My analysis of the J/ψ meson in the previous chapter gave a slightly different result, indicating the need for further study to ascertain the temperature at which these mesons dissociate.

One of the main sources of the systematic uncertainties I encountered is the small number of temporal data points available on the high temperature lattices. I have found that MEM has difficulties reconstructing the spectral functions with fewer than $N_\tau \sim 25$ points. In Chapter 5 I describe the method for generating a new set of ensembles which will double N_τ by halving the temporal lattice spacing a_τ. For these highly anisotropic lattices with a clover fermion action, there are four parameters which must be tuned — the lattice coupling β, the bare gauge anisotropy γ_g, the bare fermion anisotropy γ_f, and the quark mass (in lattice units) $a_\tau m_0$. Preliminary results for the gauge and fermion anisotropies ξ_g and ξ_f, the spatial lattice spacing a_s and the mass ratio of the π and ρ mesons m_π/m_ρ were presented. I have found that these parameters have a strong, non-trivial dependence on the input parameters and on the clover coefficients.

The preliminary estimates for the tuned values were approximated by a linear fit, yielding two likely sets of parameters. The finite volume effects of the lattice are currently being tested on these parameters by producing new configurations on a lattice with a much larger volume. Once complete, we hope to have our output parameters tuned to their target values. In the initial tuning process we consider three flavours of dynamical quarks. Once this procedure has been completed, the strange quark mass may be separated from the mass of the light quarks, giving $2+1$ dynamical flavours. The production of this new generation of ensembles will enable the calculation of excited state physics. The systematic uncertainties in MEM will be reduced, giving us the opportunity to fine-tune our results for S-wave charmonium and D mesons. The P-wave states may also become accessible.

Bibliography

[1] P.W. Higgs. Broken symmetries and the masses of gauge bosons. *Physical Review Letters*, 13(508), 1964.

[2] F. Englert and R. Brout. Broken symmetry and the mass of gauge vector mesons. *Physical Review Letters*, 13(321), 1964.

[3] Y. Nambu and G. Jona-Lasinio. Dynamic model of elementary particles based on an analogy with superconductivity. *Physical Review*, 122(345), 1961.

[4] S. Borsányi et al. Is there still any T_c mystery in lattice QCD? results with physical masses in the continuum limit III. *Journal of High Energy Physics*, 73, 2010. [arXiv:hep-lat/1005.3508].

[5] Y. Aoki, G. Endrodi, Z. Fodor, S.D. Katz, and K.K. Szabo. The order of the quantum chromodynamics transition predicted by the standard model of particle physics. *Nature*, 443:675–678, 2006. [arXiv:hep-lat/0611014].

[6] T. Bhattacharya et al. The QCD phase transition with physical mass, chiral quarks. *Physical Review Letters*, 113(082001), 2014. [arXiv:hep-lat/1402.5175].

[7] J. Adams et al [STAR collaboration]. Experimental and theoretical challenges in the search for the quark gluon plasma: The STAR collaboration's critical assessment of the evidence from RHIC collisions. *Nuclear Physics A*, 757:102–183, 2005. [arXiv:nucl-ex/0501009].

[8] J.-Y. Ollitrault. Anisotropy as a signature of transverse collective flow. *Physical Review D*, 46(229), 1992.

[9] U.W. Heinz. *Relativistic Heavy Ion Physics - Early Collective Expansion: Relativistic Hydrodynamics and the Transport Properties of QCD Matter*, volume 23. Landolt–Börnstein, 2010. [arXiv:nucl-th/0901.4355].

[10] K. Adcox et al [PHENIX Collaboration]. Formation of dense partonic matter in relativistic nucleus-nucleus collisions at RHIC: Experimental

evaluation by the PHENIX collaboration. *Nuclear Physics A*, 757:184–283, 2005. [arXiv:nucl-ex/0410003].

[11] C. Silvestre for the PHENIX Collaboration. PHENIX first measurement of the J/ψ elliptic flow parameter v_2 in Au-Au collisions at $\sqrt{s_{NN}} = 200$ GeV. *Journal of Physics G: Nuclear and Particle Physics*, 35, 2008. [arXiv:nucl-ex/0806.0475].

[12] K. Aamodt et al [ALICE Collaboration]. Elliptic flow of charged particles in Pb-Pb collisions at 2.76 TeV. *Physical Review Letters*, 105(252302), 2010. [arXiv:nucl-ex/1011.3914].

[13] E. Abbas et al [ALICE Collaboration]. J/ψ elliptic flow in Pb-Pb collisions at $\sqrt{s_{NN}} = 2.76$ TeV. *Physical Review Letters*, 111(162301), 2013. [arXiv:nucl-ex/1303.5880].

[14] P. Kovtun, D.T. Son, and A.O. Starinets. Viscosity in strongly interacting quantum field theories from black hole physics. *Physical Review Letters*, 94(111601), 2005. [arXiv:hep-th/0405231].

[15] M. Gyulassy and L. McLerran. New forms of QCD matter discovered at RHIC. *Nuclear Physics A*, 750:30–63, 2005. [arXiv:nucl-th/0405013].

[16] K. Adcox et al [PHENIX Collaboration]. Suppresion of hadrons with large transverse momentum in central Au+Au collisions at $\sqrt{s_{NN}} = 130$ GeV. *Physical Review Letters*, 88(022301), 2002. [arXiv:nucl-ex/0109003].

[17] S.S. Adler et al [PHENIX Collaboration]. Suppressed π^0 production at large transverse momentum in central Au+Au collisions at $\sqrt{s_{NN}} = 200$ GeV. *Physical Review Letters*, 91(072301), 2003. [arXiv:nucl-ex/0304022].

[18] D. d'Enterria. *Relativistic Heavy Ion Collisions: Jet Quenching*, volume 23. Springer, 2010. [arXiv:nucl-ex/0902.2011].

[19] G. David. Pion and photon production in heavy ion collisions. In *Proceedings of Science*, volume 15, 2008. [arXiv:nucl-ex/0903.0336].

[20] S. Wicks, W. Horowitz, M. Djordjevic, and M. Gyulassy. Heavy quark jet quenching with collisional plus radial energy loss and path length fluctuations. *Nuclear Physics A*, 783:493–496, 2007. [arXiv:nucl-th/0701063].

[21] A. Adare et al [PHENIX Collaboration]. Neutral pion production with respect to centrality and reaction plane in Au-Au collisions at $\sqrt{s_{NN}} = 200$ GeV. *Physical Review C*, 87(034911), 2013. [arXiv:nucl-ex/1208.2254].

[22] L. Adamczyk et al [STAR Collaboration]. Jet-hadron correlations in $\sqrt{s_{NN}} = 200$ GeV p+p and central Au+Au collisions. *Physical Review Letters*, 112(122301), 2014. [arXiv:nucl-ex/1302.6184].

[23] B. Abelev et al [ALICE Collaboration]. Centrality dependence of charged particle production at large transverse momentum in Pb-Pb collisions at $\sqrt{s_{NN}} = 2.76$ TeV. *Physics Letters B*, 720:52–62, 2013. [arXiv:nucl-ex/1208.2711].

[24] S. Chatrchyan et al [CMS Collaboration]. Study of high-p_T charged particle suppression in Pb-Pb compared to p-p collisions at $\sqrt{s_{NN}} = 2.76$ TeV. *European Physics Journal C*, 72(1945), 2012. [arXiv:nucl-ex/1202.2554].

[25] A. Adil and I. Vitev. Collisional dissociation of heavy mesons in dense QCD matter. *Physics Letters B*, 649:139–146, 2007. [arXiv:hep-ph/0611109].

[26] R. Sharma, I. Vitev, and B.-W. Zhang. A light-cone wavefunction approach to open heavy flavour dynamics in QCD matter. *Physical Review C*, 80(054902), 2009. [arXiv:hep-ph/0904.0032].

[27] S.S. Adler et al [PHENIX Collaboration]. Centrality dependence of charm production from single electrons measurement in Au+Au collisions at $\sqrt{s_{NN}} = 200$ GeV. *Physical Review Letters*, 94(082301), 2005. [arXiv:nucl-ex/0409028].

[28] G.D. Moore and D. Teaney. How much do heavy quarks thermalise in a heavy ion collision? *Physical Review C*, 71(064904), 2005. [arXiv:hep-ph/0412346].

[29] R. Rapp and H. Van Hees. *Quark-Gluon Plasma 4: Heavy Quarks in the Quark-Gluon Plasma*, volume 4. World Scientific, 2010. [arXiv:hep-ph/0903.1096].

[30] E. Eichten, K. Gottfried, T. Kinoshita, K.D. Lane, and T.-M. Yan. Charmonium: The model. *Physical Review D*, 17(3090), 1978.

[31] H. Miyazawa. Reconnection of strings and quark matter. *Physical Review D*, 20(2953), 1979.

[32] T. Matsui and H. Satz. J/ψ suppression by quark gluon plasma formation. *Physics Letters B*, 178:416–422, 1986.

[33] NA50 Collaboration. A new measurement of J/ψ suppression in Pb-Pb collisions at 158 GeV per nucleon. *European Physics Journal C*, 39:335–345, 2005. [arXiv:hep-ex/0412036].

[34] R. Arnaldi et al [NA60 Collaboration]. J/ψ production in p-A and A-A collisions at fixed target experiments. *Nuclear Physics A*, 830:345c–352c, 2009. [arXiv:nucl-ex/0907.5004].

[35] A. Adare et al [PHENIX Collaboration]. Cold nuclear matter effects on J/ψ as constrained by deuteron-gold measurements at $\sqrt{s_{NN}} = 200$ GeV. *Physical Review C*, 77(024912), 2008. [arXiv:nucl-ex/0711.3917].

[36] A. Adare et al [PHENIX Collaboration]. J/ψ production vs transverse momentum and rapidity in p+p collisions at $\sqrt{s_{NN}} = 200$ GeV. *Physical Review Letters*, 98(232002), 2007. [arXiv:hep-ex/0611020].

[37] A. Adare et al [PHENIX Collaboration]. J/ψ suppression at forward rapidity in Au+Au collisions at $\sqrt{s_{NN}} = 200$ GeV. *Physical Review C*, 84(054912), 2011. [arXiv:nucl-ex/1103.6269].

[38] S. Chatrchyan et al [CMS Collaboration]. Observation of sequential Upsilon suppression in Pb-Pb collisions. *Physical Review Letters*, 109(222301), 2012. [arXiv:nucl-ex/1208.2826].

[39] B. Abelev et al [ALICE Collaboration]. J/ψ suppression at forward rapidity in Pb-Pb collisions at $\sqrt{s_{NN}} = 2.76$ TeV. *Physical Review Letters*, 109(072301), 2012. [arXiv:hep-ex/1202.1383].

[40] B. Abelev et al [ALICE Collaboration]. Measurement of charm production at central rapidity in proton-proton collisions at $\sqrt{s_{NN}} = 2.76$ TeV. *Journal of High Energy Physics*, 191, 2012. [arXiv:hep-ex/1204:4007].

[41] R.L. Thews, M. Schroedter, and J. Rafelski. Enhanced J/ψ production in deconfined quark matter. *Physical Review C*, 63(054905), 2001. [arXiv:hep-ph/0007323].

[42] J. Stachel, A. Andronic, P. Braun-Munzinger, and K. Redlich. Confronting LHC data with the statistical hadronisation model. *Journal of Physics: Conference Series*, 509, 2014. [arXiv:nucl-th/1311.4662].

[43] X. Zhao and R. Rapp. Transverse momentum spectra of J/ψ in heavy-ion collisions. *Physics Letters B*, 664:253–257, 2008. [arXiv:hep-ph/0712.2407].

[44] Y. Liu, Z. Qu, X. Nu, and P. Zhuang. J/ψ transverse momentum distribution in high energy nuclear collisions. *Physics Letters B*, 678:72–76, 2009. [arXiv:nucl-th/0901.2757].

[45] M.I. Gorenstein, A.P. Kostyuk, H. Stoecker, and W. Greiner. Statistical coalescence model with exact charm conservation. *Physics Letters B*, 509:277–282, 2001. [arXiv:hep-ph/0010148].

[46] A. Andronic, P. Braun-Munzinger, K. Redlich, and J. Stachel. Evidence for charmonium generation at the phase boundary in ultra-relativistic nuclear collisions. *Physics Letters B*, 652:259–261, 2007. [arXiv:nucl-th/0701079].

[47] J. Adam et al [ALICE Collaboration]. Differential studies of inclusive J/ψ and $\psi(2S)$ production at forward rapidity in Pb-Pb collisions at $\sqrt{s_{NN}} =$ 2.76 TeV. *Journal of High Energy Physics*, 179, 2016. [arXiv:nucl-ex/1506.08804].

[48] B. Abelev et al [ALICE Collaboration]. Centrality, rapidity and transverse momentum dependence of J/ψ suppression in Pb-Pb collisions at $\sqrt{s_{NN}} = 2.76$ TeV. *Physics Letters B*, 734:314–327, 2014. [arXiv:nucl-ex/1311.0214].

[49] J. Adam et al [ALICE Collaboration]. Measurement of an excess in the yield of J/ψ at very low p_T in Pb-Pb collisions at $\sqrt{s_{NN}} = 2.76$ TeV. *Physical Review Letters*, 116(222301), 2016. [arXiv:nucl-ex/1509.08802].

[50] J. Adam et al [ALICE Collaboration]. J/ψ suppression at forward rapidity in Pb-Pb collisions at $\sqrt{s_{NN}} = 5.02$ TeV. *Physics Letter B*, 766:212–224, 2017. [arXiv:nucl-ex/1606.08197].

[51] K.G. Wilson. Confinement of quarks. *Physical Review D*, 10(2445), 1974.

[52] H.B. Nielsen and M. Ninomiya. Absence of neutrinos on a lattice: (1) proof by homotopy theory. *Nuclear Physics B*, 185:20–40, 1981.

[53] J. Kogut and L. Susskind. Hamiltonian formulation of Wilson's lattice gauge theories. *Physical Review D*, 11(395), 1975.

[54] K.G. Wilson. *New Phenomena in Subnuclear Physics, Part A [edited by A. Zichichi]*, volume 13. Plenum Press, 1977.

[55] P.H. Ginsparg and K.G. Wilson. A remnant of chiral symmetry on the lattice. *Physical Review D*, 25(2649), 1982.

[56] B. Sheikholeslami and R. Wohlert. Improved continuum limit lattice action for QCD with Wilson fermions. *Nuclear Physics B*, 259(572), 1985.

[57] M. Alford, T.R. Klassen, and G.P. Lepage. Improving lattice quark actions. *Nuclear Physics B*, 496:377–407, 1997. [arXiv:hep-lat/9611010].

[58] G. Aarts, C. Allton, S. Kim, M.-P. Lombardo, S.M. Ryan, and J.-I. Skullerud. Melting of P wave bottomonium states in the quark-gluon plasma from lattice NRQCD. *Journal of High Energy Physics*, 64, 2013. [arXiv:hep-lat/1310.5467].

[59] C. Morningstar and M. Peardon. The glueball spectrum from an anisotropic lattice study. *Physical Review D*, 60(034509), 1999. [arXiv:hep-lat/9901004].

[60] C. Morningstar and M. Peardon. The glueball spectrum from novel improved actions. *Nuclear Physics Proceedings Supplement*, 83:887–889, 2000. [arXiv:hep-lat/9911003].

[61] J. Foley, A. Ó'Cais, M. Peardon, and S.M. Ryan. A non-perturbative study of the action parameters for anisotropic lattice quarks. *Physical Review D*, 73(014514), 2006. [arXiv:hep-lat/0405030].

[62] C. Morningstar and M. Peardon. Analytic smearing of SU(3) link variables in lattice QCD. *Physical Review D*, 69(054501), 2004. [arXiv:hep-lat/0311018].

[63] P. Chen. Heavy quarks on anisotropic lattices: The charmonium spectrum. *Physical Review D*, 64(034509), 2001. [arXiv:hep-lat/0006019].

[64] H.-W. Lin, S.D. Cohen, J. Dudek, R.G. Edwards, B. Joó, and D. G. Richards. First results from 2 + 1 dynamical quark flavours on an anisotropic lattice: Light-hadron spectroscopy and setting the strange-quark mass. *Physical Review D*, 79(034502), 2008. [arXiv:hep-lat/0810.3588].

[65] M. Asakawa, Y. Nakahara, and T. Hatsuda. Maximum entropy analysis of the spectral functions in lattice QCD. *Progress in Particle and Nuclear Physics*, 46:459–508, 2001. [arXiv:hep-lat/0011040].

[66] T. A. DeGrand and C.E. DeTar. Static screening lengths in the gluon plasma. *Physical Review D*, 34(2469), 1986.

[67] M. Laine and M Vepsäläinen. Meson correlation lengths in high temperature QCD. *Journal of High Energy Physics*, 004, 2004. [arXiv:hep-ph/0311268].

[68] A. Bazavov, F. Karsch, Y. Maezawa, S. Mukherjee, and P. Petreczky. In-medium modifications of open and hidden strange-charm mesons

from spatial correlation functions. *Physical Review D*, 91(054503), 2005. [arXiv:hep-lat/1411.3018].

[69] B.B. Brandt, A. Francis, M. Laine, and H.B. Meyer. A relation between screening masses and real time rates. *Journal of High Energy Physics*, 117, 2014. [arXiv:hep-ph/1404.2404].

[70] C. DeTar and J.B. Kogut. Measuring the hadronic spectrum of the quark plasma. *Physical Review D*, 36(2828), 1987.

[71] T. Hatsuda and T. Kunihiro. QCD phenomenology based on a chiral effective lagrangian. *Physics Reports*, 247:221–367, 1994. [arXiv:hep-ph/9401310].

[72] G.Q. Li, C.M. Ko, and G.E. Brown. Enhancement of low-mass dileptons in heavy ion collisions. *Physics Review Letters*, 75:4007–4010, 1995. [arXiv:nucl-th/9504025].

[73] R. Rapp and J. Wambach. Chiral symmetry restoration and dileptons in relativistic heavy-ion collisions. *Advances in Nuclear Physics*, 25(1), 2000. [arXiv:hep-ph/9909229].

[74] G. Boyd, S. Gupta, F. Karsch, and E. Laermann. Spatial and temporal hadron correlators below and above the chiral phase transition. *Zeitschrift für Physik C*, 64:331–338, 1994. [arXiv:hep-lat/9405006].

[75] Ph. deForcrand et al [QCD-TARO Collaboration]. Mesons correlators in finite temperature lattice QCD. *Physical Review D*, 63(054501), 2001. [arXiv:hep-lat/0008005].

[76] E. Laermann and P. Schmidt. Mesons screening masses at high temperature in quenched QCD with improved Wilson quarks. *European Physical Journal C*, 20:541–552, 2001. [arXiv:hep-lat/0103037].

[77] T. Bayes and R. Price. An essay towards solving a problem in the doctrine of chances. By the late Rev. Mr. Bayes, F.R.S. communicated by Mr. Price, in a letter to John Canton, A.M.F.R.S. *Philosophical Transactions of the Royal Society of London*, 53:370–418, 1763.

[78] R. Bryan. Maximum entropy analysis of oversampled data problems. *European Biophysics Journal*, 18:165–174, 1990.

[79] G. Aarts, C. Allton, J. Foley, S. Hands, and S. Kim. Spectral functions at non-zero momentum in hot QCD. In *Proceedings of Science*, volume 134, 2006. [arXiv:hep-lat/0610061].

[80] G. Aarts, C. Allton, J. Foley, S. Hands, and S. Kim. Spectral functions at small energies and the electrical conductivity in hot, quenched lattice QCD. *Physical Review Letters*, 99(022002), 2007. [arXiv:hep-lat/0703008].

[81] A. Rothkopf. Improved maximum entropy analysis with an extended search space. *Journal of Computational Physics*, 238:106–114, 2013. [arXiv:hep-lat/1110.6285].

[82] A. Rothkopf. Improved maximum entropy method with an extended search space. In *Proceedings of Science*, 2012. [arXiv:physics.comp-ph/1208:5162].

[83] Y. Burnier and A. Rothkopf. A novel Bayesian approach to spectral function reconstruction. *Physical Review Letters*, 111(182003), 2013. [arXiv:hep-lat/1307.6106].

[84] S. Kim, P. Petreczky, and A. Rothkopf. Lattice NRQCD study on in-medium bottomonium spectra using a novel Bayesian reconstruction approach. *American Institute of Physics Conference Proceedings*, 1701, 2016. [arXiv:hep-lat/1411.3137].

[85] Y. Burnier, O. Kaczmarek, and A. Rothkopf. Static quark-antiqiark potential in the quark-gluon plasma from lattice QCD. *Physical Review Letters*, 114(082001), 2015. [arXiv:hep-lat/1410.2546].

[86] Y. Burnier, O. Kaczmarek, and A. Rothkopf. The Bayesian reconstruction of the in-medium heavy quark potential from lattice QCD and its stability. [arXiv:hep-lat/1411.3141], 2014.

[87] B.B. Brandt, A. Francis, H.B. Meyer, and H. Wittig. Thermal correlators in the ρ channel of two-flavour QCD. *Journal of High Energy Physics*, 100, 2013. [arXiv:hep-lat/1212.4200].

[88] O. Kaczmarek and M. Müller. Temperature dependence of electrical conductivity and dilepton rates from hot quenched lattice QCD. In *Proceedings of Science*, 2013. [arXiv:hep-lat/1312.5609].

[89] A. Francis, O. Kaczmarek, M. Laine, T. Neuhaus, and H. Ohno. A non-perturbative estimate of the heavy quark momentum diffusion coefficient. *Physical Review D*, 92(116003), 2015. [arXiv:hep-lat/1508.04543].

[90] B.B. Brandt, A. Francis, H.B. Meyer, and D. Robaina. The pion quasi-particle in the low-temperature phase of QCD. *Physical Review D*, 92(094510), 2015. [arXiv:hep-lat/1506.05732].

[91] D. Dudal, O. Oliveira, and P.J. Silva. Källén-Lehmann spectroscopy for (un)physical degrees of freedom. *Physical Review D*, 89(014010), 2014. [arXiv:hep-lat/1310.4069].

[92] P.J. Silva, O. Oliveira, D. Dudal, P. Bicudo, and N. Cardoso. Aspects of gluon propagation in landau gauge: Spectral densities and mass scales at finite temperature. *Acta Physica Polonica B Proceedings Supplement*, 8, 2015. [arXiv:hep-lat/1412:4286].

[93] G. Cuniberti, E. De Micheli, and G.A. Viano. Reconstructing the thermal green functions at real times from those at imaginary times. *Communications in Mathematical Physics*, 216:59–83, 2001. [arXiv:cond-mat/0109175].

[94] Y. Burnier, M. Laine, and L. Mether. A test on analytic continuation of thermal imaginary-time data. *European Physical Journal C*, 71(1619), 2011. [arXiv:hep-lat/1101.5534].

[95] J. Ghiglieri, O. Kaczmarek, M. Laine, and F. Meyer. Lattice constraints on the thermal photon rate. *Physical Review D*, 94(016005), 2016. [arXiv:hep-lat/1604.07544].

[96] S. Digal, P. Petreczky, and H. Satz. Quarkonium feed-down and sequential suppression. *Physical Review D*, 64(094015), 2001. [arXiv:hep-ph/0106017].

[97] P. Zhuang and X. Zhu. Leakage effect on $J/\psi p_T$ distributions in different centrality bins for Pb-Pb collisions at E/A=160 GeV. *Physical Review C*, 67(067901), 2003. [arXiv:nucl-th/0304019].

[98] X. Zhao and R. Rapp. Charmonium production at high p_T at RHIC. In *24th Winter workshop on Nuclear Dynamics (WWND 2008)*, volume 24, 2008. [arXiv:nucl-th/0806.1239].

[99] M.B. Oktay and J.-I. Skullerud. Momentum dependence of charmonium spectral functions from lattice QCD. [arXiv:hep-lat/1005.1209], 2010.

[100] D. Forster. *Hydrodynamic Fluctuations, Broken Symmetry, and Correlation Functions*, volume 47. Perseus Books, 1995.

[101] H.B. Meyer. Transport properties of the quark-gluon plasma — a lattice QCD perspective. *European Physical Journal A*, 47(86), 2011. [arXiv:hep-lat/1104.3708].

[102] S. Gupta. The electrical conductivity and soft photon emissivity of the QCD plasma. *Physics Letters B*, 597:57–62, 2004. [arXiv:hep-lat/0301006].

[103] H.-T. Ding, A. Francis, O. Kaczmarek, F. Karsch, E. Laermann, and W. Soeldner. Thermal dilepton rate and electrical conductivity: An analysis of vector current correlation functions in quenched lattice QCD. *Physical Review D*, 83(034504), 2011. [arXiv:1012.4963].

[104] A. Amato, G. Aarts, C. Allton, P. Giudice, S. Hands, and J.-I. Skullerud. Electrical conductivity of the quark-gluon plasma across the deconfinement transition. *Physical Review Letters*, 111(172001), 2013. [arXiv:hep-lat/1307.6763].

[105] G. Aarts, C. Allton, A. Amato, P. Giudice, S. Hands, and J.-I. Skullerud. Electrical conductivity and charge diffusion in thermal QCD from the lattice. *Journal of High Energy Physics*, 186, 2015. [arXiv:hep-lat/1412.6411].

[106] H.-T. Ding, A. Francis, O. Kaczmarek, F. Karsch, H. Satz, and W. Soeldner. Charmonium properties in hot quenched lattice QCD. *Physical Review D*, 86(014509), 2012. [arXiv:hep-lat/1204.4945].

[107] P. Petreczky and D. Teaney. Heavy quark diffusion from the lattice. *Physical Review D*, 73(014508), 2006. [arXiv:hep-ph/0507318].

[108] H.B. Meyer. The errant life of a heavy quark in the quark-gluon plasma. *New Journal of Physics*, 13, 2011. [arXiv:hep-lat/1012.0234].

[109] A. Francis, O. Kaczmarek, M. Laine, and J. Langelage. Towards a non-perturbative measurement of the heavy quark momentum diffusion coefficient. In *Proceedings of Science*, 2011. [arXiv:hep-lat:1109.3941].

[110] S. Caron-Huot, M. Laine, and G.D. Moore. A way to estimate the heavy quark thermalisation rate from the lattice. *Journal of High Energy Physics*, 53, 2009. [arXiv:hep-lat/0901.1195].

[111] J. Casalderrey-Solana and D. Teaney. Heavy quark diffusion in strongly coupled $\mathcal{N} = 4$ Yang Mills. *Physical Review D*, 74(085012), 2006. [arXiv:hep-ph/0605199].

[112] G. Aarts, C. Allton, M.B. Oktay, M. Peardon, and J.-I. Skullerud. Charmonium at high temperature in two flavour QCD. *Physical Review D*, 76(094513), 2007. [arXiv:hep-lat/0705.2198].

[113] R. Lewis and R.M. Woloshyn. Light vector meson decay constants and the renormalisation factor from a tadpole-improved action. *Physical Review D*, 56:1571–1578, 1997. [arXiv:hep-lat/9610027].

[114] H. Ohno, S. Aoki, S. Ejiri, K. Kanaya, Y. Maezawa, H. Saito, and T. Umeda. Charmonium spectral functions with the variational method in zero and finite temperature lattice QCD. *Physical Review D*, 84(094504), 2011. [arXiv:hep-lat/1104.3384].

[115] M. Asakawa and T. Hatsuda. J/ψ and η_c in the deconfined plasma from lattice QCD. *Physical Review Letters*, 92(012001), 2004. [arXiv:hep-lat/0308034].

[116] I. Vitev. Testing the theory of QGP-induced energy loss at RHIC and the LHC. *Physics Letters B*, 639:38–45, 2006. [arXiv:hep-ph/0603010].

[117] B. Abelev et al [STAR Collaboration]. Transverse momentum and centrality dependence of high p_T non-photonic electron suppression in Au+Au collisions at $\sqrt{s_{NN}} = 200$ GeV. *Physical Review Letters*, 98(192301), 2007. [arXiv:nucl-ex/0607012].

[118] N. Armesto, M. Cacciari, A. Dainese, C.A. Salgado, and U.A. Wiedemann. How sensitive are high-p_T electron spectra at RHIC to heavy quark energy loss? *Physics Letters B*, 637:362–366, 2006. [arXiv:hep-ph/0511257].

[119] M. He, R.J. Fries, and R. Rapp. D_s-meson as quantative probe of diffusion and hadronisation in nuclear collisions. *Physical Review Letters*, 110(112301), 2013. [arXiv:nucl-th/1204.4442].

[120] Y. Zhang for STAR Collaboration. Open charm hadron measurement in p+p and Au+Au collisions at $\sqrt{s_{NN}} = 200$ GeV in STAR. *Journal of Physics G: Nuclear and Particle Physics*, 38, 2011. [arXiv:nucl-ex/1106.6078].

[121] B. Abelev et al [ALICE Collaboration]. Measurement of prompt D-meson production in p-Pb collisions at $\sqrt{s_{NN}} = 5.02$ TeV. *Physical Review Letters*, 113(232301), 2014. [arXiv:nucl-ex/1405.3452].

[122] S. De for the ALICE Collaboration. Measurements of open heavy-flavour production with ALICE at the LHC. *Journal of Physics: Conference Series*, 770, 2016. [arXiv:nucl-ex/1609.02862].

[123] T. Hilger, R. Thomas, and B. Kampfer. QCD sum rules for D and B mesons in nuclear matter. *Physical Review C*, 79(025202), 2009. [arXiv:nucl-th/0809.4996].

[124] Z.-G. Wang. Analysis of the heavy mesons in the nuclear matter with the QCD sum rules. *Physical Review C*, 92(065205), 2015. [arXiv:hep-ph/1501.05093].

[125] K. Suzuki, P. Gubler, and M. Oka. D meson mass increase by restoration of chiral symmetry in nuclear matter. *Physical Review C*, 93(045209), 2016. [arXiv:hep-ph/1511.04513].

[126] C. Fuchs, B.V. Martemyanov, A. Faessler, and M.I. Krivoruchenko. D-mesons and charmonium states in hot pion matter. *Physical Review C*, 73(035204), 2006. [arXiv:nucl-th/0410065].

[127] A. Bazavov et al. The melting and abundance of open charm hadrons. *Physics Letters B*, 737:210–215, 2014. [arXiv:hep-lat/1404.4043].

[128] S. Mukherjee, P. Petreczky, and S. Sharma. Charm degrees of freedom in the quark gluon plasma. *Physical Review D*, 93(014502), 2016. [arXiv:hep-lat/1509.08887].

[129] A. Kelly and J.-I. Skullerud. Thermal D mesons from anistotropic lattice QCD. In *Proceedings of Science*, 2016. [arXiv:hep-lat/1701.09005].

[130] L. Liu et al. Excited and exotic charmonium spectroscopy from lattice QCD. *Journal of High Energy Physics*, 126, 2012. [arXiv:hep-ph/1204.5425].

[131] S. Borsányi et al. QCD thermodynamics with dynamical overlap fermions. *Physics Letters B*, 713:342–346, 2012. [arXiv:hep-lat/1204.4089].

[132] S. Cotter, P. Giudice, S. Hands, and J.-I. Skullerud. Towards the phase diagram of dense two-colour matter. *Physical Review D*, 87(034507), 2013. [arXiv:hep-lat/1210.4496].

[133] G. Moir, M. Peardon, S.M. Ryan, C.E. Thomas, and L. Liu. Excited spectroscopy of charmed mesons from lattice QCD. *Journal of High Energy Physics*, 21, 2013. [arXiv: hep-ph/1301.7670].

[134] S. Datta, F. Karsch, P. Petreczky, and I. Wetzorke. Behaviour of charmonium systems after deconfinement. *Physical Review D*, 69(094507), 2004. [arXiv:hep-lat/0312037].

[135] J. Adam et al [ALICE Collaboration]. Measurement of D_s^+ production and nuclear modification factor in Pb-Pb collisions at $\sqrt{s_{NN}} = 2.76$ TeV. *Journal of High Energy Physics*, 082, 2016. [arXiv:nucl-ex/1509.07287].

[136] J.-I. Skullerud et al. Quark-gluon plasma phenomenology from anisotropic lattice QCD. *American Institute of Physics Conference Proceedings*, 1701(060018), 2016. [arXiv:hep-lat/1501.00018].

[137] T. Umeda. Quarkonium at finite temperature. *Nuclear Physics A*, 783:277–284, 2007. [arXiv:hep-lat/0610030].

[138] R.G. Edwards, B. Joó, and H.-W. Lin. Tuning for three flavors of anisotropic clover fermions with stout-link smearing. *Physical Review D*, 78(054501), 2008. [arXiv:hep-lat/0803.3960].

[139] I. Horvath, A.D. Kennedy, and S. Sint. A new exact method for dynamical fermion computations with non-local actions. *Nuclear Physics Proceedings Supplement*, 73:834–836, 1999. [arXiv:hep-lat/9809092].

[140] R.G. Edwards and B. Joó. The Chroma software system for lattice QCD. *Nuclear Physics Proceedings Supplement*, 140(832), 2005. [arXiv:hep-lat/0409003].

[141] M. Alford, T. Klassen, and P. Lepage. A quark action for very coarse lattices. *Physical Review D*, 58(034503), 1998. [arXiv:hep-lat/9712005].

[142] S. Borsányi et al. Anisotropy tuning with the Wilson flow. [arXiv:hep-lat/1205.0781], 2012.

[143] M. Lüscher and P. Weisz. Perturbative analysis of the gradient flow in non-abelian gauge theories. *Journal of High Energy Physics*, 51, 2011. [arXiv:hep-lat/1101.0963].

[144] M. Lüscher. Trivialising maps, the Wilson flow and the HMC algorithm. *Communications in Mathematical Physics*, 293:899–919, 2010. [arXiv:hep-lat/0907.5491].

[145] M. Lüscher. Properties and uses of the Wilson flow in lattice QCD. *Journal of High Energy Physics*, 71, 2010. [arXiv:hep-lat/1006.4518].

[146] S. Borsányi et al. High precision scale setting in lattice QCD. *Journal of High Energy Physics*, 010, 2012. [arXiv:hep-lat/1203.4469].

[147] S. Kim. Heavy flavours in quark-gluon plasma. In *Proceedings of Science*, 2016. [arXiv:hep-lat/1702.02297].